

Design Optimization of a Boundary Layer Ingestion Propulsor Using a Coupled Aeropropulsive Model

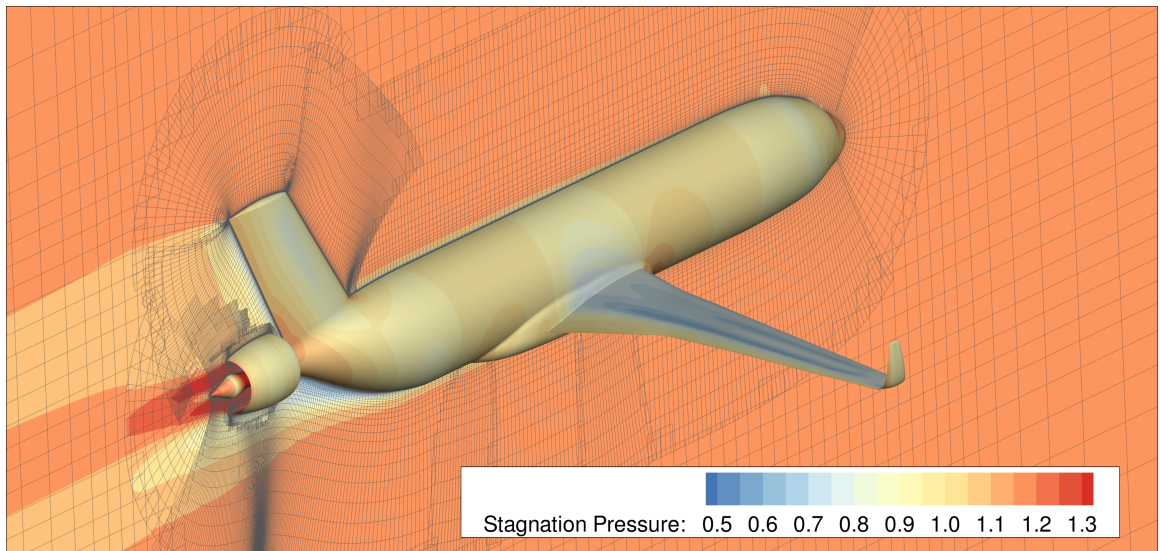
by

Justin S. Gray

A dissertation submitted in partial fulfillment
of the requirements for the degree of
Doctor of Philosophy
(Aerospace Engineering)
in the University of Michigan
2018

Doctoral Committee:

Professor Joaquim R. R. A. Martins, Chair
Professor James F. Driscoll
Dr. James Heidmann
Professor Eric Johnsen



Justin S. Gray

Justin.S.Gray@nasa.gov

ORCID id: 0000-0002-7506-7360

©Justin S. Gray 2018

For anyone who was ever told that something could not be done, and then went and did it anyway. It will only be impossible until you figure out how to do it!

ACKNOWLEDGMENTS

This thesis would not have been possible without the support of many people who I am lucky to be able to call mentors and friends. First I would like to thank my family for their loving support throughout my whole life, but in particular during the years I've worked on this research. Sharon and Eli, I asked an awful lot of you both while I took this journey. Thank you for allowing me to spend a year away from home to take classes and for supporting me at every step of the way. Thank you, also, to my parents who taught me a love of learning and made sure I had the opportunity to do it.

Before I ever started this research there were many people who helped to make it possible. I never would have been involved in MDO research at all, if it had not been for Professor Juan Alonso who ensured that the OpenMDAO project got off the ground at NASA Glenn in 2007, and who continued to support the effort ever since. Thank you to Cindy Naiman and Bob Plencner, who decided to take a chance on a very young, very inexperienced engineer and see if I could find a way to make OpenMDAO into something useful. It was through the work on the OpenMDAO project that I first discovered the MDO research field and started trying to figure out how to use all of the amazing ideas it was producing. Looking back on that time now, I see how vitally important my early interactions with so many researchers were in shaping my own work. In particular, I would like to thank Dr. Evin Cramer, Professor William Crossley, Professor Joaquim Martins, and Professor Karen Wilcox for their willingness to share some of their valuable expertise with me.

When I decided to attempt to earn a doctorate, Therese Griebel and Dr. James Heidmann went far out of their way to make sure that I had the opportunity to undertake this research. Thank you both for your faith in me. This work would have been possible without your support, and I sincerely hope that you both find the result worth the investment.

Thank you to Dr. Gaetan Kenway, Dr. Charles Mader, and Dr. John Hwang for freely sharing your knowledge and experience with me and more importantly for being patient with me while I tried to absorb it.

Thank you to the OpenMDAO development team: Bret Naylor, Dr. Ken Moore, Dr. Steve Ryan, Herb Schilling, and Keith Marsteller. Your unending work to improve and extend OpenMDAO was so fundamentally important to the success of this research that I simply could not have completed it without your help. I look forward to many more years of productive research with you all.

I owe a special thank you two colleagues in particular, Dr. Eric Hendricks and Rob Falck. You both picked up much of the slack that I had to lay out in order to find the time to do this. I left many things to you that would normally have fallen to me and you handled them without complaint. I am lucky to be able to work with you both.

And last but certainly not least I need to acknowledge my advisor, Professor Joaquim Martins. In addition to sharing much advice early in my research career, you graciously agreed to supervise my doctorate. I can not thank you enough for your advice, mentorship, and friendship. You let me choose my own path and found a way to help guide me along it. I could not have asked for a better advisor and I will always consider myself your student.

TABLE OF CONTENTS

Dedication	ii
Acknowledgments	iii
List of Figures	viii
List of Tables	xii
List of Appendices	xiii
List of Abbreviations	xiv
Abstract	xv
 Chapter	
1 Introduction	1
1.1 Background	1
1.2 How BLI works	7
1.2.1 An aerodynamic perspective	8
1.2.2 A propulsive perspective	10
1.2.3 A note about total pressure loss	14
1.3 BLI research using uncoupled modeling methods	15
1.3.1 Conceptual aircraft design studies	16
1.3.2 Aerodynamics focused investigations	18
1.3.3 Propulsion focused investigations	19
1.4 Applying high-fidelity MDO to aeropropulsive design	20
2 Approach aeropropulsive design optimization of BLI systems	22
2.1 MDO architectures for aeropropulsive applications	24
2.2 Using the OpenMDAO to compute analytic derivatives for coupled models	26
2.2.1 A simple representative example	30
2.3 Overview of OpenMDAO model structure	33
3 pyCycle: propulsion analysis for multidisciplinary applications	35
3.1 Predicting gas thermodynamic properties via chemical equilibrium analysis	36
3.1.1 Chemical Equilibrium Equations	37
3.1.2 Analytic Derivatives	43
3.1.3 Verification of Analysis and Derivatives	44

3.1.4 Optimization Results	52
3.2 Building a modular propulsion analysis library with analytic derivatives .	55
3.3 Summary	58
4 Quantifying the importance of aeropropulsive coupling in BLI applications	59
4.1 Modeling	59
4.1.1 Propulsion model	60
4.1.2 BLI Aerodynamic Model	61
4.1.3 Podded configuration aerodynamic model	63
4.1.4 Aeropropulsive coupling	63
4.2 Results	65
4.2.1 Net force as a function of FPR	67
4.2.2 Propulsor force as a function of FPR	68
4.2.3 Fuselage force as a function of FPR	71
4.3 Summary	75
5 Design optimization of a axisymmetric BLI propulsion system	78
5.1 Design optimization of the aeropropulsive fuselage	79
5.1.1 Aerodynamic Model	79
5.1.2 Propulsion Model	81
5.1.3 Optimization Problem	82
5.1.4 Aeropropulsive Optimization Results	83
5.2 BLI Propulsor Sizing Analysis	85
5.2.1 Podded Propulsor Performance	85
5.2.2 Propulsion System Sizing Method	87
5.2.3 Propulsion Sizing Results	88
5.2.4 Qualitative Analysis of the Optimized Configurations	89
5.3 Summary	92
6 Distortion constrained optimization of a 3-D BLI propulsor	94
6.1 Aerodynamic Model	95
6.1.1 Aircraft Geometry	95
6.1.2 RANS Solver: ADflow	96
6.1.3 Grid Convergence Study	98
6.1.4 Force Accounting	98
6.1.5 Computing BLI Propulsor Power	101
6.2 Propulsion Model	101
6.2.1 1D Cycle Model: pyCycle	101
6.2.2 BLI Propulsor Model	103
6.3 Aeropropulsive Optimization	104
6.3.1 Optimization Problem	104
6.3.2 Optimization Results	108
6.4 Summary	115
7 Concluding Remarks	116
7.0.1 Summary and Future Work	116

7.0.2 Contributions	118
Bibliography	121
Appendices	131

LIST OF FIGURES

1.1	Artist conception of a notional BWB or HWB aircraft	4
1.2	Artist conception of a notional D8 aircraft concept with top, aft mounted BLI propulsion system.	5
1.3	Artist conception of a notional BWB aircraft with a turboelectric distributed propulsion system.	6
1.4	Artist conception of the STARC-ABL aircraft with a turboelectric BLI aft mounted propulsor.	6
1.5	Integration surface definitions for notional podded and BLI propulsor configurations. S_{body} is the propulsion control volume. S_{TP} is the Trefftz plane.	9
1.6	Propulsion centric control volumes for the podded (top) and BLI (bottom) configurations.	11
1.7	Normalized outflow velocity as a function of of normalized average inflow velocity for four different values of the normalized energy addition (\dot{Q}).	13
1.8	The STARC-ABL configuration, with the turboelectric power flow highlighted by the red arrow. Electric power is generated by generators on the underwing nacelles and send to the aft fuselage to power an electric BLI propulsor.	18
2.1	Scaling of the cost for computing derivatives vs the number of design variables for a representative design optimization of a satellite design problem.	23
2.2	extended design structure matrix (XDSM) [1] diagram displaying a notional aeropropulsive optimization problem solved with the MDF optimization architecture.	25
2.3	XDSM [1] diagram displaying a notional aeropropulsive optimization problem solved with the IDF optimization architecture.	26
2.4	XDSM [1] diagram showing how a simple example model would be constructed in OpenMDAO.	31
2.5	Diagram of a notional OpenMDAO model, including the four major classes.	33
3.1	XDSM diagram of the chemical equilibrium analysis sequence.	37
3.2	Structure of partial derivative matrix for adjoint multidisciplinary derivatives of T_p solver. The subset of partial derivatives needed for the Newton solver is highlighted by the gray box	44
3.3	Structure of partial derivative matrix for adjoint multidisciplinary derivatives of hP and S_p solvers. The subset of partial derivatives needed for the Newton solver are highlighted by the gray box.	45

3.4	Variation of total number of active chemical species in CEA solutions with respect to temperature.	47
3.5	Mean differences between equilibrium gas compositions predicted by CEA and by proposed code.	48
3.6	l^2 norm of difference between concentration vectors, $\ n_{\text{CEA}} - n\ _2$	49
3.7	Mean relative errors between the thermodynamic states predicted by CEA and by proposed code is less than 0.1%.	50
3.8	Relative error of finite-difference approximations versus step size obtained for standard day conditions and by using computed analytic values as reference.	51
3.9	Relative error of finite-difference approximations versus step size for cruise conditions and with computed analytic values as reference.	52
3.10	Wall times required to compute the 5×2 Jacobian by using analytic methods (direct and adjoint) and finite-difference approximations.	52
3.11	Air-fuel equivalence ratio ϕ that maximizes the combustion temperature T as a function of pressure P ranging from 15 to 1500 psi.	53
3.12	Optimization wall time versus tolerance of chemical-equilibrium solver obtained by using analytic and finite-difference methods to compute derivatives.	54
3.13	Diagram of how cycle elements are combined in a pyCycle model to construct a propulsion analysis for a specific engine cycle. Each box is a single element.	55
3.14	XDSM diagram for the pyCycle Duct element. Engineering calculations are shown as red boxes. Chemical equilibrium flow solves are shown in blue.	57
3.15	XDSM diagram for the pyCycle Compressor element. Engineering calculations are shown as red boxes. Chemical equilibrium flow solves are shown in blue.	57
4.1	Axisymmetric fuselage with aft mounted BLI propulsor representing a simplified STARC-ABL configuration.	60
4.2	XDSM [1] diagram of the propulsor model, including the Newton solver used find the required mass flow rate to satisfy the shaft power residual ($\mathcal{R}_{\text{pwr}} = \text{Pwr}_{\text{shaft}} - 3500 = 0$)	61
4.3	Free-form deformation defining the geometry parametrization. Green nodes are allowed to move while red nodes are fixed.	62
4.4	Podded propulsor configuration with clean fuselage (top) and detailed view of the propulsor (bottom).	63
4.5	XDSM [1] for the coupled aero-propulsive analysis.	64
4.6	Converged flow solutions for FPR = 1.2 (top), FPR = 1.35 (middle), and the clean fuselage (bottom) designs	67
4.7	Net force on the body (fuselage and propulsor) as a function of design FPR.	68
4.8	Force integrated over propulsor ($C_{F_{\text{prop}}}$) as a function of design FPR.	69
4.9	Mach contours for the propulsor simulation on the FPR = 1.2 (top) and FPR = 1.35 (bottom) designs of the podded configuration.	70

4.10	Mass-averaged total pressure normalized by the value for the podded configuration as a function of FPR for the podded configuration (pink), the BLI configuration with a fully coupled analysis (solid blue), and a decoupled analysis (dashed blue)	72
4.11	Force coefficient on the fuselage, $C_{F_{\text{fuse}}}$ as a function of design FPR.	72
4.12	Comparison of boundary layer profiles at the aft fuselage between the podded and BLI configurations; $l_{\text{ref}} = 4 \text{ ft}$	73
4.13	Comparison of surface C_p vs axial distance from the inlet (x/l_{ref}) between the podded and BLI configurations vs axial distance with FPRs of 1.35 and 1.2; $l_{\text{ref}} = 4 \text{ ft}$	74
5.1	BLI configuration and boundary conditions: viscous walls (S_1, S_2), outflow face (S_3), and inflow face (S_4)	79
5.2	The podded configuration serves as a reference and models fuselage (top) and propulsor (bottom) separately.	80
5.3	The shape of the BLI configuration is enveloped in FFD boxes (black lines) and parameterized using FFD control points.	80
5.4	The propulsor fan model consists of three sub-models; It computes the shaft power and fan exit conditions given the FPR, mass flow, and fan face conditions.	81
5.5	XDSM diagram of the full optimization problem formulation, including the compatibility constraints that enforce the aeropropulsive coupling.	83
5.6	Power saving coefficient vs C_{F_x} shows that smaller BLI propulsors (small positive C_{F_x}) offer greater power savings than larger ones.	85
5.7	$P_{\text{shaft}}/C_{F_{\text{pod}}}$ data (circles) and 4 th order polynomial fit (solid line) for the podded propulsor.	86
5.8	Overall aircraft PSC at cruise vs the fraction of shaft power used for BLI at different assumed values of transmission efficiency, η_{trans}	89
5.9	Best-performing designs for three assumed values of η_{trans} . Increased transmission efficiency drives the design to larger BLI propulsors relative to the under-wing engines.	90
5.10	Boundary layer profiles (measured via $p_t/p_{t\infty}$) for the best designs found for each assumed value of η_{trans} . The horizontal dashed lines indicate the height of the inlet lip for each design.	91
6.1	openVSP model of the STARC-ABL aircraft geometry including the vertical tail and aft mounted BLI propulsor.	96
6.2	Diagram of the shape parameterization for the aft fuselage and BLI propulsor. The red curves represent elliptical cross sections and the yellow curves represent circular cross sections. Each cross section on the BLI nacelle also has tangent strength and angle design variables which control the surface bezier curves.	97
6.3	Overset mesh of the model with surface C_p color contours.	97
6.4	Side view of the aft mounted BLI propulsor including the body-force zone that simulates the fan. The p_t color contours show the effect of the van via the increased pressure.	98

6.5	Grid convergence study on the convergence of the coefficient of net force (C_F) for the 3-D STARC-ABL aerodynamic model.	99
6.6	Grid convergence study on the convergence of the aggregated distortion metric ($\hat{\kappa}$) for the 3-D STARC-ABL aerodynamic model.	99
6.7	Cycle elements in the pyCycle model of the BLI propulsor. Red elements are explicit calculations, blue elements are implicit calculations.	104
6.8	Fan adiabatic efficiency versus FPR, assuming a constant polytropic efficiency of 97%.	105
6.9	XDSM diagram of the full optimization problem formulation.	107
6.10	ARP1420 distortion calculation diagram, showing the notional pressure rake locations (left) and a notional pressure trace taken across a single radial measurement stations (right).	108
6.11	Contours of stagnation pressure for the baseline and three optimized geometries.	110
6.12	Front view comparison between the optimized designs for the unconstrained (left) and distortion-constrained (right) BLI propulsor inlet for the different cases considered.	112
6.13	Actual numerical pressure rake used to compute distortion metric, with 150 measurement locations arranged in 5 semicircular rings (r_0-r_4) of 30 sensors each. θ starts at the bottom location and rotates counter-clockwise toward the top.	113
6.14	$\Delta p_{\text{total}}/p_{\text{total}}$ vs annular location (θ) for rakes 0-4, for the $C_F \times 10^4 = 90.39$ case.	113
6.15	$\Delta p_{\text{total}}/p_{\text{total}}$ vs annular location (θ) for rakes 0-4, for the $C_F \times 10^4 = 110.05$ case.	114
6.16	$\Delta p_{\text{total}}/p_{\text{total}}$ vs annular location (θ) for rakes 0-4, for the $C_F \times 10^4 = 130.06$ case.	114
A.1	Control volume definition for the derivation of the power balance equations. Modified from the original figure from Drela's power balance paper [2].	131

LIST OF TABLES

3.1	Temperature and pressure conditions used for verification cases.	45
4.1	Reference values used in the nondimensionalization.	66
4.2	Boundary layer height at the nacelle lip for podded and BLI configurations. . .	67
5.1	Reference values used in the force nondimensionalization	81
5.2	Optimization problem for the fuselage aeropropulsive design.	84
6.1	Reference values for force normalization.	100
6.2	Optimization problem definition for the aero-propulsive design of the propul- sion system without a distortion constraint.	106
6.3	Optimization problem definition for the aero-propulsive design of the propul- sion system with a distortion constraint.	108
6.4	Optimization results for the 3-D STARC-ABL aeropropulsive optimization with and without a distortion constraint	109

LIST OF APPENDICES

A Derivation of Power Balance Method	131
---	------------

LIST OF ABBREVIATIONS

- CFD** Computational Fluid Dynamics
MDO Multidisciplinary Design Optimization
BLI boundary layer ingestion
PSC power saving coefficient
FEA finite element analysis
RANS reynolds averaged Navier Stokes
MDF multidisciplinary design feasible
IDF individual design feasible
XDSM extended design structure matrix
MAUD modular analysis and unified derivatives
UDE unified derivatives equation
NPSS Numerical Propulsion System Simulation
FPR fan pressure ratio
FFD free form deformation

ABSTRACT

Within a few years of the first jet engine powered aircraft entering military service, engineers proposed a tightly coupled aeropropulsive concept called boundary layer ingestion (BLI) that could offer reduced aircraft fuel burn. The central idea was that the jet engine, essentially a massive air pump, would ingest the boundary layer air and thereby reduce aircraft drag and improve propulsion system efficiency at the same time. Although a promising idea, BLI failed to catch on at the time due to a combination of computational limitations and the availability of easier to achieve performance gains. More recently though, BLI concepts have seen renewed interest. Due to the increased computational power and developments in the field of multidisciplinary design optimization RANS CFD is now a viable design tool for early stage aircraft design and which has now opened the door to the design of BLI propulsion systems.

This thesis presents a detailed aeropropulsive study of the aft-mounted BLI propulsor for NASA's turboelectric STARC-ABL aircraft. The multidisciplinary modeling was performed using a fully coupled model built with RANS CFD and newly developed 1-D thermodynamic propulsion analysis. First an aeropropulsive study is presented that investigates the fundamental interactions between aerodynamics and propulsion and provides a quantitative analysis of the relative contributions of each to the overall BLI gain. The results show that both contribute equally to the overall BLI effect and that in order to accurately capture each contribution fully coupled aeropropulsive models are required. Next the results of a performance and sizing study for the aft-mounted BLI propulsor are presented. These results were generated with a simplified 2-D aerodynamic model of the STARC-ABL configuration. The study was performed using efficient gradient based optimization with

analytic derivatives in order to enable investigation of the large design multidisciplinary space. The sizing study shows that STARC-ABL could use between 1% and 4.6% less energy at cruise compared to a non BLI aircraft, depending on assumptions made about the efficiency of the turboelectric power transmission system. Last a more detailed study of the aft-mounted BLI propulsor was performed using a 3-D aerodynamic model that included the wings, vertical tail, and full fuselage. The 3-D aerodynamic effects create inlet distortion, which was mitigated using design optimization. The results compare the BLI efficiency with and without the presence of distortion, demonstrating that while it is possible to reduce the distortion doing so comes at the cost of reduced BLI efficiency.

Collectively the results in this thesis represent the first aeropropulsive design studies of the STARC-ABL performed with fully coupled models. The studies were made possible through the development of new design methods that leveraged gradient based optimization with analytic derivatives. The efficiency of that approach enabled multiple optimizations to be run to conduct the design studies presented here. The results of those studies have demonstrated the potential for BLI to offer significant improvements to aircraft performance and motivate continued future work.

CHAPTER 1

Introduction

1.1 Background

Boundary layer ingestion is an aeropropulsive concept that tightly integrates the aerodynamics and propulsion system of an aircraft in order to achieve more efficient flight. The basic idea is that the propulsion system can produce the same thrust for less input power by ingesting air that has been slowed down via viscous effects in the boundary layer around the aircraft. From an aerodynamic centric perspective, boundary layer ingestion (BLI) can be understood as the propulsion system ingesting a portion of the airframe viscous drag, in the limiting case completely negating it, thus making the overall system more efficient. From a propulsion centric perspective BLI can be viewed as leveraging the boundary layer to reduce the engine inflow velocity, and thus reducing the ram drag, making the overall system more efficient.

Both perspectives are reasonable ways to interpret the basic mechanisms by which BLI achieves performance improvements. The reality is that BLI systems gain performance benefits from both aerodynamic and propulsion contributions that are not easily separated from each other, but discipline specific perspectives do provide significant insight none the less. Despite the potential performance gains, to date no commercial or military aircraft in production exploits BLI. The lack of BLI propulsion system on any aircraft is perhaps even more surprising when you consider that the basic idea is nearly as old as the jet engine itself. Frank Whittle of the UK and Hans von Ohain of Germany both independently invented their own version of the jet engine in the late 1920's and early 1930's, though the first working prototype engines weren't produced until the early 1940's. The very first jet airplane, the Heinkel He 178, had its first flight in August of 1939. In 1944 the Me 262 was the first jet powered aircraft to enter military service.

In 1947 —just 3 years after the Me 262 entered service— Smith and Roberts[3] from the Douglass Aircraft Company published the first paper on BLI. Their idea was to use the

jet engine, effectively a massive air pump, to create a suction source for boundary layer control in order to reduce aircraft drag. They performed an analysis, extrapolating from experimental data that showed reduction in flat plat drag due to boundary layer suction, to estimate that a transport aircraft with a BLI propulsion system would be 25% more efficient at cruise than a more traditional decoupled design. They noted that 25% seemed overly optimistic because “[the] theory is so incomplete that one is hesitant to use it as a basis for prediction”. Despite their caution, they concluded that even if the actual benefit was lower there was still strong motivation for future investigation of the BLI concept.

Despite this very early work demonstrating a large potential for performance gain, BLI did not receive any significant additional attention for quite some time. Two additional publications related to BLI for aircraft applications were published in 1960[4] and 1970[5] as internal technical documents at the McDonnell Douglas Aircraft Company, but these were not publicly available. No other publications on BLI for aircraft applications appear in the literature until the 1990’s.

Though no aerospace applications were produced, BLI propulsion did find use in naval applications with the most obvious use case being for torpedo designs. A number of academic publications on “wake ingestion”, an alternate term for BLI, were published by Wislicenus and Smith[6], Gearhart and Henderson[7], and Brue et al.[8]

In 1966 Betz[9] published an analysis that showed that propulsive efficiency of wake ingestion based systems could exceed 100%, because the power expended to propel a craft could be less than the product of its velocity times its drag. An efficiency greater than 100% indicates a poor definition for said efficiency, so Betz’s analysis was the first to formally demonstrated that traditional thrust vs drag accounting methods are not directly applicable to aeropropulsively coupled systems. The fundamental challenge, which Betz had touched on, is that when aerodynamic and propulsion systems interact strongly the concept of independent thrust and drag quantities begins to break down. When using a thrust-drag accounting system, there is an inherent assumption that the two quantities are independent. By design, this assumption is appropriate for a traditional tube-with-wings aircraft configuration because the airframe and propulsion systems are intentionally decoupled. For BLI systems this assumption no longer holds, and thrust-drag based accounting becomes complicated by the need to include interactions terms for propulsion effects on drag and airframe effects on thrust.

Although Betz was the first to publish work that touched on the challenges of using a thrust-drag based accounting system, he offered no remedy for the problem. The first solution was proposed by Leroy Smith[10] in a 1993 paper that analyzed the BLI benefit using a new metric, that Smith termed power saving coefficient (PSC). He defined the PSC

as

$$PSC = \frac{Pwr'_{\text{shaft}} - Pwr_{\text{shaft}}}{Pwr'_{\text{shaft}}}. \quad (1.1)$$

The key concept in the PSC is that comparisons between BLI and non-BLI configurations are performed by computing the power required to achieve a given net force, F_{net} , on the entire body (airframe and propulsor) without distinguishing between individual thrust and drag contributions of sub-systems. This metric compared the power required by a BLI configuration (Pwr_{shaft}) to the power required by a podded configuration (Pwr'_{shaft}), assuming the same net net force on the body (F_{net}). The PSC thus represents the fractional savings of the BLI system relative to comparable podded system. If the aircraft is assumed to be at steady cruise then the F_{net} should be zero, but if the aircraft is accelerating or decelerating then the F_{net} could be a positive or negative quantity. Regardless of the prescribed value of F_{net} , the core idea is that the two configurations are compared via the power required. Smith computed the PSC for a range of different wake shapes, concluding that BLI systems could use up to 50% less power than an equivalent free stream propulsors to produce the same net force.

Leroy Smith's work[10], with the benefit of nearly 50 years of additional research into boundary layer flows and considerably more experimental and empirical data, was significantly more advanced than the original 1947 work of Smith and Roberts[3]. Despite the more complete analysis and the demonstrated potential BLI still failed to attract significant additional research or practical implementations. It is my opinion that a major contributing factor to the lack of interest in BLI was the fundamental difficulty in accurately predicting boundary layer flows for arbitrary shapes. Despite the promise clearly shown by prior research, when it came to the practical task of designing actual BLI systems the challenge was ensuring high performance over a wide range of operating conditions for a tightly coupled aeropropulsive system. No low-fidelity tools existed to provide accurate boundary layer predictions for arbitrary 3-D bodies, and although reynolds averaged Navier Stokes (RANS) Computational Fluid Dynamics (CFD) models were first developed in the 1970's[11] they did not start to become practical for general aircraft applications till the 1990's[12]. Methods for using RANS CFD with numerical optimization weren't developed until the early 2000's[13]. It is worth noting that aerodynamic design, via optimization methods, using potential flow and Euler CFD was being researched in the late 1980 's and 1990's[14, 15, 16, 17]. However, these techniques were not applicable to BLI problems because they had only been developed for inviscid analyses. The lack of low fidelity models for viscous flows and the high computational cost of RANS CFD meant that

there was no ability to produce coupled aeropropulsive models to design aircraft with. The modeling difficulties combined with the fact that there was still significant performance to be gained by optimizing the aircraft aerodynamics and propulsion systems separately limited motivation to tackle the challenges of designing an aeropropulsive BLI system.

Starting in the late 1990's and early 2000's, experimental and theoretical research on BLI propulsion began to appear more frequently in the literature. In 1999 Anabtawi[18] published experimental results examining flows in a BLI inlet with an s-duct design showing the potential need for vortex generators to maintain adequate inlet total pressure recovery. In 2001 Rodriguez[19] published the first Multidisciplinary Design Optimization (MDO) of a BLI inlet, including the use of RANS CFD for aerodynamic modeling. In 2009, Drela[2] dramatically expanded on Smith's ideas around power based accounting, developing a complete power based bookkeeping scheme for aeropropulsively coupled aircraft that he called the "power balance method". Drela's power balance method has proved to be an important tool for the conceptual design of aeropropulsive systems, and has been used heavily for conceptual design studies of BLI propulsion systems.



Figure 1.1: Artist conception of a notional BWB or HWB aircraft.

Along with the new experimental and theoretical BLI research, a number of new unconventional aircraft concepts were proposed that leveraged BLI as part of an overall design meant to achieve lower fuel burn. A series of three papers from researchers at Boeing examined a blended wing body configuration, similar to the artist conception shown in Figure 1.1, with and without BLI propulsion in the form of embedded engines with s-duct inlets[20, 21, 22] which predicted between 6% and 10% improved fuel burn compared to a similar technology level tube-with-wings aircraft. In 2007 Plas et al. published a study that predicted the BLI propulsion system on a blended wing body fuselage could achieve lower

3%-4% fuel burn than the same airframe with podded engines. In 2010 and 2011 a series of three papers from Greitzer et al.[23] and Drela[24, 25] proposed a super-wide body aircraft concept, they termed the D8 “double bubble”, predicting 7% fuel burn reduction compared to a similar technology level tube-with-wings configuration. An artist conception of the D8 configuration is shown in Figure 1.2



Figure 1.2: Artist conception of a notional D8 aircraft concept with top, aft mounted BLI propulsion system.

All of these proposed aircraft used traditional gas turbine engines as the heart of their propulsion system, but in 2009 Felder and Kim [26] proposed a more radical application of BLI with a turboelectric propulsion system. Their goal was to use electric motors to create a distributed propulsor that consumed the majority of the boundary layer air from the top surface of the fuselage, thus maximizing the BLI benefit and giving a predicted 12% fuel burn savings. An artist conception of their aircraft configuration in Figure 1.3 shows the aircraft’s most distinct feature, the BLI mail slot inlet. More recently in 2016 Welstead and Felder[27] proposed a much less unconventional turboelectric concept, named the STARC-ABL, which used a tube-with-wings fuselage combined with an electrically powered aft mounted propulsor to achieve fuel burn reductions of around 6%. The STARC-ABL aircraft is depicted, with its aft mounted propulsor, in Figure 1.4. The STARC-ABL configuration is a particularly interesting concept from a practical point of view, because the airframe is essentially a conventional tube-with-wings, that achieves lower fuel burn via a more limited application of BLI. The traditional fuselage means the concept is much closer to a typical aircraft and can be designed using more typical methods, if reasonable estimates for the performance of the turboelectric BLI system can be made. Of course, that means that getting estimates of the BLI performance is still the key challenge to overcome.

The wide range of predictions for the overall impact of BLI was partly due to the range of different aircraft configurations that were investigated. However, there was also large variations in the results because of the different techniques that were used to estimate the effects of the aeropropulsive coupling from the BLI on the aerodynamics and propulsion. With the exception of Rodriguez's work, all of the aeropropulsive models were built using an uncoupled or weakly coupled modeling approach that mainly captured the aerodynamic impact on propulsion but not vice versa.

Rodriguez's work was multidisciplinary because he coupled his aerodynamics model to a 1-D propulsion model in order to compute fuel-burn and to capture the impact of the propulsion system on the inlet boundary conditions, but his design optimization problem could only handle about 25 designs variables because he was using the costly complex-step method to compute derivatives. To keep the computational budget reasonable, Rodriguez limited his design space to a set of somewhat limited shape variables for the inlet and didn't include gross design variables like inlet diameter or any propulsion design variables. Rodriguez's conclusions were that the BLI propulsion system underperformed relative to a podded configuration, but his results were not definitive because of the limited design problem that he was able to solve using the somewhat inefficient methods available and the high compute cost of the RANS aerodynamic analysis. Although Rodriguez's work repre-



Figure 1.3: Artist conception of a notional BWB aircraft with a turboelectric distributed propulsion system.

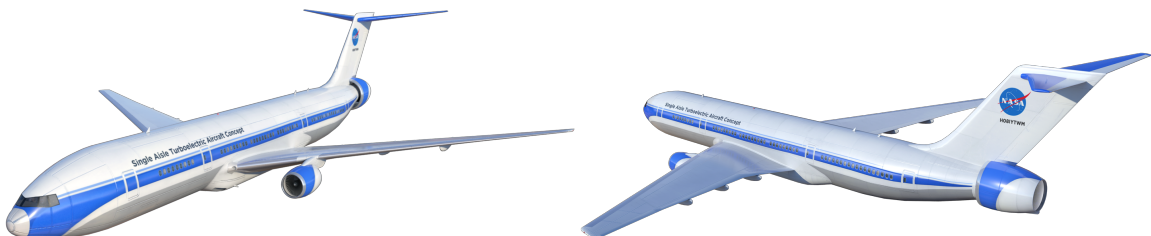


Figure 1.4: Artist conception of the STARC-ABL aircraft with a turboelectric BLI aft mounted propulsor.

sented a significant advancement toward the ability to design BLI systems, the difficulties he encountered served to validate the choice by engineers to shy away from BLI concepts when there were similar performance gains to be had by optimizing the subsystems by themselves.

In this thesis, I seek to overcome these challenges and help open the door a little wider to realizing a BLI based aircraft. I have developed a method for designing BLI propulsion systems, using a fully coupled aeropropulsive design optimization technique. I leverage gradient based optimization with analytic derivatives to achieve the computational efficiency necessary to include both aerodynamic and propulsion design variables in the design problem. The work presented here analyzes the performance of the aft-mounted BLI propulsor for NASA's STARC-ABL aircraft, and uses design optimization to present the first complete aeropropulsive sizing results for that configuration. This thesis demonstrates that with the combination of modern MDO methods, efficient adjoint based RANS CFD solvers, and a newly developed propulsion model it is now possible consider BLI propulsion systems in the early design phases for an aircraft concept.

1.2 How BLI works

BLI involves a complex interaction between the aircraft aerodynamics and the propulsion system where each one affects the other, with the result being higher overall performance. It is possible to analyze a BLI system from either an aerodynamic or propulsive perspective which can attribute the BLI gains to different affects. In some cases, a particular analysis seeks to associate the entire BLI performance gain to either aerodynamics or propulsive effects but, as Chapter 4 will demonstrate, the reality is that both aerodynamic and propulsive impacts are occurring simultaneously and contributing equally to the overall effect.

In this section I summarize an existing aerodynamic focused analysis from Drela [2] and present a new propulsion focused analysis that I developed using common terminology with the goal of explaining the fundamental mechanisms through which BLI creates improved performance. Drela's aerodynamic analysis is more general, and has the potential to capture the full aeropropulsive coupling. The propulsion focused analysis is more limited in scope, but provides much greater insight into the fundamental effect of BLI on a propulsor. Comparing and contrasting the two analysis approaches gives an overall perspective of the the BLI mechanisms.

1.2.1 An aerodynamic perspective

Drela's [2] power balance method presents an aerodynamic BLI perspective, based on a particular control volume analysis. A detailed derivation of the power balance equations is provided in Appendix A.

For jet propelled aircraft in steady level flight, the power balance equation is

$$P_k + P_s = \dot{\mathcal{E}} + \Phi, \quad (1.2)$$

where P_k is the net power being expended by any jet propulsion system, P_s is the net power being produced by all the viscous wall surfaces (i.e. fuselage, wing, and propellers), $\dot{\mathcal{E}}$ is the net pressure-work and kinetic energy flow rate out of the control volume (measured on a Trefftz plane), and Φ is power lost to viscous dissipation. This equation holds whether or not an aircraft uses a BLI propulsion system.

The fundamental goal of BLI is to reduce the P_k and P_s terms, reducing the amount of power required to fly the aircraft. P_k is defined as

$$P_k = \iint - \left[p + \rho \frac{1}{2} V^2 \right] \vec{V} \cdot \hat{n} \, dS_{body}^{flow}, \quad (1.3)$$

which is essentially equal to the net power produced by any jet propulsion system.

The P_s term, defined as

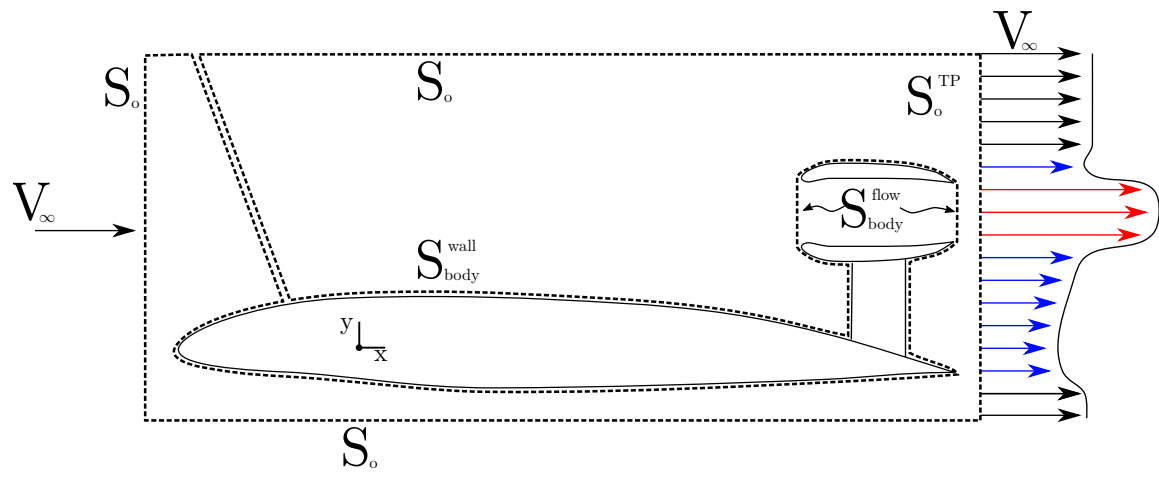
$$P_s = \iint - [p\hat{n} + \vec{\tau}] \, \vec{V} \, dS_{body}^{wall}, \quad (1.4)$$

has a more complex interpretation. This term is integrated over every solid wall surface of the body, including the wings, tail, fuselage, and propellers. So this term includes any viscous and pressure forces on all the wetted area of the airframe. If the aircraft was purely propeller driven, then this term would obviously need to be net negative — note the negative sign in Equation (1.4). However, if the aircraft was purely jet powered then this term would end up being positive (representing a net loss of power to the overall system). Either way, the goal would be for the magnitude of P_s to move closer to zero.

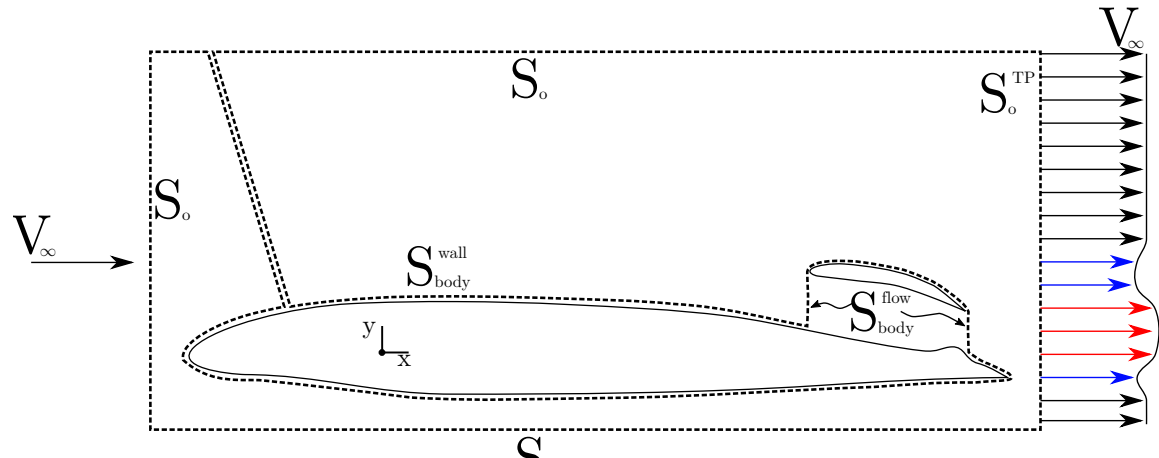
Equation (1.2) says that in order for BLI to yield a lower $P_k + P_s$, it must also decrease least one of the two right hand side terms: $\dot{\mathcal{E}}$ and Φ . For the notional example in Figure 1.5, $\dot{\mathcal{E}}$ is defined as

$$\dot{\mathcal{E}} = \iint_{S_o^TP} \left[(p - p_\infty) + \frac{1}{2} \rho (V^2 - V_\infty^2) \right] V \, dS_{TP}. \quad (1.5)$$

Because of the $(V^2 - V_\infty^2)$ term in Equation (1.5), $\dot{\mathcal{E}}$ is highly sensitive to non-uniformities



(a) podded configuration



(b) BLI configuration

Figure 1.5: Integration surface definitions for notional podded and BLI propulsor configurations. S_{body} is the propulsion control volume. S_{TP} is the Trefftz plane.

in the velocity profile along the Trefftz plane (S_{TP}). Anything that can be done to make the velocity profile on the Trefftz plane more uniform will reduce the integrated $\dot{\mathcal{E}}$ value and hence reduce P_k . This is the source of the increased propulsive efficiency gained via BLI, which was first noted by Betz [9] and is often cited in more propulsion centric discussions. $\dot{\mathcal{E}}$ can broadly be thought of as the propulsive contribution to the BLI benefit. This is a simplification because the sections of the flow that display a velocity deficit along the Trefftz plane are caused aerodynamic losses from the fuselage. The velocity increment from the propulsion system is the most significant effect, so it is reasonable to consider $\dot{\mathcal{E}}$ as mainly a propulsive term related most closely to P_k .

BLI benefit can also be gained by reducing Φ , defined as

$$\Phi = \iiint_V (\bar{\tau} \cdot \nabla) \cdot \vec{V} dV, \quad (1.6)$$

which is an integral of the stress tensor ($\bar{\tau}$) over the entire control volume. This term captures viscous dissipation in the flow from various different sources such as friction drag on the airframe, mixing losses in the wake, and shock losses. For a first approximation, using this simple 2-D case, Φ can be thought of as representing the viscous drag of fuselage. This is a different mechanism for BLI performance gains than reductions to $\dot{\mathcal{E}}$, and does not come from a change in the propulsive efficiency of the system. Examples of effects that contribute to lower Φ include reduced nacelle installation drag, reduced whetted area of the configuration, and reductions in viscous drag on the fuselage upstream of the propulsor inlet. Due to the relationship with viscous drag, Φ can be thought of as an aerodynamic contribution to the BLI benefit most closely associated with P_s . Again, this is a simplification because there are propulsion related factors that influence this term as well. Broadly though, characterizing Φ as related to aerodynamics is reasonable.

In Chapter 4 I examine the relative importance of the aerodynamic and propulsive contributions and show that for an aft-mounted propulsor configuration like STARC-ABL they are roughly equal importance to the overall BLI effects. Similar results were also found via by Hall et al. [28] when examining the D8 aircraft configuration. This means that a BLI propulsion system reduces both $\dot{\mathcal{E}}$ and Φ , and consequently P_k and P_s , by roughly equal amounts.

1.2.2 A propulsive perspective

BLI can also be understood from a more propulsion focused perspective, by using a traditional propulsion control volume approach and 1-D averaged flow quantities. The 1-D

form of propulsion analysis is used by pyCycle and NPSS [29, 30], and is the most widely used method for studying propulsion system performance. This style of analysis provides insight into the mechanism by which the propulsor gets more efficient by showing that BLI effectively modifies the propulsor inlet conditions in a way that mimics slower flight speeds. Here we use a propulsion centric control volume that focuses only on the airflow passing through the propulsor itself, as shown in Fig. 1.6.

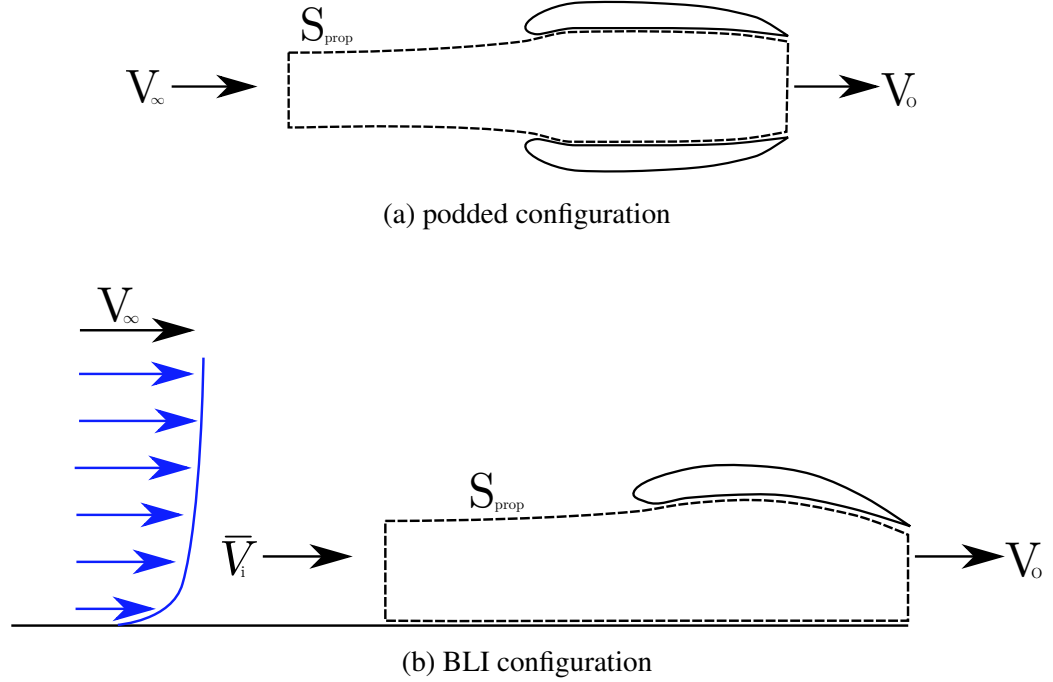


Figure 1.6: Propulsion centric control volumes for the podded (top) and BLI (bottom) configurations.

For the control volume defined by S_{prop} in Figure 1.6 (a), neglecting any added mass from the combustion of fuel or frictional losses within the control volume, the net thrust normalized by free stream velocity is computed as

$$\frac{F_{\text{net}}}{V_{\infty}} = \dot{m} \left(\frac{V_o}{V_{\infty}} - \frac{V_i}{V_{\infty}} \right) + \frac{1}{V_{\infty}} [(p_o - p_{\infty})A_o - (p_i - p_{\infty})A_i]. \quad (1.7)$$

Equation (1.7) bears a strong similarity to the definition for P_k in Equation (1.3). Though one equation gives thrust and the other power, the two are related. However care must be taken in comparing them because the control volumes that they are evaluated over are different, due to the inflow plane of S_{prop} extending far out ahead of actual inlet. In a propulsion centric analysis, this is done to simplify the thrust equation by ensuring that the velocity and static pressure at the inflow plane are equal to the free stream quantities. This

is not the case if the inflow plane is placed at the inlet highlight, as is done for the control volume defined for the P_k equation.

For the sake of simplicity, assume that the nozzle has been designed to be perfectly expanded so that $p_o = p_\infty$. I have already noted that the inflow plane (denoted by the subscript i) is selected such that $p_i = p_\infty$. With those assumptions the pressure related terms of Equation (1.7) drop out and all that is left are the impulsive terms:

$$\frac{F_{\text{net}}}{\dot{m}V_\infty} = \frac{V_o}{V_\infty} - \frac{V_i}{V_\infty}. \quad (1.8)$$

Now consider the power added to the flow, which is equal to the change in kinetic energy flux ($\Delta \dot{\text{KE}}$) across the control volume. For a simple electric propulsor, the power addition to the flow comes from the fan adding total pressure which the nozzle converts into velocity at the exit plane of the control volume. $\Delta \dot{\text{KE}}$ can be related to the change in velocity across the control volume with Equation (1.9), which be rearranged to provide the ratio of V_o/V_∞ , given a known input power and flight speed and inflow velocity.

$$\frac{\Delta \dot{\text{KE}}}{V_\infty^2} = \frac{1}{2}\dot{m} \left(\left(\frac{V_o}{V_\infty} \right)^2 - \left(\frac{V_i}{V_\infty} \right)^2 \right) \quad (1.9)$$

$$\frac{V_o}{V_\infty} = \sqrt{\frac{2}{\dot{m}V_\infty^2} \Delta \dot{\text{KE}} + \left(\frac{V_i}{V_\infty} \right)^2}. \quad (1.10)$$

For the traditional podded engine configuration $V_i = V_\infty$ because the inflow plane has been chosen intentionally so that is the case. For the BLI configuration the viscous losses in the boundary layer ensure that the average inflow velocity (\bar{V}_i) will always be less than the free stream velocity. Exactly how much less will be a function of the amount of boundary layer air that a BLI propulsor consumes, but it will always be true that $\bar{V}_i < V_\infty$.

Equation (1.8) and (1.10) are both non-dimensional. Equation (1.8) provides a net thrust normalized by what is commonly referred to as ram drag ($\dot{m}V_\infty$). Equation (1.10) includes a non-dimensional power addition term ($\frac{2}{\dot{m}V_\infty^2} \Delta \dot{\text{KE}}$) that I will refer to as \dot{Q} . We can assume any arbitrary value for \bar{V}_i/V_∞ that is less than 1, and then consider a series of different values for \dot{Q} . The top graph in Figure (1.7) plots Equation (1.10) using those assumptions, showing that the outflow velocity is effectively independent of the average inflow velocity, and is only a strong function \dot{Q} . Higher \dot{Q} gives a higher outflow velocity.

Since V_o/V_∞ is effectively independent of \bar{V}_i/V_∞ for any BLI configuration, then via Equation (1.8) we see that the gains from BLI must come solely from a reduction in \bar{V}_i/V_∞ itself. This means that the mechanism by which BLI achieves improved propulsion performance is to leverage the work done on the flow by the viscous effects in the boundary

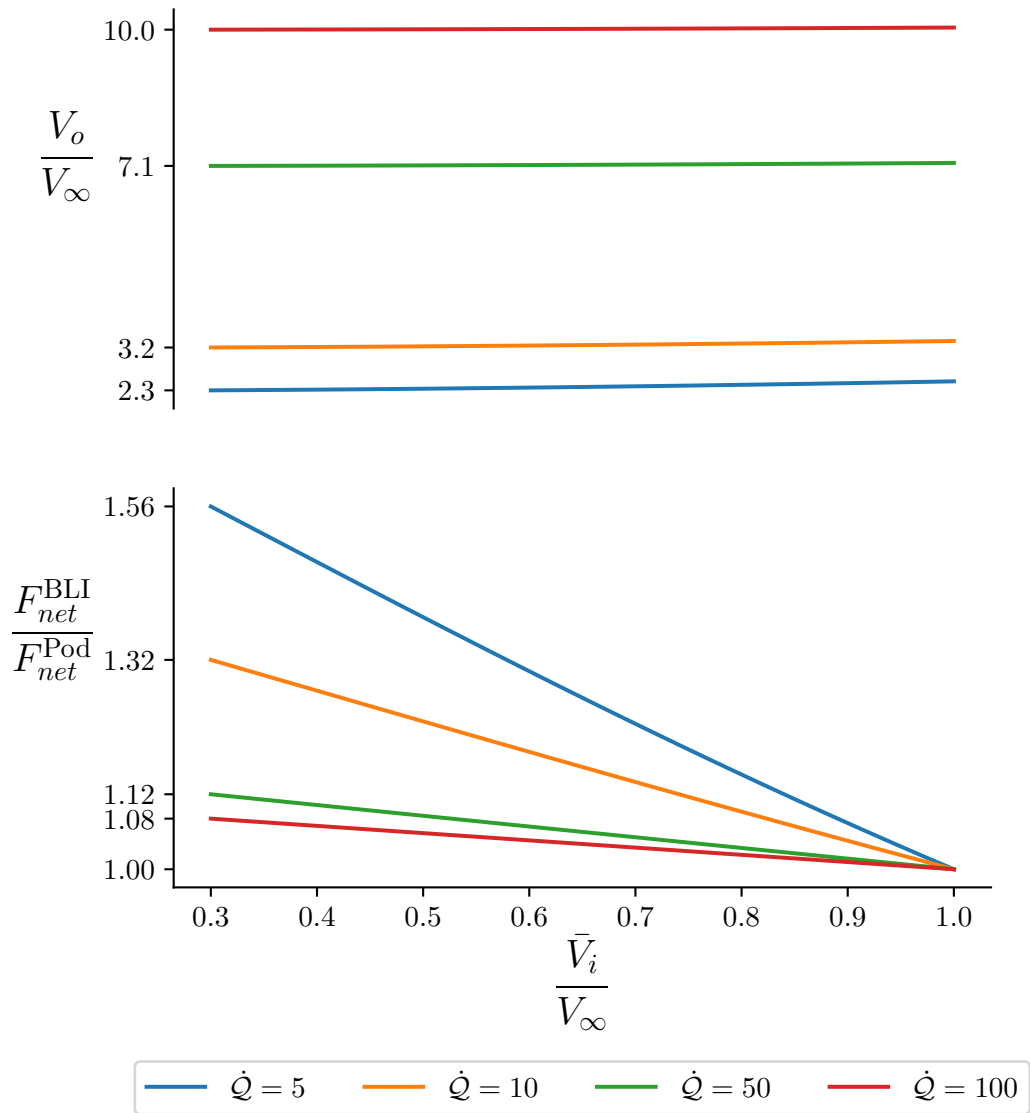


Figure 1.7: Normalized outflow velocity as a function of normalized average inflow velocity for four different values of the normalized energy addition (\dot{Q}).

layer to reduce the ram drag term in the thrust equation. In other words, BLI essentially creates a situation where the propulsion system is flying slower than free stream velocity and hence is more efficient. The efficiency gain is shown in the bottom graph of Figure 1.7, which plots the ratio of Equation (1.8) computed with \bar{V}_i to the reference value computed with $V_i/V_\infty = 1$ (representing the podded configuration). Figure 1.7 shows that BLI has the highest impact for lower values of \dot{Q} .

The actual value of \dot{Q} needed by any given aircraft to maintain steady flight will be function of the aircraft size and the propulsion system design, but Figure 1.7 fundamentally shows that for the same \dot{Q} the BLI configuration will produce more net thrust than the podded configuration. Figure 1.7 also shows that lower \dot{Q} designs would achieve better performance gains from BLI. If one assumes a constant ΔKE and V_∞ , then \dot{Q} can be lowered by increasing \dot{m} . For a traditional turbofan engine cycle, higher \dot{m} would correspond to a higher bypass ratio design. So one important conclusion from Figure 1.7 is that the higher bypass ratio of a given propulsion system, the more it will benefit from BLI.

It is worth noting that the BLI effect does not come for free, because the boundary layer that causes $\bar{V}_i/V_\infty < 1$ also creates viscous drag on the aircraft. So one might ask if the improvement in BLI efficiency is enough to overcome the added drag from the boundary layer. To answer that note that the aircraft will produce a boundary layer, and hence the viscous drag, no matter what. So the propulsive effect from BLI can fundamentally be understood as of exploiting work already being done by the airframe to yield improved propulsion performance.

It is also important to reiterate that this propulsion centric analysis is not capable of capturing the complete BLI effect, because it does not capture any changes to the surface pressure distribution or viscous drag on the fuselage. The analysis is useful in gaining insight into how the propulsor itself reacts to BLI, but a more complete analysis is necessary to capture the full BLI effects.

1.2.3 A note about total pressure loss

Inlet total pressure loss is a crucially important parameter in propulsion system design. Traditionally, total pressure losses arise from inefficiency in the propulsion system inlet itself and are detrimental to overall propulsion performance. High inlet total pressure losses, or low inlet total pressure recovery, translates to a loss of specific thrust (F_{net}/\dot{m}) from the propulsion system. In a typical podded configuration, where the thrust required at any given flight condition can be considered a fixed value then a loss of specific thrust translates into the need for a larger propulsor which will weigh more and burn more fuel.

In the above section I show that boundary layer ingestion has an equivalent effect to flying at a lower flight speed. At a constant altitude, with a constant atmospheric static pressure, total pressure is given by

$$p_{\text{total}} = p_{\text{static}} \left(1 + \frac{\gamma - 1}{2} M N^2 \right)^{\frac{\gamma}{\gamma-1}}. \quad (1.11)$$

Equation (1.11) indicates that an effective lower flight speed will also yield a lower inlet total pressure. Given the deleterious effects of inlet total pressure loss for podded configurations it is, perhaps, intuitive to assume that total pressure loss due to BLI will also have a negative impact. In both cases, the loss of total pressure will reduce \dot{m} through the engine for a fixed propulsor size. However, in the case of inlet total pressure loss the only effect is reduced \dot{m} , and hence a lower specific thrust. In the case of BLI the propulsion system sees a reduced \dot{m} but also a reduced \bar{V}_i (ram drag). The velocity effect is the dominant one, as shown by the increase in relative net thrust vs reduced \bar{V}_i/V_∞ in Figure 1.7. Thus, for the same reason that we do not worry about loss of total pressure when we are flying slower, the loss of total pressure due to BLI is not deleterious to performance.

1.3 BLI research using uncoupled modeling methods

The increasing number of publications on the subject of BLI starting in the late 1990's, covered in Sec. 1.1, indicates a growing interest in the subject. The overwhelming majority of the research performed on BLI concepts has been done using uncoupled analysis methods that do not fully capture the effect of aeropropulsive coupling.

I use the term "uncoupled" to describe models that capture the affect of the aerodynamics on the propulsion system or vice versa, but not both simultaneously. BLI propulsion systems are inherently aeropropulsively coupled, so an uncoupled modeling approach can only loosely approximate the performance of such a system. Still, uncoupled models play an important role in studying BLI propulsion systems. Most significantly, they allow engineers to make first cut approximations of BLI performance that serve to guide more detailed research and identify the most promising concepts.

With RANS CFD methods becoming practical for transonic aircraft applications in the 1990's[12], and gaining broad adoption in the 2000's, aerodynamicists finally had the right modeling tool to predict boundary layer flows for arbitrary 3-D bodies at relevant Reynolds numbers. Despite its availability, its suitability for use in aeropropulsive design was still very limited. In the mid 2000's, RANS CFD analyses of full aircraft still took 10's of hours to days to run a single case. If running a single RANS CFD analysis wasn't expensive

enough, using it for a coupled aeropropulsive analysis was a significantly more expensive proposition. In 2001 Rodriguez[19] presented an aerodynamic shape optimization that used a coupled aeropropulsive model work served as the blueprint for accomplishing that coupling, one which my own work presented here follows. However his optimization results, lacking any propulsion system design variables such as fan diameter or pressure ratio, showed that BLI actually underperformed compared to the reference podded configuration. His results, which ran counter to the other uncoupled analysis that came before, demonstrate just how challenging a task aeropropulsive coupling can be from a modeling and design standpoint.

So despite the technical capability to build fully coupled aeropropulsive models, the practical reality in the early and mid 2000's was that fully coupled modeling wasn't yet a viable option for designing BLI propulsion systems. Hence, while uncoupled models are fundamentally limited in their ability to accurately predict detailed performance metrics for BLI propulsion systems they nevertheless served an important role in the conceptual design of the newly proposed aircraft concepts that sought to include BLI in their technology suite.

1.3.1 Conceptual aircraft design studies

The D8 aircraft concept is the most widely studied aircraft concept among those that include a BLI propulsion system. It was first proposed by Greitzer et al.[23, 25] as part of a conceptual design funded via NASA NRA grant. During that work Drela performed an uncoupled design optimization for the D8 configuration using a custom designed multilevel optimization scheme. Since then, the concept has been the center of a number of theoretical and experimental studies that have helped to validate some of the early performance predictions.

The D8 concept was tested NASA Langley's 14x22 ft subsonic wind tunnel in 2013, with initial results presented by Uranga et al. in mid 2014 [31] showing that the BLI benefit was $(6 \pm 2.3)\%$ reduced power required. At the same time, numerical studies conducted by Pandya et. al [32], using RANS CFD analyses with actuator zone models for the propulsors predicted a 9% reduction in power required. In 2017 Uranga et al. [33] published an updated analysis that attempted to isolate the BLI benefit for the D8 configuration by comparing data from a wind tunnel model with and without a BLI propulsor configuration. This updated analysis concluded that BLI itself reduced the power required for steady flight by $(8.6 \pm 1.8)\%$. NASA also published its own series of analyses conceptual design studies on the D8 that largely agreed with the other predictions [34, 35].

Another highly researched configuration is the hybrid wing body (a.k.a blended wing body or flying wing) aircraft concept. The first work on this concept came from researchers at Boeing [20, 21, 22], as discussed in Section 1.1. The original concept had 3 traditional engines embedded inside the fuselage, with BLI inlets connected via s-ducts. In 2009 Felder et al. [26] proposed a dramatic extension of this aircraft configuration via the addition of a turboelectric distributed propulsion system and a mail-slot inlet. Their idea was to utilize wing-tip mounted gas turbine engines as generators, to power a series of small distributed electric propulsors along the upper surface of the combined fuselage and wing. The goal of this re-design was to allow the propulsion system to ingest a larger portion of the boundary layer and achieve greater than 50% lower fuel burn compared to a Boeing 777 baseline. Although the distributed propulsion idea was novel it relied heavily on a number of technologies that were either in their infancy or did not exist at all, such as superconducting motors and hydrogen powered flight weight cryogenic cooling systems. The radical nature of the design, combined with the low technology readiness of crucial systems made this concept unattractive. The aggressive turboelectric concept was not feasible, it did inspire the later development of a more realistic BLI aircraft concept: the STARC-ABL.

In 2016 Welstead and Felder [27] proposed STARC-ABL as a new aircraft concept with a turboelectric BLI propulsion system and a much more realistic airframe configuration. The central aspect of this concept was that it maintained a nearly totally traditional airframe, with aerodynamic and structural changes limited to the tail section to support an aft mounted propulsor. In order to power that aft mounted propulsor, they proposed using a turboelectric propulsion system with power produced by generators attached to the low pressure spools of the two under-wing mounted engines sent to the back of the fuselage where it turned an electric motor mounted to a fan. This is highlighted via the red arrow in Figure 1.8, which shows the power moving from the generators two generators (one under each wing) to the aft propulsor.

The original publication by Welstead and Felder predicted a 12% fuel burn reduction for the STARC-ABL concept. This was a monumental result, especially considering the relative conventional nature of the aircraft configue, that inspired me to focus on this aircraft concept for my thesis research. Unfortunately subsequent independent analysis both by the original authors and by myself has revised that original figure down to between 1% and 5% fuel burn reduction. Though a much less impressive figure, it still offers hope for a highly impactful application of BLI. My own research into this concept will be presented in detail throughout the body of this thesis.

1.3.2 Aerodynamics focused investigations

There has been a number of publications that have focused more on the aerodynamic side of BLI propulsion systems. This research all takes a specific configuration as a given assumption and then examines the aeropropulsive interactions caused by the BLI system from a distinctly aerodynamic perspective. As such the work often assumes a constant propulsion system design, meaning that the key defining characteristics of the propulsion system (i.e. fan pressure ratio, fan diameter, thrust level, etc.) are either held fixed—in other words, the propulsion system is not being designed.

The earliest example of this aerodynamically focused work is that of Rodriguez [19]. Rodriguez's work used powered boundary conditions, consisting of an inflow and outflow plane that represented the interface to the propulsion system. More recently, Blumenthal et al. [36] added a flat actuator zone to the CRM aircraft geometry [37] to simulate an aft mounted thruster and performed aerodynamic shape optimization on the aft fuselage. They concluded that the best geometry for a BLI and a non-BLI system were different and that additional performance gains could be had by tailoring the fuselage shape to suite the BLI configuration.

One of the major practical challenges for BLI propulsion is the presence of inlet distortion, which is problematic for the structural design of the fan. In the best case scenario, high distortion levels will cause only an increase in fan weight to provide a strong structure. In the worst case scenario, the fan efficiency will be compromised to provide a wider aerodynamic operating zone. The aft propulsor provides an interesting case to study distortion because, at least in theory, the mostly axisymmetric fuselage will provide a mostly axisymmetric distortion pattern that is potentially less undesirable from a fan design standpoint. Due to these concerns, two sets of researchers separately studied the possibility of limiting



Figure 1.8: The STARC-ABL configuration, with the turboelectric power flow highlighted by the red arrow. Electric power is generated by generators on the underwing nacelles and sent to the aft fuselage to power an electric BLI propulsor.

inlet distortion for an aft propulsor using aerodynamic shape optimization. Ordaz et al. [38] integrated a distortion metric based on measurements of total pressure arranged in a computational rake around the inlet annulus into the FUN3D RANS CFD solver and performed optimization to minimize the distortion. They used a notional business jet as their baseline geometry, adding a aft mounted thruster and showing that they could reduce the incurred distortion by 95% compared to a very non-optimal baseline. Kenway and Kiris [39] integrated a similar distortion metric into the ADflow RANS CFD solver, and performed shape optimization at a range of different angles of attack on the actual STARC-ABL reference geometry. The initial distortion in that case was already much lower, less than 5%. Kenway and Kiris were able to reduce distortion down to less than 2% for most angles of attack. The work of these two sets of researchers, though aerodynamically focused, demonstrated that shape optimization on RANS CFD models was now a viable tool for BLI design work. They also demonstrated that the tool could be used to mitigate somewhat more detailed design issues that would be important to ensuring that an actual BLI design would be able to reach its full potential when flown.

1.3.3 Propulsion focused investigations

In a analogous fashion to the aerodynamics focused research, there has been a considerable amount of propulsion focused research as well. As before, this work assumes a configuration for the sake of measuring the impact of BLI but the focus of the research is not to develop the configuration itself. Here the work is focused on analyzing and quantifying the BLI impact from a propulsion centric perspective.

Florea et al. [40] studied BLI performance from a detailed inlet design perspective, concluding that shape optimization would allow for a modest 1.5% total pressure loss for BLI inlets compared to the 6% non-optimized baseline. Building off that work, Ochs et al. [41] extended the analysis to a full propulsor and concluded that a 4.2% overall propulsive efficiency benefit was possible with an embedded engine BLI configuration.

Work from researchers at Cranfield university focused on the modeling of the turboelectric propulsion system in a BLI context. Based on CFD results from Mantic-lugo et al. [42], Liu et al. analyzed thermodynamic cycle performance for a turboelectric distributed propulsion system by relating the BLI propulsor mass flow to an equivalent free stream mass flow using assumed boundary layer profiles.

In a 2017 paper on estimation of BLI benefits Hall et al. [28] leveraged the power balance method from Drela [2] to estimate the relative contributions of BLI from aerodynamic and propulsive performance improvements. They found that the BLI benefit was derived

40% from aerodynamic gains and 60% from propulsive gains. This conclusion is in strong agreement with my own research presented in Chapter 4.

In 2017 Arend et al. [43] presented a summary of their experimental results for a wind tunnel test of a BLI fan, conducted in the transonic section of NASA Glenn's 8x6 wind tunnel. Extensive modifications were made to the wind-tunnel to add new bleed air systems in order to replicate expected boundary layer conditions at the inlet within the test section. The test was primarily focused on measuring fan performance in the presence of strong inlet distortion, and as such UTRC collaborators designed a new fan specifically for this test. The most significant conclusion from the test was that the overall stage adiabatic efficiency was 87.9% which was 3.1 percentage points higher than the value predicted by CFD models.

1.4 Applying high-fidelity MDO to aeropropulsive design

In Sec. 1.3 I discussed a number of the most significant publications on the design of aircraft concepts that included BLI propulsion systems. The vast majority of that work was performed using an uncoupled analysis method to approximate the performance gains from BLI. There are a few examples of research performed using coupled aeropropulsive models, but in these cases only coupled analysis was performed. Turnbull et al.[44] developed a fully coupled aeropropulsive analysis using an integral boundary layer method added to a panel code, but did not perform any design optimization. Ordaz [45] developed a coupled aeropropulsive model using a RANS CFD solver and a 1-D cycle analysis tool, but was also not able to perform design optimization. Rodriguez's work[19], discussed earlier, developed an aerodynamic optimization that included some aeropropulsive modeling, but lacked propulsion design variables and used a very small design space. Save those three examples all the rest of the work done used uncoupled models. More significantly, despite aeropropulsive models being a classic example of an MDO problem, none of the prior work has leveraged the most advanced or efficient optimization techniques developed by that community because they lacked the tools to apply those methods.

Applying design optimization to aeropropulsive models is difficult because it involves conquering three challenges:

1. large numbers of design variables due to the inclusion of aerodynamic shape variables in the design space
2. optimization in the presence of expensive RANS CFD aerodynamic analyses
3. optimization in the presence of a coupled multidisciplinary models

These three challenges are not unique to aeropropulsive design problems, and in fact all are shared with aerostructural design problems. There are also many other disciplines that suffer from at least one of these three challenges as well; hence, a wide range of different techniques for addressing all them have been developed by various research communities. In the 1970's Bryson[46] developed adjoint based methods for efficiently computing derivatives of large design spaces for optimal control applications, and these methods were later adopted and refined by structural optimization[47] and aerodynamic optimization[14] researchers for their applications. Starting in the late 1990's The MDO community began working on ways to efficiently optimize coupled analysis models[48]. In the mid 2000's Martins[49, 50] extended those methods to coupled high-fidelity aerostructural applications using Euler CFD for the aerodynamic solver and finite element analysis (FEA) for the structural solver. Significant additional development on efficient gradient based optimization of aerostructural models was undertaken by Kenway et al. [51, 52], Kennedy et al. [53, 54], Marta et al. [55], Mader et al. [56]. By 2012 all of the various methods had been combined to tackle all three of the above listed challenges, but the methods were somewhat tailored to the aerostructural specific case. In 2013 [57] and 2018 [58] Hwang and Martins developed a generalization of the different techniques for computing analytic derivatives as well as a computational and algorithmic architecture to leverage them for general MDO frameworks which helped to extend the state of the art MDO methods to a more general class of problems. The only missing piece to be able to extend that work to aeropropulsive applications was the need to use RANS CFD aerodynamic models (instead of Euler), and that was first demonstrated in 2012 by Osusky by Zingg[59] and further developed extensively by Lyu et al. [60] in 2013.

Thanks to the developments in the CFD and MDO fields, by 2013 all of the methods needed to tackle design optimization of BLI propulsion systems were in place. With the various methods available it has been the primary goal of my research to adapt them to the new application on aeropropulsive models with high fidelity RANS CFD aerodynamic models. This thesis presents my work applying high-fidelity MDO to the challenge of designing BLI propulsion systems.

CHAPTER 2

Approach aeropropulsive design optimization of BLI systems

This chapter details the methods and tools used to build a coupled aeropropulsive model of a BLI propulsor. The construction of aeropropulsive models is made difficult from a confluence of separate but compounding factors. In order to capture the viscous flow effects that create the boundary layer on arbitrary 3-D bodies RANS CFD is needed for the aerodynamic analysis. One challenge with RANS CFD is that it is a computationally expensive modeling approach that requires a distributed memory parallel computing architecture to execute efficiently. Another, more significant challenge that arises when applying RANS CFD is the resulting large number of aerodynamic shape design variables that are needed in order to provide enough design freedom to achieve a high performing geometry. In order to properly parameterize a general 3-D geometry, you can easily have 10's to 100's of shape design variables. Although many of these shape design variables are not ones that, during the early stages of a design cycle, you would usually be concerned with the RANS CFD analysis is highly sensitive to them. As such, when integrating a RANS CFD analysis—or any CFD analysis for that matter—into an aeropropulsive model you end up with both a computationally expensive model and a large number of design variables who's values are not easily chosen by basic engineering principals.

As discussed in Section 1.4, the MDO community has developed a number of techniques to efficiently solve design problems of this nature, by leveraging gradient based optimization with analytic derivatives. Optimization is used here because the design problem is under-defined, by which I mean that there are more design variables than there are relationships to constrain them, and hence there is no unique solution to the problem. Instead we define an objective function and seek the combination of variables that maximizes or minimizes that objective as a means of creating a problem formulation with a single answer. There are many different algorithms for optimization, but they can be classified into two broad categories: gradient free and gradient based. Both classes of algorithms have

their strengths and weakness, but gradient based algorithms offer vastly superior computational efficiency. This is demonstrated clearly in Figure 2.1, which shows the relative cost of applying different optimization algorithms to a satellite design problem [61]. The primary conclusion here is that gradient based methods, even with finite difference derivatives, are an order of magnitude more efficient than gradient free methods. Applying adjoint analytic derivatives achieves nearly independent computational cost with respect to increasing number of design variables. This issue was investigated in great detail by Lyu et al. [62] in the context of aerodynamic shape optimization, showing that gradient based methods were two to four orders of magnitude more efficient than the gradient free methods.

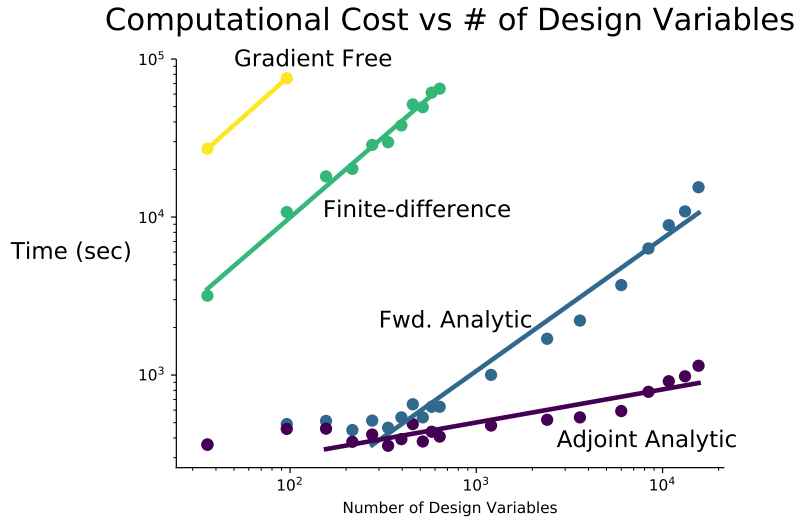


Figure 2.1: Scaling of the cost for computing derivatives vs the number of design variables for a representative design optimization of a satellite design problem.

The computational efficiency of the gradient based optimization with analytic derivatives motivated me to adopt this technique for my research, so that I could keep the cost of running an optimization as low as possible. Inexpensive optimizations enabled me to run many of them to perform design space exploration. Unfortunately leveraging efficient gradient based optimization is not without its challenges. The most significant difficulty is that, for different phases of the research I used different model setups, which would traditionally necessitate separate implementations for computing analytic derivatives. Re-implementing the analytic derivative computation for each model would require significant work, so a more flexible and modular approach was needed. Additionally, not all of the analysis tools used in this research provided analytic derivatives which meant that it would be necessary to implement a semi-analytic approach to computing total derivatives across the model.

In order to address all of these difficulties, I leveraged the OpenMDAO framework [61]

to build the various coupled models used in this thesis. The framework provides the ability to re-configure the model as needed to support different coupling strategies, and also has features that allow the computation of semi-analytic derivatives using a combination of finite-differencing for some analyses and analytic derivatives for others.

2.1 MDO architectures for aeropropulsive applications

The MDO community has proposed a wide range of different optimization architectures for optimizing coupled problems [63], but benchmarking efforts [64, 65] have shown that two architectures provide the most consistent performance and lowest computational cost: multidisciplinary design feasible (MDF) and individual design feasible (IDF).

The MDF architecture solves a multidisciplinary optimization problem in the manner shown by the XDSM diagram [1] in Figure 2.2. A nonlinear solver drives the model to physical compatibility for any given set of design variable values. From an optimization standpoint, using MDF means that the optimizer is always presented with a physically valid design as the output of the model for whatever design variable values it has chosen. As a result MDF tends to be highly robust. Another positive aspect of MDF is that, since the solver converges all the multidisciplinary compatibility constraints, the optimizer does not see them which means there are less linear solves needed to compute the total derivatives for the optimizer. Chapter 2.2 discussed how linear solves are used to compute total derivatives in more detail, but for now it is sufficient to simply understand that typically one linear solve is required per constraint value. Less constraints means less linear solves and lower computational cost for computing derivatives.

The downside to the MDF approach is that because you are converging the model with a solver, you also need to compute coupled multidisciplinary derivatives [48], which means that although there are fewer linear solves needed the ones you do have to perform are somewhat more computationally expensive. In smaller models, OpenMDAO can use a simple direct factorization to solve for the coupled derivatives. However, when high-fidelity tools such as RANS CFD models are being used a direct factorization is not possible. Martins was the first to successfully solve for coupled derivatives in this type of situation, using a linear block Gauss-Seidel solver [50] to compute derivatives for a high fidelity aerostructural optimization. Martins' approach was effective, but later Kenway et al. [66, 52, 67] developed a preconditioned Krylov based solver to compute the coupled derivatives more efficiently than the linear block Gauss-Seidel solver. While OpenMDAO is capable of solving for coupled derivatives, using the coupled Krylov solver architecture developed by Kenway et al. the computational cost of doing so is still significantly higher than solving

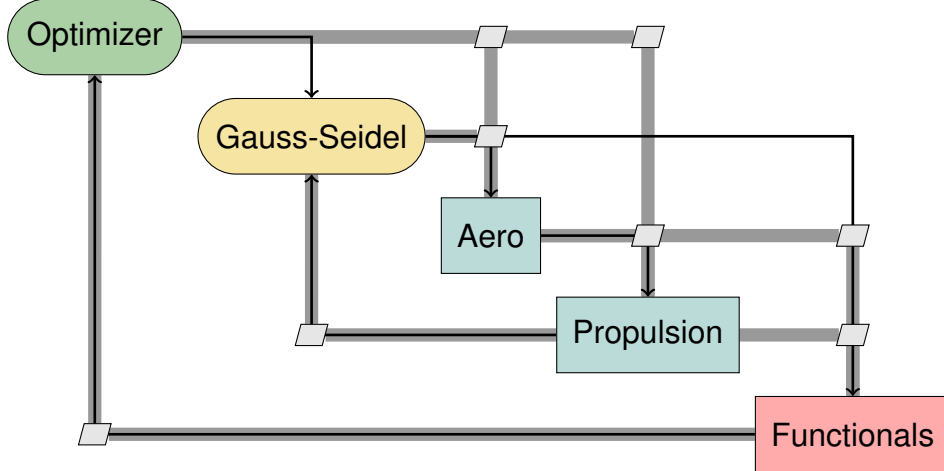


Figure 2.2: XDSM [1] diagram displaying a notional aeropropulsive optimization problem solved with the MDF optimization architecture.

for a single aerodynamic only adjoint. In the case of a coupled high-fidelity aerostructural model there are 10000's of individual coupling constraints that must be converged (one for each node in the aerodynamic surface mesh), and hence the cost of the coupled adjoint is well worth it to avoid solving so many separate adjoints. However, for aeropropulsive application in this research there are many fewer coupling variables; on the order of five to 10. Because of the smaller number of coupling variables, the IDF architecture provides a simpler but still computationally efficient method of building a coupled model.

The key characteristic of the IDF architecture is that it does not use a nonlinear solver to converge the multidisciplinary compatibility constraints. Instead, it promotes all of the multidisciplinary state variables up to be design variables for the optimizer and adds the associated equality constraints to the optimization problem as well. This is illustrated in the XDSM diagram in Figure 2.3, which shows how the optimizer directly converges the full MDO problem without the any nonlinear solver loop. This means that an optimization problem solved with IDF has more design variables and constraints than the same problem solved with MDF. The advantage gained by the increased problem size is that the task of computing the necessary derivatives is much simpler. As long as there are not too many compatibility constraints, then IDF offers a simpler path toward efficient MDO.

In the end, both MDF and IDF are solving the same optimization problem. Since the number of coupling variables for the aeropropulsive problems solved in this thesis was so small, IDF was the clear choice for optimization. Notably, however, in Chapter 4 I do use a nonlinear solver to perform aeropropulsive analysis (no optimization) with coupled models. That was necessary because there was no optimizer used for that study, hence it was not

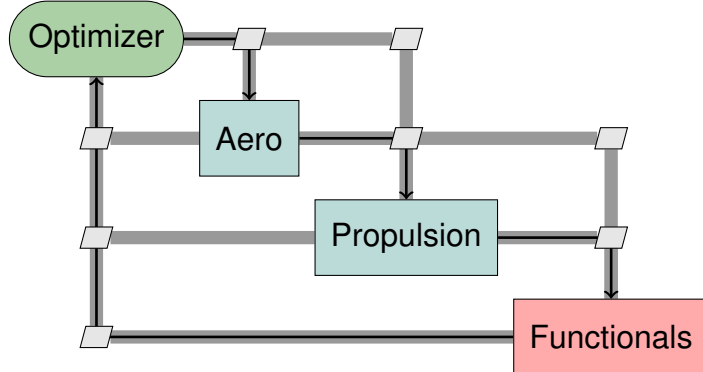


Figure 2.3: XDSM [1] diagram displaying a notional aeropropulsive optimization problem solved with the IDF optimization architecture.

able to converge the multidisciplinary coupling. OpenMDAO is capable of supporting both methods (with and without a nonlinear solver), and I exploited that flexibility to customize the solution architecture for each phase of the research.

2.2 Using the OpenMDAO to compute analytic derivatives for coupled models

As mentioned in Chapter 2.1, the two primary challenges for working with aeropropulsive models are the need for modular and flexible model construction and the difficulty that such modularity then poses in terms of computing analytic derivatives for the coupled model. Both of these difficulties are addressed by NASA’s OpenMDAO framework [61], which is specifically designed to support gradient based optimization with analytic derivatives for MDO applications. This section presents the theoretical underpinnings of OpenMDAO which enabled it to be useful in this research. Though the theory and development of OpenMDAO is not part of the contributions of this research, it is presented here for completeness and clarity.

The ability to construct multidisciplinary models in a modular fashion is certainly not unique to OpenMDAO. Many other frameworks also offer this functionality (e.g. ModelCenter, Isight, ModeFrontier). The modularity, while extremely valuable from a model construction standpoint, is also extremely problematic when it comes to the task of computing analytic derivatives. The challenge is that even if each individual discipline were to provide its own analytic derivatives, then the specific way that they are combined in any given model must be accounted for in the computation of derivatives across the entire model.

Traditionally, an MDO practitioner that wished to use gradient based optimization with analytic derivatives would be required to first implement the multi-disciplinary model in some ad-hoc fashion and then also implement the computation of derivatives across that model using the chain-rule. This means that any changes to the model itself will also need to be mirrored in the chain-rule derivative computation. Thus, somewhat paradoxically, if you use a framework to make it easy to rearrange a multidisciplinary model for different use cases then you are also creating a lot of additional work because the chain-rule must be re-applied each time a change is made.

OpenMDAO addresses this paradoxical problem by, in addition to supporting modular model construction, providing functionality that automatically applies a generalized form of the chain-rule to also compute the derivatives across that model. The automatic derivatives functionality of OpenMDAO makes it much easier to work with flexible multidisciplinary models in combination with gradient based optimization with analytic derivatives.

At this point, to further understand the challenge associated with computing analytic derivatives and how OpenMDAO alleviates it, we must introduce some more specific terminology:

- **total derivatives**: derivative of an objective or constraint with respect to a design variable (i.e. df/dx)
- **partial derivatives**: derivative of a disciplinary output with respect to its own inputs (i.e. $\partial f/\partial x$)

The distinction between total derivatives and partial derivatives is crucially important in the context of understanding how the analytic derivative functionality of OpenMDAO works. The framework can automatically compute **total derivatives**, assuming that it is given access to all of the **partial derivatives** of each discipline. There are four different ways that partial derivatives can be computed — finite-difference, complex-step, hand derivation, algorithmic derivation — and OpenMDAO supports all of them. Regardless of which methods is chosen, it is relatively computationally inexpensive to obtain the partial derivatives. The challenge then is to find a way to compute accurate total derivatives, given only the partial derivatives. For the remainder of this section, I will assume that the partial derivatives are simply known quantities and focus on how to compute the total derivatives.

Given an arbitrary function $f(x, y)$, where y is length m vector of variables that are implicitly dependent on a length n vector x then

$$\frac{df}{dx} = \frac{\partial f}{\partial x} + \frac{\partial f}{\partial y} \frac{dy}{dx}. \quad (2.1)$$

The only derivative in Eq. (2.1) that is not partial is dy/dx , which captures the change in the converged values for y with respect to x . Noting that y is defined implicitly by $\mathcal{R}(x, y) = 0$ and differentiating with respect to x yields

$$\frac{d\mathcal{R}}{dx} = \frac{\partial\mathcal{R}}{\partial x} + \frac{\partial\mathcal{R}}{\partial y} \frac{dy}{dx} = 0. \quad (2.2)$$

Re-arranging this equation, we get the linear system

$$\underbrace{\begin{bmatrix} \frac{\partial\mathcal{R}}{\partial y} \\ \vdots \\ \frac{\partial\mathcal{R}}{\partial y} \end{bmatrix}_{m \times m}}_{m \times m} \underbrace{\frac{dy}{dx}}_{m \times n} = \underbrace{\begin{bmatrix} \frac{\partial\mathcal{R}}{\partial x} \\ \vdots \\ \frac{\partial\mathcal{R}}{\partial x} \end{bmatrix}_{m \times n}}_{m \times n}. \quad (2.3)$$

Now dy/dx can be computed using by solving this linear system, which is constructed using only partial derivatives. This linear system needs to be solved n times, once for each component of x , with the right hand being the column of $[\partial\mathcal{R}/\partial x]$ that corresponds to that specific component of x . Then, dy/dx can be used in Eq. (2.1) to compute the total derivatives. This approach is known as the direct method.

There is another way to compute the total derivatives based on these equations. If we substitute the solution of the linear system (2.3) into the total derivative equation (2.1), we obtain:

$$\frac{df}{dx} = \frac{\partial f}{\partial x} + \underbrace{\frac{\partial f}{\partial y} \left[\underbrace{\begin{bmatrix} \frac{\partial\mathcal{R}}{\partial y} \\ \vdots \\ \frac{\partial\mathcal{R}}{\partial y} \end{bmatrix}_{m \times m}}_{\psi^T} \right]^{-1} \begin{bmatrix} \frac{\partial\mathcal{R}}{\partial x} \\ \vdots \\ \frac{\partial\mathcal{R}}{\partial x} \end{bmatrix}}_{1 \times m}. \quad (2.4)$$

By grouping the terms $[\partial f/\partial y]$ and $[\partial\mathcal{R}/\partial y]$ we get a $(1 \times m)$ row vector. This vector, denoted with ψ is called the adjoint vector. If we can compute ψ , using only partial derivatives then we could get df/dx via

$$\frac{df}{dx} = \frac{\partial f}{\partial x} + \psi^T \frac{\partial\mathcal{R}}{\partial x}, \quad (2.5)$$

which is referred to as the adjoint method.

To compute ψ^T , we perform the following manipulation:

$$\begin{aligned}
\psi^T &= \frac{\partial f}{\partial y} \left[\frac{\partial \mathcal{R}}{\partial y} \right]^{-1} \\
\psi &= \left[\frac{\partial f}{\partial y} \left[\frac{\partial \mathcal{R}}{\partial y} \right]^{-1} \right]^T \\
\psi &= \left[\frac{\partial \mathcal{R}^T}{\partial y} \right]^{-1} \frac{\partial f^T}{\partial y} \\
\left[\frac{\partial \mathcal{R}^T}{\partial y} \right] \psi &= \frac{\partial \mathcal{R}^T}{\partial y} \left[\frac{\partial \mathcal{R}^T}{\partial y} \right]^{-1} \frac{\partial f^T}{\partial y} \\
\underbrace{\left[\frac{\partial \mathcal{R}^T}{\partial y} \right]^T}_{m \times m} \underbrace{\psi}_{m \times 1} &= \underbrace{\left[\frac{\partial f}{\partial y} \right]^T}_{m \times 1}.
\end{aligned} \tag{2.6}$$

The linear system in Equation (2.6) needs to be solved once for each function of interest (f). If f is a vector, then the right hand side for each solve is the corresponding row of the partial derivatives matrix $[\partial f / \partial y]$. This derivation shows why the computational cost of this method is proportional to the number of outputs and independent of the number of inputs. Therefore, if the number of inputs exceed the number of outputs, the adjoint method is advantageous, while if the opposite is true, then the direct method has the advantage.

As mentioned in Chapter 1.4, the analytic methods—Equations (2.1), (2.3), (2.5), (2.6)—have been extended to MDO applications [48] and further adapted for high-fidelity applications [50]. The challenge, as stated earlier, is that applying these methods in practice requires the ad-hoc combination of the chain rule along with the direct or adjoint formulations above in order to compute total derivatives for each specific model.

To overcome the challenge of model specific derivative computations Hwang and Martins[68, 69] developed the modular analysis and unified derivatives (MAUD) architecture, which provides the mathematical and algorithmic framework to combine the chain rule, direct, and adjoint methods into a single generalized implementation that could be integrated into a modular framework environment. The key theoretical innovation they developed is the unified derivatives equation (UDE), which combined all of the different methods of computing analytic derivatives a single linear system of equations, that when solved, would provide the total derivatives for any model without the need for ad-hoc derivations.

To accomplish this, they introduced a subtle transformation of all equations in the model into an implicit form,

$$\mathcal{R}(o) = r = 0, \quad (2.7)$$

where all variables in the model become implicit state variables and the whole model takes the form of a single combined nonlinear system. $\mathcal{R}()$ is the nonlinear residual function for the whole model, o is the vector of variables in the model (every output of every disciplinary analysis), and r is the actual value of the residual function which must be driven to 0 for a valid solution. Given Equation (2.7), they then showed that total derivatives could be computed via the UDE:

$$\left[\frac{\partial \mathcal{R}}{\partial o} \right] \left[\frac{do}{dr} \right] = \mathcal{I} = \left[\frac{\partial \mathcal{R}}{\partial o} \right]^T \left[\frac{do}{dr} \right]^T. \quad (2.8)$$

The matrix $\partial \mathcal{R} / \partial o$ contains all the partial derivatives from each disciplinary analysis, which we have assumed to be known quantities here. The matrix do / dr contains the total derivatives that we ultimately want (i.e., df / dx). The left hand side of Equation (2.8) is analogous to the direct method from Equation (2.3), and must be solved once per design variable. The right hand side of Equation (2.8) is analogous to the adjoint method, Equation (2.6), and must be solved once per objective and constraint variable.

OpenMDAO solves for total derivatives using Equation (2.8) by automatically assembling $[\partial \mathcal{R} / \partial o]$ and then solving the linear system the appropriate number of times to compute all the total derivatives needed for optimization.

2.2.1 A simple representative example

A simple representative example is presented to help clarify the implicit transformation required in Equation (2.7) and to make more obvious how do / dr from Equation (2.8) includes the actual derivatives needed for optimization (e.g. df / dx).

I begin with a pair of very simple discipline analyses represented by one equation each:

$$(\text{Discipline 1}) \quad y_1 = y_2^2 \quad (2.9)$$

$$(\text{Discipline 2}) \quad \exp(-y_1 y_2) - xy_2 = 0, \quad (2.10)$$

$$(\text{Objective}) \quad f = y_1^2 + y_2 + 3. \quad (2.11)$$

Discipline 1 and the objective function (Equations (2.9) and (2.11)) are explicit functions, and Discipline 2 (Equation (2.9)) is an implicit function. The associated OpenMDAO model would be composed as shown in Figure 2.4, with the red boxes representing explicit functions and the blue box representing the implicit function. Notably, although Discipline

1 itself is an explicit function, there is an implicit coupling between Disciplines 1 and 2, which means that collectively those two disciplines represent an implicit system in this model.

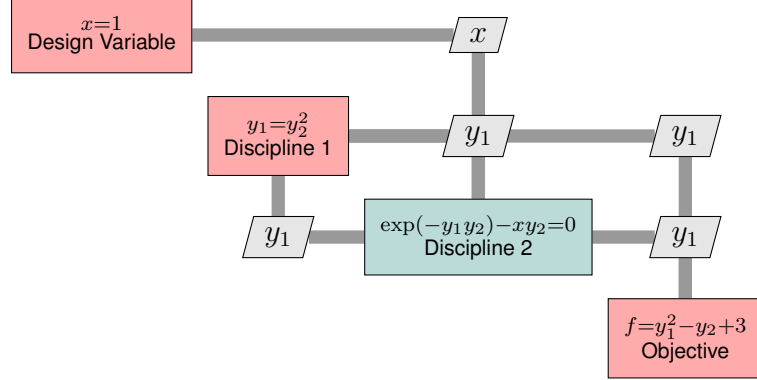


Figure 2.4: XDSM [1] diagram showing how a simple example model would be constructed in OpenMDAO.

Although an OpenMDAO user does not need to manually perform the MAUD implicit conversion form Equation (2.7), the transformation is performed none the less behind the scenes by the framework. For this problem the implicit transformation would be done as follows:

$$\begin{aligned}
 x &= x^* \\
 y_1 &= y_2^2 \\
 \exp(-y_1 y_2) - xy_2 &= 0 \\
 f &= y_1^2 - y_2 + 3
 \end{aligned} \Rightarrow \mathcal{R}(o) = \begin{bmatrix} x - x^* \\ y_1 - y_2^2 \\ \exp(-y_1 y_2) - xy_2 \\ f - y_1^2 + y_2 + 3 \end{bmatrix} = \begin{bmatrix} r_x \\ r_{y_1} \\ r_{y_2} \\ r_f \end{bmatrix} = 0. \quad (2.12)$$

Now the partial derivatives of $\mathcal{R}(o)$ can be computed as

$$\frac{\partial \mathcal{R}_x}{\partial x} = \frac{\partial x}{\partial x} = 1 \quad (2.13)$$

$$\frac{\partial \mathcal{R}_{y_1}}{\partial y_1} = \frac{\partial y_1}{\partial y_2} = 1 \quad (2.14)$$

$$\frac{\partial \mathcal{R}_{y_1}}{\partial y_2} = -\frac{\partial y_1}{\partial y_2} = -2y_2 \quad (2.15)$$

$$\frac{\partial \mathcal{R}_{y_2}}{\partial y_1} = -y_2 \exp(-y_1 y_2), \quad (2.16)$$

$$\frac{\partial \mathcal{R}_{y_2}}{\partial y_2} = -y_1 \exp(-y_1 y_2) - x, \quad (2.17)$$

$$\frac{\partial \mathcal{R}_{y_2}}{\partial x} = -y_2 \quad (2.18)$$

$$\frac{\partial \mathcal{R}_f}{\partial y_1} = -\frac{\partial f}{\partial y_1} = -2y_1 \quad (2.19)$$

$$\frac{\partial \mathcal{R}_f}{\partial y_2} = -\frac{\partial f}{\partial y_2} = -1 \quad (2.20)$$

$$\frac{\partial \mathcal{R}_f}{\partial f} = \frac{\partial f}{\partial f} = 1. \quad (2.21)$$

$$(2.22)$$

In Equations (2.13)-(2.21) I have noted the equality between the partial derivatives of the implicitly transformed equations and the original explicit forms (they differ only by a negative sign). These partial derivatives can then be assembled into $[\partial \mathcal{R}/\partial o]$ and then Equation (2.8) can be used to solve for $[do/dr]$, which contains the actual derivatives needed as shown in Equation (2.23).

$$\left[\frac{do}{dr} \right] = \begin{bmatrix} \frac{dx}{dr_x} & \frac{dx}{dr_{y_1}} & \frac{dx}{dr_{y_2}} & \frac{dx}{dr_f} \\ \frac{dy_1}{dr_x} & \frac{dy_1}{dr_{y_1}} & \frac{dy_1}{dr_{y_2}} & \frac{dy_1}{dr_f} \\ \frac{dy_2}{dr_x} & \frac{dy_2}{dr_{y_1}} & \frac{dy_2}{dr_{y_2}} & \frac{dy_2}{dr_f} \\ \frac{df}{dr_x} & \frac{df}{dr_{y_1}} & \frac{df}{dr_{y_2}} & \frac{df}{dr_f} \end{bmatrix} = \begin{bmatrix} 1 & 0 & 0 & 0 \\ \frac{dy_1}{dx} & \frac{dy_1}{dr_{y_1}} & \frac{dy_1}{dr_{y_2}} & 0 \\ \frac{dy_2}{dx} & \frac{dy_2}{dr_{y_1}} & \frac{dy_2}{dr_{y_2}} & 0 \\ \frac{df}{dx} & \frac{df}{dr_{y_1}} & \frac{df}{dr_{y_2}} & 1 \end{bmatrix}. \quad (2.23)$$

While in Equation (2.23) I have shown the full do/dr matrix, in practice it is never necessary to compute the entire thing. If a notional OpenMDAO model has an o vector of length 100 but only a single objective function, then assembling the entire total derivative matrix would require 100 solves, which is not necessary since we needed only a row of it. OpenMDAO solves only for whatever rows (forward/direct method) or columns (reverse/adjoint method) contain the quantities needed by the optimizer.

2.3 Overview of OpenMDAO model structure

OpenMDAO uses four main classes to construct and interact with models:

- **Component:** Maps input variables to output variables
- **Group:** Hierarchical container of Components and other groups
- **Driver:** Iterative model execution control (e.g. optimizer, design of experiments)
- **Problem:** Container for other objects that provides model execution interface

The relationship between the classes is illustrated graphically in Figure 2.5. Of these four classes, the most important two to understand are the **Component** and **Group**, because these are the fundamental building blocks used to construct the actual multidisciplinary model itself. A single disciplinary analysis can be composed of a single component or it could be a group composed of many sub-components. In this thesis, both situations occur, so when I refer to a “disciplinary analysis” it may be in reference to either a group or a component.

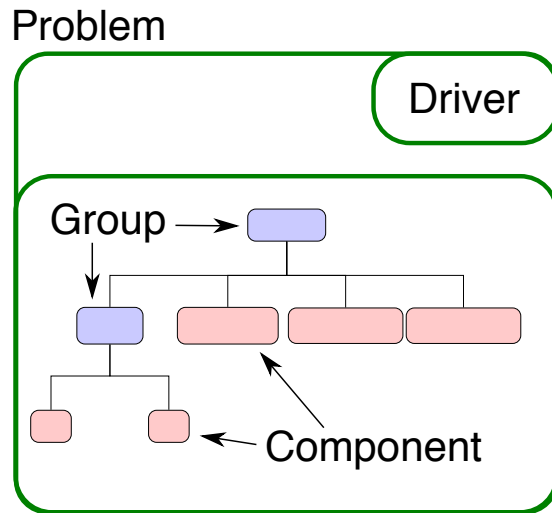


Figure 2.5: Diagram of a notional OpenMDAO model, including the four major classes.

In Chapter 2.2, the concepts of **partial derivatives** and **total derivatives** were introduced. In the broad sense, I defined partial derivatives as the derivatives of disciplinary outputs with respect to disciplinary inputs. In the practical implementation of an OpenMDAO model, partial derivatives refer specifically to derivatives of component outputs with respect to component inputs. So if a given disciplinary analysis is built from a group containing sub-components, then each sub-component provides its own partials. Groups do

not directly provide their own partial derivatives, rather they expose the partial derivatives of their sub-components.

Total derivatives, in the context of an OpenMDAO model, refer to the derivatives of model outputs (i.e. objective and constraints) with respect to model inputs (i.e. design variables). As explained in Chapter 2.2, total derivatives are computed via the solution to a linear system defined by Equation (2.8). OpenMDAO provides an interface, via the **Problem** class, for the user to request total derivatives. When called, this function will solve Equation (2.8) using customized linear solvers in either the forward or reverse modes, and then return the total derivatives.

CHAPTER 3

pyCycle: propulsion analysis for multidisciplinary applications

An aeropropulsive model is composed of two primary disciplinary analyses — aerodynamics and propulsion — along with a set of secondary (and less expensive) components. The primary analyses are the most expensive parts of the computation, and hence it is important that both provide analytic derivatives to ensure an efficient optimization.

The aerodynamic analysis in this research was performed using ADflow, an efficient RANS CFD solver with an algorithmically differentiated adjoint [70, 56]. This solver has been extremely well developed and used extensively in many different aerodynamic and aerostructural design applications [67, 71, 72, 73, 74] that have proven both the efficiency and accuracy of both its nonlinear analysis and its adjoint solver.

For the propulsion analysis, no suitable propulsion modeling tool was available that provided both the necessary accuracy and analytic derivatives. The state of the art propulsion modeling tool, in wide use by both government and industry, is Numerical Propulsion System Simulation (NPSS). This code poses 1-D propulsion models as large nonlinear system of equations and converges it using a Newton solver. NPSS predicts engine performance (e.g. thrust, fuel burn) for arbitrary operating conditions, accounting for key engine design considerations such as shaft speed and temperature limitations and turbine cooling requirements [29, 30]. While NPSS is an extremely powerful propulsion modeling tool, it doesn't provide analytic derivatives. A number of researchers have specifically noted issues with finite-differencing NPSS in optimization applications[75, 76, 77, 78, 79], which further underscores the need for analytic derivatives in the propulsion model.

Since no existing propulsion analysis tool provided analytic derivatives I chose to develop a new one that could, while still providing the same modular modeling functionality of NPSS. To achieve this, I levered the capabilities of OpenMDAO to support modular model construction with analytic derivatives, and developed pyCycle as a library of components and groups that can perform the necessary functions for propulsion modeling.

3.1 Predicting gas thermodynamic properties via chemical equilibrium analysis

Before a full cycle modeling capability could be developed, I first developed the core thermodynamic prediction library. This library provided the means to predict the relevant thermodynamic properties of air (e.g. enthalpy, entropy, density, specific heat ratio, etc.) as a function of temperature and pressure. All of the propulsion element engineering calculations (e.g. inlet, compressor, combustor, turbine, etc.) assume the availability of these calculations, so its development was the crucial first step.

A number of different methods exist for computing the thermodynamic properties of air and air-fuel mixtures, and many implementations of these methods are available. NPSS provides a set of thermodynamics libraries (CEA, JANAF, ALLFUEL, GasTbl), which the user can select at runtime [29]. ALLFUEL and GasTbl are computationally efficient but are based on interpolated tabular data and are only accurate for Jet-A fuels or other fuels that are chemically very similar to Jet-A fuel. Tran and Snyder [80] demonstrated that tabular thermodynamics data offer limited accuracy when considering fuels that are chemically dissimilar from those used to generate the data. They recommend either generating new tabular data when switching fuels or integrating a chemical-equilibrium analysis directly into the propulsion code. For unconventional cycle configurations that use multiple fuels (for example, combining Jet-A fuel with liquid natural gas [81]), tabular thermodynamics data are not suitable.

A more advanced technique for building a Kriging surrogate model of the equilibrium gas composition was proposed by Walter and Owen [82] and offers a more flexible option for an interpolation-based method. However, this technique does not provide a means of computing the thermodynamic properties of the composite gas. The CEA and JANAF libraries use a chemical-equilibrium-based method, but the JANAF library only considers a fixed set of species. The CEA [83] library is by far the most general of the options in NPSS, accepting an arbitrary number of chemical species that enables it to consider a wide range of fuels.

There are also a number of chemical-equilibrium libraries developed for fields outside of cycle analysis. MINEQL+ [84] specializes in equilibrium reactions in aqueous solutions. ChemSage [85] supports reactions that include metallic elements and metal oxides. JANAF, CEA, MINEQL+, and ChemSage all solve for chemical equilibrium directly by minimizing the Gibbs energy. These codes differ primarily in the details of how they converge the nonlinear chemical-equilibrium equations and also offer specialized features for their specific applications. Another alternative is the nonstoichiometric equilibrium method [86],

which is used by the open-source library Cantera [87]. Chin et al. [88] used the Cantera implementation for an application involving cycle analysis.

For each propulsion analysis, the thermodynamics module is called hundreds of times, so computational efficiency is important. However, flexibility to consider a wide range of fuels is also important to allow alternative fuels to be investigated, such as hydrogen [89], natural gas [81, 90], and bio-fuels. The low flexibility of interpolative methods makes them less desirable, despite their simplicity. Chemical-equilibrium methods provide the needed flexibility. The Cantera library was ruled out due to our prior experience using it in this application where it led to problems regarding performance. I considered the option of differentiating one of the other chemical-equilibrium libraries, but none implement a continuous solution algorithm that is differentiable. The CEA and JANAF libraries use a method for handling trace species—those with negligible concentrations—where a heuristic controls their addition and removal from the equilibrium calculations, causing small discontinuities in the solution. These discontinuities are problematic from an analysis point of view [91] and create points where derivatives are not defined. Therefore, I developed a new algorithm for solving the chemical-equilibrium analysis that is differentiable and thus suitable for gradient-based optimization.

3.1.1 Chemical Equilibrium Equations

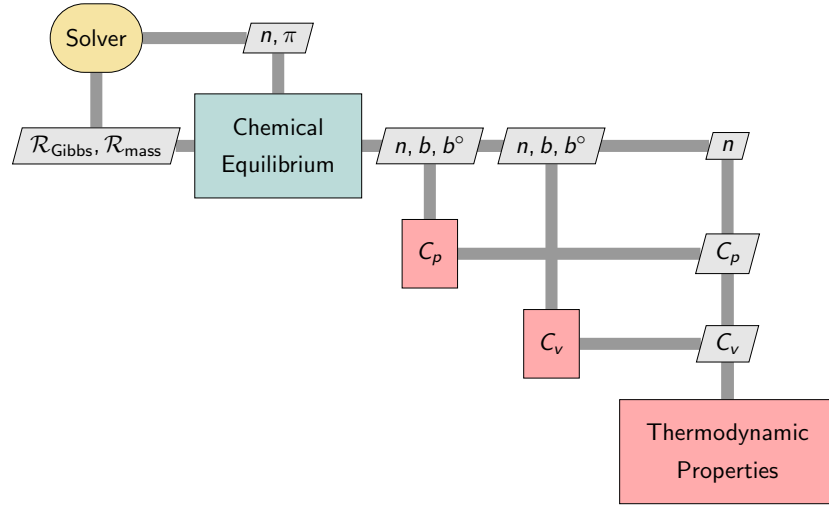


Figure 3.1: XDSM diagram of the chemical equilibrium analysis sequence.

3.1.1.1 Thermodynamic Properties Prediction

To find the thermodynamic state of a gas, CEA uses the multistep process illustrated in Figure 3.1 as an extended design structure matrix (XDSM) diagram [1]. First, it solves a system of nonlinear equations to minimize the Gibbs energy, which gives the equilibrium composition for the gas (n) at the prescribed state and lagrange multipliers to satisfy a mass conservation constraint (π). Second, it solves an additional set of equations to compute the thermodynamic state of the gas by using the converged equilibrium composition. These equations are documented in detail by Gordon and McBride [83] in their seminal paper on CEA. However, the form of the equations presented in their work combines the residuals from the Gibbs-energy minimization with a customized procedure for solving for the Newton update. This combination was motivated by the computing power limitations imposed by early computing hardware. However, with modern computers and more powerful linear algebra libraries, it is much better to keep the residuals separate from the numerics to simplify the task of differentiating the analysis. The purely physical form of the equations is presented here. We refer the reader to the original CEA publication for details on the second step where the thermodynamic properties are computed from the converged equilibrium solution; it remains unchanged from the original formulation [83].

3.1.1.2 Gibbs Energy Minimization

The full thermodynamic state of a real gas can be defined by any two of the five physical state variables: temperature T , pressure P , density ρ , entropy S , and enthalpy h . Three specific combinations are useful for propulsion analysis: temperature and pressure (Tp), enthalpy and pressure (hP), and entropy and pressure (Sp). The Tp formulation is the most fundamental. The hP and Sp formulations augment the Tp -formulation equations with a new state variable T and the associated residual to drive the solution to the prescribed value of h or S .

Temperature-Pressure Formulation

The Gibbs energy g is defined as

$$g = \sum_j^{N_s} (\mu_j n_j), \quad (3.1)$$

where N_s is the number of chemical species, and n_j and μ_j are the concentration (kg-mol/kg-mixture) and the chemical potential of the j^{th} species, respectively. The chemical

potential is a function of temperature, pressure, and concentration and is given by

$$\frac{\mu_j}{RT} = \frac{H_j^\circ(T)}{RT} - \frac{S_j^\circ(T)}{RT} + \ln\left(\frac{p}{p_a}\right) + \ln(n_j) - \ln\left(\sum_k^{N_s} n_k\right), \quad (3.2)$$

where R is the universal gas constant, and H° and S_j° are given by

$$\frac{H_j^\circ(T)}{RT} = \frac{-c_0}{T^2} + \frac{c_1 \ln(T)}{T} + c_2 + \frac{c_3}{2}T + \frac{c_4}{3}T^2 + \frac{c_5}{4}T^3 + \frac{c_6}{5}T^4 + \frac{c_7}{T}, \quad (3.3)$$

$$\frac{S_j^\circ(T)}{R} = \frac{-c_0}{2T^2} - \frac{c_1}{T} + c_2 \ln(T) + c_3 T + \frac{c_4}{2}T^2 + \frac{c_5}{3}T^3 + \frac{c_6}{4}T^4 + c_8, \quad (3.4)$$

where c_0, \dots, c_8 are constants for each species, taken from the NIST-JANAF Thermochemical Tables [92].

The equilibrium composition is defined by the values of the concentration variables n that minimize the Gibbs energy subject to conservation-of-mass constraints. The mass is tracked on an elemental basis and is given by

$$\mathcal{R}_{\text{mass } i} = \sum_{j=1}^{N_s} (a_{ij} n_j) - b_i^\circ = 0 \quad (3.5)$$

where N_s is the number of species in the mixture, b_i° is the amount of each element in the initial composition, and a_{ij} is the stoichiometric constant for element i of species j . The mass-balance residuals $\mathcal{R}_{\text{mass } i}$ yield N_e constraints—one per element present in the mixture. To solve the mass-constrained minimization of the Gibbs energy, we form a Lagrangian

$$G = \sum_{j=1}^{N_s} (\mu_j n_j) + \sum_{i=1}^{N_e} \lambda_i \left(\sum_{j=1}^{N_s} (a_{ij} n_j) - b_i^\circ \right), \quad (3.6)$$

where λ_i is the Lagrange multiplier for the i^{th} element. We differentiate with respect to the n and λ variables to build a system of nonlinear equations whose solution minimizes the Lagrangian:

$$\delta G = \sum_{j=1}^{N_s} \left(\mu_j + \sum_{i=1}^{N_e} (\lambda_i a_{ij}) \right) \delta n_j + \sum_{i=1}^{N_e} \left(\sum_{j=1}^{N_s} (a_{ij} n_j) - b_i^\circ \right) \delta \lambda_i = 0. \quad (3.7)$$

Because δG is linear in δn_j and $\delta \lambda_i$, we can split Equation (3.7) into two sets of equations.

We get N_s equations,

$$\mathcal{R}_{\text{Gibbs}} = \mu_j + \sum_{i=1}^{N_e} (\lambda_i a_{ij}) = 0, \quad (3.8)$$

as residuals representing the Gibbs energy. For convenience, because of the factors of $1/RT$ in Equations (3.2) and (3.4), we define an alternative Lagrange multiplier as follows:

$$\pi_i = -\frac{\lambda_i}{RT}. \quad (3.9)$$

This yields an alternate form of Equation (3.8):

$$\mathcal{R}_{\text{Gibbs}} = \frac{\mu_j}{RT} - \sum_{i=1}^{N_e} (\pi_i a_{ij}) = 0. \quad (3.10)$$

Equations (3.5) and (3.10) yield a system with $N_s + N_e$ unknowns and $N_s + N_e$ residual equations, which can then be solved numerically.

Enthalpy-Pressure Formulation

The hP formulation retains the state variables (n and π) from the Tp solver and the associated residuals from Equations (3.5) and (3.10). In addition, it adds a new state variable T and a new residual to drive the computed enthalpy to match the specified enthalpy value h_0 :

$$\mathcal{R}_h = h_0 - \sum_{j=1}^{N_s} (n_j H_j^\circ(T)) = 0. \quad (3.11)$$

Entropy-Pressure Formulation

Like the hP problem, the Sp formulation uses the same setup as the Tp problem with one additional state variable and residual. In this case, the new state variable is the prescribed entropy, S_0 . The new residual drives the computed entropy to match the prescribed entropy:

$$\mathcal{R}_S = S_0 - R \sum_{j=1}^{N_s} \left\{ n_j \left(\frac{S_j^\circ(T)}{R} - \ln \left(\frac{p}{p_a} \right) - \ln(n_j) + \ln \left(\sum_k^{N_s} n_k \right) \right) \right\} = 0, \quad (3.12)$$

where the pressure term is nondimensionalized by standard atmospheric pressure ($P_a = 1.01325$ Bar). The reference condition is necessary because entropy is defined as a variation from a reference condition.

3.1.1.3 CEA Modified Newton's Method for Chemical Equilibrium

Newton Convergence Scheme

Gordon and McBride [83] applied Newton's method to converge the chemical-equilibrium system. When applied to Gibbs-energy minimization, Newton's method consists of successive solutions of the linear system

$$\frac{\partial \mathcal{R}}{\partial U} \Delta U = -\mathcal{R}(U), \quad (3.13)$$

where $U = [n, \pi]$ for a Tp problem, and $U = [n, \pi, T]$ for hp and Sp problems. ΔU is iteratively computed and applied until the residuals (3.5), (3.10)–(3.12) converge to zero within a chosen tolerance.

Note that Equation (3.10) involves computing μ_j , which, through Equation (3.2), requires taking the natural logarithm of n . In addition, Equation (3.4) involves taking the natural logarithm of T . Thus, neither n nor T can be negative during the iterations. The natural logarithms also cause numerical difficulties, because the derivative with respect to n tends to infinity as n tends to zero. In addition, this means that the Newton system becomes ill conditioned as n tends toward zero. In CEA this problem is partially dealt with via a logarithmic transformation, where ΔU is split into two parts: one for $[n, T]$ and another for π . The $[n, T]$ component of the updates are treated as $\Delta \ln(n)/n$ and $\Delta \ln(T)/T$. The Newton update equation is modified to account for this as follows:

$$n_{k+1} = n_k \exp\left(\frac{\Delta \ln(n)}{n}\right), \quad (3.14)$$

$$T_{k+1} = T_k \exp\left(\frac{\Delta \ln(T)}{T}\right). \quad (3.15)$$

By using the exponential update form, negative values from the Newton solution are converted into multiplicative updates that are always positive, so, assuming a positive initial guess, the values of n and T never become negative. The π update variables are treated normally, with a Newton update

$$\pi_{k+1} = \pi_k + \Delta\pi. \quad (3.16)$$

Although the CEA method deals with the need to keep both n and T positive, it does not solve the problem whereby trace species create poorly conditioned Jacobians. For this problem, species with n lower than a set value (10^{-5} by default) are discarded from the solution. Removal of species, even trace species, introduces a nondifferentiable discontinuity in the Jacobian matrix.

nuity that needs to be avoided. Leal et al. [91] propose a method that retains all species and modifies the computed Newton step for trace species to keep them positive. Because this method retains all species, it is continuous and thus differentiable. I adopt a similar approach to Leal for this work and use a step-limiting method from the built-in solvers in OpenMDAO to keep values positive at all times.

Computing $\partial\mathcal{R}/\partial U$

We compute $\partial\mathcal{R}/\partial U$ analytically, where the nonzero elements for the Tp residual partial derivatives are given by

$$\frac{\partial\mathcal{R}_{\text{Gibbs j}}}{\partial n_k} = \begin{cases} \frac{-1}{\sum_l^{N_s} n_l} & \text{if } j \neq k \\ \frac{1}{n_k} - \frac{-1}{\sum_l^{N_s} n_l} & \text{if } j = k, \end{cases} \quad (3.17)$$

$$\frac{\partial\mathcal{R}_{\text{Gibbs j}}}{\partial \pi_i} = -a_{ij}, \quad (3.18)$$

$$\frac{\partial\mathcal{R}_{\text{mass i}}}{\partial n_j} = a_{ij}. \quad (3.19)$$

When solving an hP or Sp problem, additional nonzero partial derivatives of Equation (3.8) with respect to T are given by

$$\frac{\partial\mathcal{R}_{\text{Gibbs j}}}{\partial T} = \frac{\partial H_j^\circ}{\partial T} - \frac{\partial S_j^\circ}{\partial T}. \quad (3.20)$$

For an hP problem, the residual (3.11) contributes the following nonzero partial derivatives:

$$\frac{\partial\mathcal{R}_h}{\partial n_j} = -RT H_j^\circ, \quad (3.21)$$

$$\frac{\partial\mathcal{R}_h}{\partial T} = -RT \sum_{j=1}^{N_s} n_j \left(\frac{\partial H_j^\circ}{\partial T} + H_j^\circ \right). \quad (3.22)$$

Similarly, for an Sp problem the residual (3.12) contributes the following nonzero partial derivatives:

$$\frac{\partial\mathcal{R}_S}{\partial n_j} = -R \left[\frac{S_j^\circ(T)}{R} - \ln\left(\frac{p}{p_a}\right) - \ln(n_j) + \ln\left(\sum_k^{N_s} n_k\right) - 1 \right], \quad (3.23)$$

$$\frac{\partial\mathcal{R}_S}{\partial T} = -R \sum_{j=1}^{N_s} \left(n_j \frac{\partial H_j^\circ}{\partial T} \right). \quad (3.24)$$

All these nonzero terms can be assembled into a matrix, which is then inverted using a direct factorization because the size of the matrix is at most $(N_s + N_e + 1)(N_s + N_e + 1)$, where the largest term N_s is on the order of hundreds of species.

3.1.2 Analytic Derivatives

In order to compute analytic derivatives across the chemical equilibrium solve, additional partial derivatives are needed beyond those required for applying Newton's method. For the Newton solver, we compute only the partial derivatives of the residual equations with respect to the state variables. To compute the analytic derivatives, still use the partial derivatives for Newton's method ($\partial \mathcal{R} / \partial U$) but now also include partial derivatives with respect to all the other variables as well. This yields a larger partial derivative matrix, ($\partial \mathcal{R} / \partial o$), which can then be used with Equation (2.8) in Chapter 2.2 to compute the total derivatives.

As an example, consider Equation (3.12). The two partial derivatives needed for the Newton solver are given by Equations (3.23) and (3.24). These two derivatives are augmented with the two following additional derivatives:

$$\frac{\partial \mathcal{R}_s}{\partial S_0} = 1, \quad (3.25)$$

$$\frac{\partial \mathcal{R}_s}{\partial p} = \frac{R}{p} \sum_{j=1}^{N_s} n_j. \quad (3.26)$$

For the chemical-equilibrium model developed herein, the structure of $[\partial \mathcal{R} / \partial o]^T$ is shown in Figure 3.2 for a *Tp* solver and in Figure 3.3 for the *hP* or *Sp* solver. The diagonal terms are the partial derivatives of the residuals with respect to the associated state variable or an output with respect to itself. The off-diagonal terms are partial derivatives of residuals or outputs with respect to the other variables. In Figure 3.2, the 2×2 block of partial derivatives, outlined in dark gray, are the same derivatives needed for the Newton solver. These partial derivatives are given by Equations (3.17)–(3.19). For the *Tp* solver, temperature is an input to the calculation, but, for the *hP* and *Sp* solvers, it becomes a state variable. For these slightly more complex solvers, the $\partial \mathcal{R} / \partial o$ matrix includes *h* or *S* as inputs and *T* as an additional state variable. The 3×3 block, outlined in dark gray in Figure 3.3, contains the Newton derivatives for the corresponding solvers. All other shaded boxes outside the Newton blocks are the additional partial derivatives needed to compute the multidisciplinary derivatives. It is convenient that the partial derivatives necessary for a Newton solver can be reused when computing derivatives for optimization, but Figures 3.2 and 3.3 also show that significantly more partial derivatives are required in the latter case.

	Inputs			Chem. Eq.			C_p	C_v	Thermo. Props.			
	T	p	n_{init}	b°	n	π	C_p	C_v	ρ	S	h	γ
Temperature	T											
Pressure		p										
Initial Composition Vector			n_{init}									
Init. element amounts				b°								
Composition vector					n							
Lagrange multipliers						π						
Specific heat at constant p							C_p					
Specific heat at constant volume								C_v				
Density									ρ			
Entropy										S		
Enthalpy											h	
Specific heat ratio												γ

Figure 3.2: Structure of partial derivative matrix for adjoint multidisciplinary derivatives of Tp solver. The subset of partial derivatives needed for the Newton solver is highlighted by the gray box

3.1.3 Verification of Analysis and Derivatives

The thermodynamics module is to be the foundation for a new cycle analysis tool, so it is important that it accurately models the thermodynamic properties of air and air-fuel mixtures across a wide range of temperatures and pressures. Given the goal of using this work for optimization, it is also important that the analytic derivatives be correct. This section presents the verification of the analysis and the corresponding derivatives.

3.1.3.1 Approach to Analysis Verification

The new code was verified against CEA predictions. The verification cases correspond to the temperature and pressure combinations listed in Table 3.1. A total of 3600 different conditions were examined with temperatures ranging from 200 to 4800 degrees Rankine, and pressures from 1 to 1500 psi. This regular grid was run at four equivalence ratios ϕ of 0, 0.015, 0.3, and 0.44 to provide a wide range of combustion conditions. The equivalence ratio (the ratio of the actual fuel-to-air ratio to the stoichiometric value) is a convenient way to express the amount of potential combustion in a manner that is independent of the specific fuel being used. This verification grid includes low temperatures that are not phys-



Figure 3.3: Structure of partial derivative matrix for adjoint multidisciplinary derivatives of hP and Sp solvers. The subset of partial derivatives needed for the Newton solver are highlighted by the gray box.

ically meaningful and that actually extend below the valid range of the thermodynamics data provided as input. Such low temperatures were run not to test the physical predictive power of the code under invalid conditions, but rather to compare it numerically with CEA under extreme conditions. Because the new code is to be used for optimization, it must be numerically stable even under nonphysical conditions because optimizations often iterate through physically invalid areas on their way to the optimum.

Table 3.1: Temperature and pressure conditions used for verification cases.

	Low	High	Step
Temperature (° R)	200	4800	200
Pressure (psi)	1	1500	10

To compute the verification data, the new code was set up with air at the temperature and pressure conditions prescribed in Table 3.1 and then combusted at the given ϕ with Jet-A, which is a hydrocarbon fuel ($C_{12}H_{23}$) with a stoichiometric fuel-air ratio of 0.06817 corresponding to $\phi = 1$.

The combustion was modeled as a prescribed enthalpy process by computing the overall enthalpy of the air-fuel combination and holding it constant while solving for a chemical-

equilibrium composition. Because the total enthalpy calculation is already required for the combustion model in the new code, the corresponding CEA runs are set up with h and P by using the enthalpy output from the corresponding case. For both codes, a reduced set of 19 chemical species is considered in order to reduce the number of trace species present in the converged equilibrium results and to improve computational speed. The following species are included: N, NH₃, N₂, NO, NO₂, NO₃, CH₄, C₂H₄, CO, CO₂, O, OH, O₂, H, H₂, H₂O, HO₂, H₂O₂, Ar.

Two different types of verification are performed. First, the predicted chemical-equilibrium compositions are compared to ensure that the proper amount of each chemical species is present at each test point. Next, the actual thermodynamic properties (p , T , ρ , h , S , C_P , C_V , γ) are compared. To verify the composition, the average discrepancy between the codes is 5.2×10^{-6} moles and the maximum error is 0.00011 moles. The average discrepancy in the prediction of the thermodynamic properties is 0.03%, and the maximum error is 0.52%. These results demonstrate a strong agreement over a wide range of temperature and pressure.

One unavoidable source of discrepancy between the new code and CEA comes from implementation details related to handling trace species, as discussed in Section 3.1.1.3. Figure 3.4 quantifies this effect more clearly, showing the number of species retained in the final solution from CEA for different values of ϕ over a range of temperatures. The number of active species varies most for $\phi = 0$ (from 4 to 11) because, at lower temperatures, the composition of air stays relatively close to atmospheric, but NO_x starts to form and dissociation starts to occur at the higher temperatures. Note that the data in Figure 3.4 are pressure-averaged over the entire range of pressures from Table 3.1. A slight negative correlation exists between pressure and the number of active species in the data, but this is negligible compared with the temperature effect. If a larger set of species were considered, the pressure effect could be more pronounced.

3.1.3.2 Verification of Chemical Equilibrium

The first verification serves to confirm that the new code returns the same chemical composition as does CEA over the verification grid from Table 3.1. The comparison is done on a per-species basis and is measured with absolute differences. Air, even when combusted with $\phi = 0.44$, is composed of over 70% diatomic nitrogen, which means that any other chemical species (e.g., CO₂, H₂O), although important to the thermodynamic properties, makes up less than 30% of the overall gas. Some species (e.g., NH₃, NO₃) are present only in trace amounts and have almost no impact on the thermodynamics. The accuracy of the amount of trace species predicted by using a chemical-equilibrium method is highly

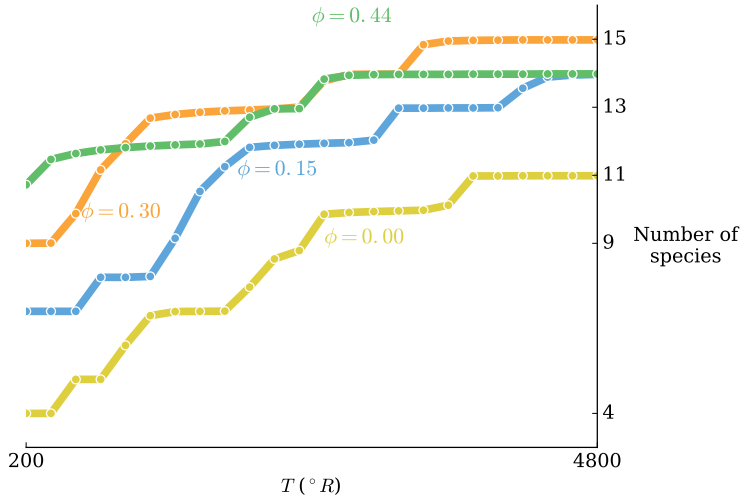


Figure 3.4: Variation of total number of active chemical species in CEA solutions with respect to temperature.

limited but is still of practical significance to ensure that the two codes predict the same trace species. The low-concentration of many species requires an absolute error to measure the discrepancy between codes, and, to be meaningful, absolute error requires knowledge of the actual value for n_j . Figure 3.5 shows the accuracy of the predicted values for n averaged over the full T and P verification set as a function of equivalence ratio. The mean n_j are shown as solid blue lines and can be compared with the absolute error $\|n_{j \text{ CEA}} - n_j\|_2$, which is represented as orange lines. Most of the errors are at least two orders of magnitude smaller than the mean concentrations, indicating strong agreement between the two codes. For NH_3 and NO_3 the discrepancies are the same order of magnitude as the mean value because CEA results includes these species at the lower limit of 10^{-10} . These two species further highlight the subtle difference between the trace-species method for CEA and the new code. At such small concentrations, these species do not have a meaningful impact on the thermodynamic properties. Note that CH_4 and C_2H_4 are excluded from Figure 3.5 because they are always trace species for CEA, and their compositions are always below 10^{-13} for the new code.

In addition to showing the discrepancy for each species individually, Figure 3.6 also shows how the norm of the absolute error, $\|n_{\text{CEA}} - n\|_2$, varies with T and P for the case $\phi = 0.44$. Although small, there is a clear trend toward increasing discrepancy with higher temperature and a much weaker correlation with increasing pressure. Although the discrepancy grows from 3×10^{-5} to 2×10^{-4} upon moving from the lower-left corner to the upper-right corner, it is still small. This trend is consistent with Figure 3.4, where CEA starts introducing small concentrations of new species as the temperature rises. Because

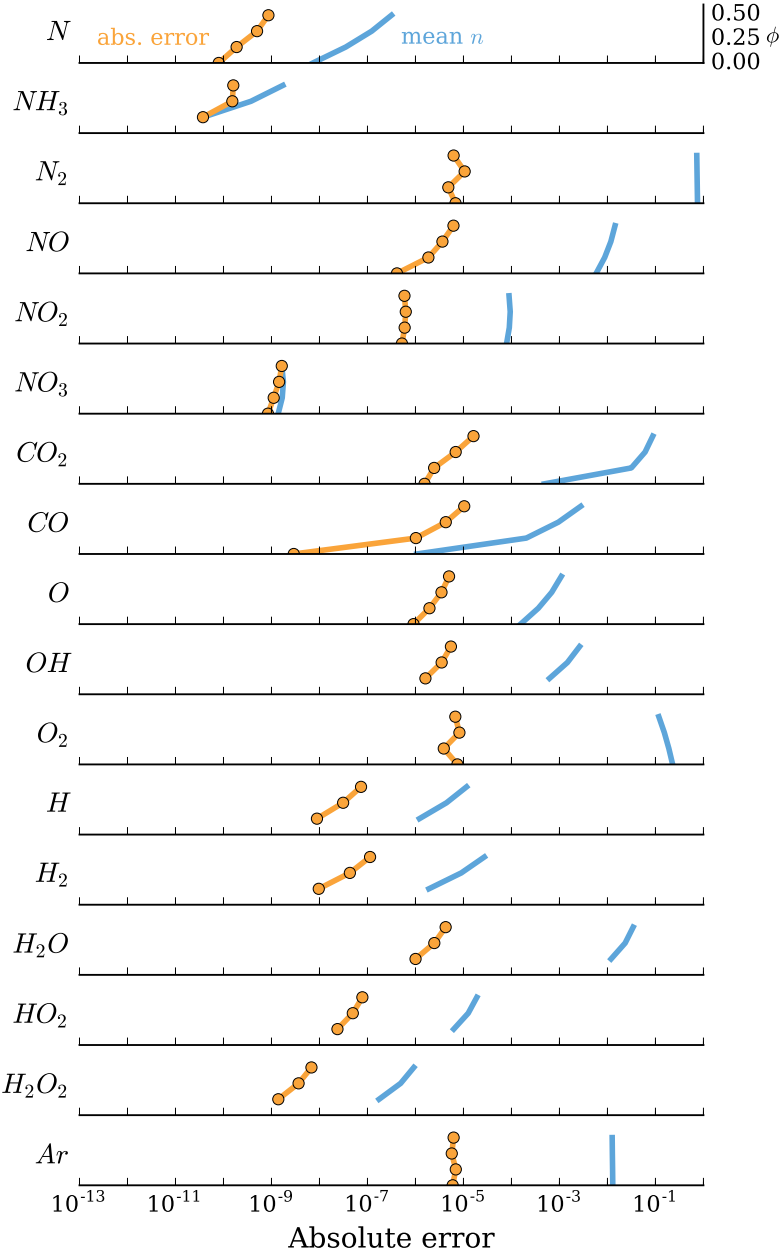


Figure 3.5: Mean differences between equilibrium gas compositions predicted by CEA and by proposed code.

different methods are used to handle these trace species, we expect additional discrepancy in areas where trace species are prevalent. Figures 3.5 and 3.6 demonstrate that both codes give results that are in strong agreement in terms of overall composition across the entire verification grid. The overall conclusion is that the proposed code and CEA both compute the same composition, within solver tolerance.

From a cycle-analysis perspective, the composition vector n is not important in itself;

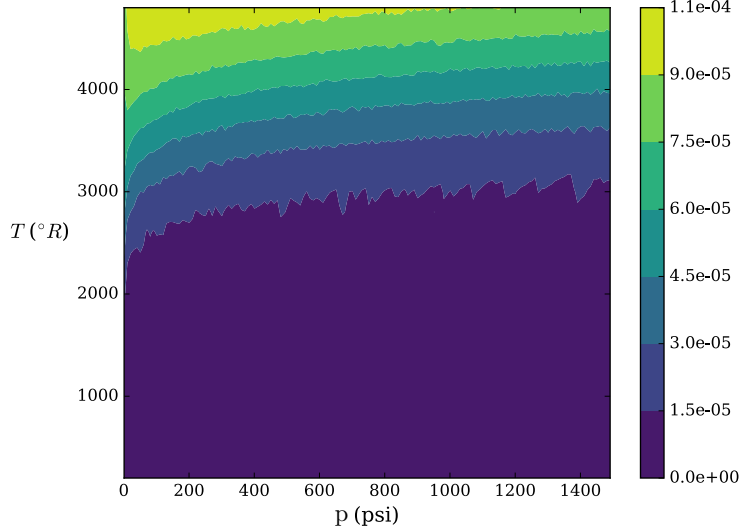


Figure 3.6: l^2 norm of difference between concentration vectors, $\|n_{\text{CEA}} - n\|_2$.

however, because the thermodynamic properties are computed as a function of n , it is indirectly important. Therefore, the verification of predicted composition serves as a preliminary verification of the thermodynamics itself. The next section presents the verification of the thermodynamic properties, but these data reinforce those results by ensuring that the calculations are fundamentally based on the same chemical compositions.

3.1.3.3 Verification of Thermodynamic Properties

We use relative measurements to compare the thermodynamic state variables predicted by CEA with those predicted by the new code. Figure 3.7 shows mean discrepancy, measured across the full verification grid, for entropy S , temperature T , enthalpy h , density ρ , pressure P , specific-heat ratio γ , and specific heat at constant pressure C_P . The mean error for all cases, across all properties, is 0.03%, and the maximum error is 0.52%. Note that, because both h and P are set directly for the CEA run, from the output of the corresponding cases with the new code, these properties have the lowest errors in Figure 3.7. The other errors are larger but are still less than 0.1%. This demonstrates a strong agreement between CEA and the new code and verifies its predictions for cycle-analysis applications.

3.1.3.4 Verification of Multidisciplinary Derivatives

The derivative accuracy is verified by comparing analytic derivatives (direct method in this case) to finite-difference approximations by using forward-, central-, and backward-difference methods. Figures 3.8 and 3.9 show the relative error between the three finite-

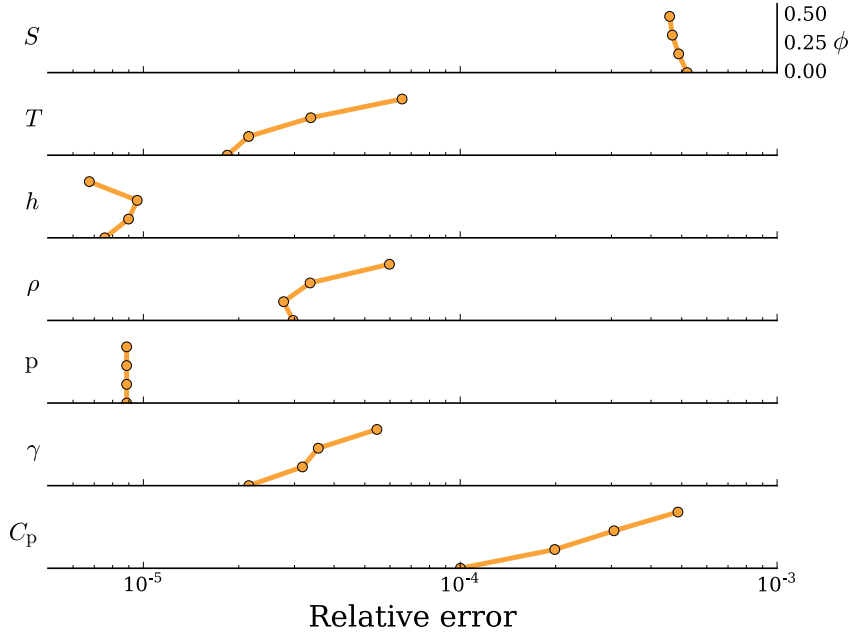


Figure 3.7: Mean relative errors between the thermodynamic states predicted by CEA and by proposed code is less than 0.1%.

difference derivative approximations and the analytic reference values. This relative error is plotted for varying finite-difference step sizes. The plots follow the structure of the Jacobian, showing the derivatives of h , S , ρ , C_P , and γ (rows) with respect to T and P (columns). Figure 3.8 corresponds to standard day conditions (288 K, 1 bar), whereas Figure 3.9 corresponds to a representative cruise condition (1500 K, 10 bar). The analytic and finite-difference derivatives all agree to at least 10^{-5} , although the point of best agreement occurs at different step sizes for different variables.

Whereas the results for standard day conditions in Figure 3.8 show good agreement for all step sizes, the results for the cruise condition in Figure 3.9 shows a dramatic increase in accuracy when the relative step-size is less than 10^{-5} . At cruise conditions, the temperature and pressure are higher, and the converged mixture contains many more active species, which makes the solution more sensitive to input values. Thus, keeping the step size sufficiently small to prevent major changes in the solution is the key to obtaining accurate finite-difference approximations. The central-difference approximation converges faster than the forward or backward schemes and offers better overall accuracy over a range of step sizes. This is expected because central differencing is second order accurate, whereas the other two schemes are first order. However, this accuracy comes at a cost because central differencing requires two function evaluations for each derivative.

Figure 3.10 shows the computational times for assembling the full 5×2 Jacobian of the

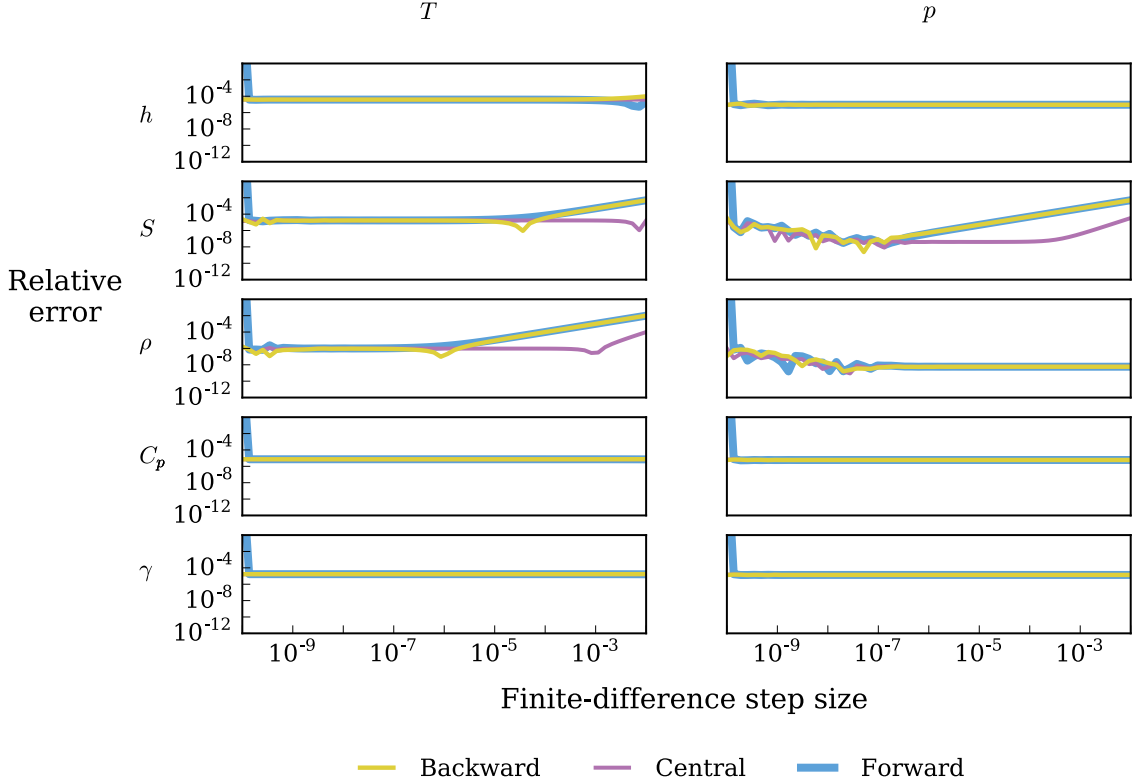


Figure 3.8: Relative error of finite-difference approximations versus step size obtained for standard day conditions and by using computed analytic values as reference.

responses with respect to the design variables. All computational times were measured on an Apple MacBook Pro laptop with a 2.6 GHz dual-core Intel Core i5 processor and 16 GB of memory. The computational cost of the central-difference approximation is twice that of the right- and left-difference schemes. Computing the derivatives with the direct method is faster than with the finite-difference approximations because each finite-difference step requires the convergence of the full nonlinear model, as opposed to the solution of a linear system for the direct method.

Of the two analytic methods, the direct method is faster than the adjoint method for this problem. In this case, the direct method is expected to be faster because it involves two independent variables and five responses. Thus, for the direct method, two linear solutions are needed to compute the full Jacobian. For the adjoint method, five linear solutions are needed. For problems with more design variables than constraints, the adjoint method would become advantageous.

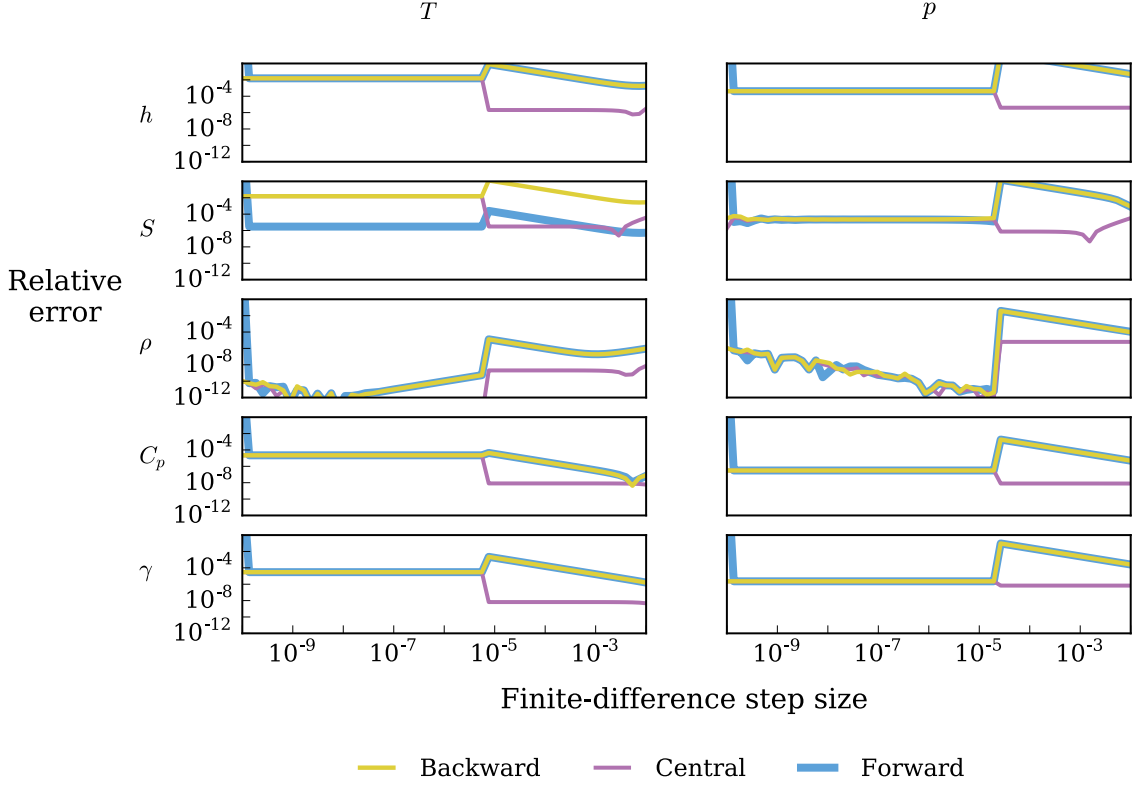


Figure 3.9: Relative error of finite-difference approximations versus step size for cruise conditions and with computed analytic values as reference.

Method	Time (sec)
Direct	0.0046
Adjoint	0.0085
Forward finite difference	0.0110
Central finite difference	0.0213
Backward finite difference	0.0110

Figure 3.10: Wall times required to compute the 5×2 Jacobian by using analytic methods (direct and adjoint) and finite-difference approximations.

3.1.4 Optimization Results

3.1.4.1 Equivalence Ratio Optimization

To demonstrate the use of analytic derivatives in a gradient-based optimization, we ran a series of unconstrained optimizations at a fixed pre-combustion gas temperature of $518^{\circ}R$. Each optimization seeks to maximize the combustion temperature by varying ϕ for a given fixed pressure. We solved 200 optimizations for pressures ranging from 15 to 1500 psi. Figure 3.11 plots the optimal temperatures and the corresponding values of ϕ for the various

pressures. The maximum temperatures occur for ϕ between 1.02 and 1.07, which seems counterintuitive. Under the assumption of perfect combustion, the maximum temperature would occur at the stoichiometric value, $\phi = 1$, where every molecule of diatomic oxygen would be converted to water. However, equilibrium calculations take into account dissociation effects, which simultaneously lower the maximum achievable temperature and cause that temperature to occur at a richer ϕ [93]. The effect of dissociation becomes less severe at higher pressures, which tends to favor the creation of slightly larger molecules, and the reaction more closely approximates ideal combustion. This is shown in Figure 3.11 by both the increasing maximum temperature and the decreasing optimal ϕ as pressure increases. These optimization problems are solved by using gradients computed with both the finite-difference method and the adjoint method. The results are identical in terms of both overall execution time and final objective value because, for this problem with a single design variable, the adjoint method does not significantly improve the speed or accuracy.

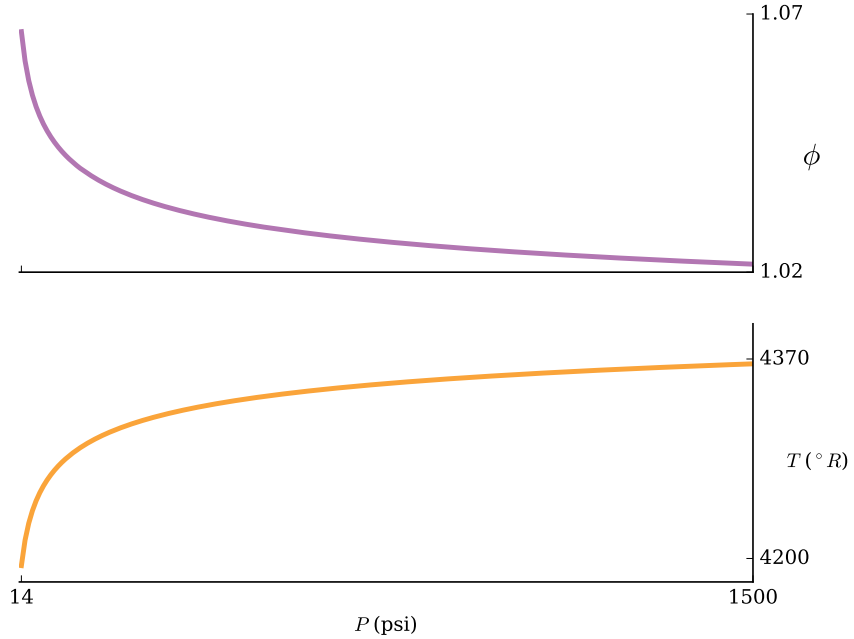


Figure 3.11: Air-fuel equivalence ratio ϕ that maximizes the combustion temperature T as a function of pressure P ranging from 15 to 1500 psi.

3.1.4.2 Equivalence Ratio and Pressure Optimization

The previous results establish that combustion becomes more efficient as pressure increases, even when accounting for equilibrium-chemistry effects. Therefore, we expect that including pressure as a design variable would yield the same result without requiring

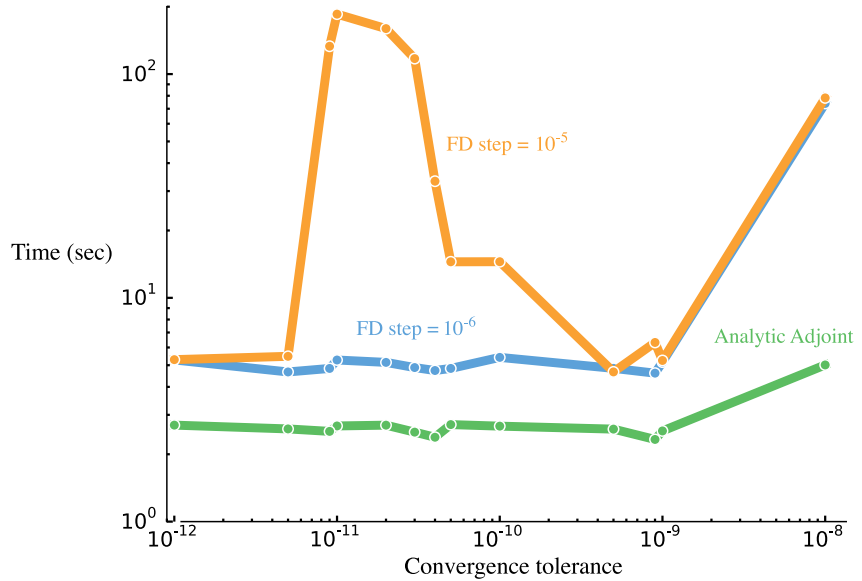


Figure 3.12: Optimization wall time versus tolerance of chemical-equilibrium solver obtained by using analytic and finite-difference methods to compute derivatives.

the parameter study for pressure. To verify this, a second series of optimizations are solved with both ϕ and P as design variables, again seeking to maximize combustion temperature. For this set of optimizations, the tolerance of the chemical equilibrium numerical solver is varied from 10^{-8} to 10^{-12} to test how sensitive the the optimization is to the accuracy of the solution. Again, we used two methods to compute derivatives: the adjoint method and the forward finite-difference approximation. Both derivative methods converge to $\phi = 1.021$ and $P = 1500$ psi, which is consistent with the previous optimization results shown in Figure 3.11. However, unlike the single-design-variable optimization, the adjoint method clearly performs better than the finite-difference method. The finite- difference approximation is at least twice as expensive as the adjoint method, as shown in Figure 3.12. One of the main challenges with using finite-difference derivatives is the need to have tight tolerances for the solvers, such as the one used to converge chemical equilibrium. The data in Figure 3.12 quantify this effect by comparing the performance for different tolerances of chemical- equilibrium solvers. The optimizations that use adjoint-computed gradients require a nearly constant computation time. However, the optimizations that use finite-difference derivatives require between 5.5 and 110 s, depending on solver tolerance and finite-difference step size. This wide range in computational time results from inaccurate derivatives, which force the optimizer to iterate more to converge to the required tolerance. The worst performance occurs when using a step size of 10^{-6} with tolerances between 10^{-11} and 10^{-10} , but the times are reduced for step sizes between 10^{-10} and 10^{-9} . This er-

ratic behavior is particularly troubling and shows that finite-difference approximations are not reliable. For both step sizes, with a solver tolerance of 10^{-8} , the computational times started to rise. Beyond that point, numerical noise prevents the optimizer from converging when using finite-difference derivatives. This result highlights the value of the analytic approach. Even for just two design variables, the adjoint derivatives enable both faster and more stable optimization.

3.2 Building a modular propulsion analysis library with analytic derivatives

The central contribution of this research is the development of the new differentiable formulation for chemical equilibrium solves detailed in the previous section. The implementation of that new formulation forms the thermodynamic core of pyCycle, which was the necessary first step to enabling its further development. Additional development was needed to implement the actual propulsion cycle modeling physics on top of the thermodynamics core.

Following the modular design of NPSS, propulsion models are constructed from a set of interconnected cycle **Elements** (e.g. inlet, compressor, combustor, turbine, nozzle, etc.). A standard library of the most commonly used elements is provided —custom elements can also be defined as needed—and a user will assemble them to construct a disciplinary analysis model of a specific propulsion system. For example, Figure 3.13 shows a layout of elements to model a notional under-wing engine cycle for the STARC-ABL aircraft concept. This engine is a separate flow, high-bypass-ratio turbofan with the addition of a generator attached to the low pressure spool to provide power to the aft BLI propulsor. Each box in the diagram is a separate element. The blue arrows indicate that flow information (e.g. temperature, pressure, mass-flow) are being exchanged. The red arrows indicate that shaft power information is being exchanged.

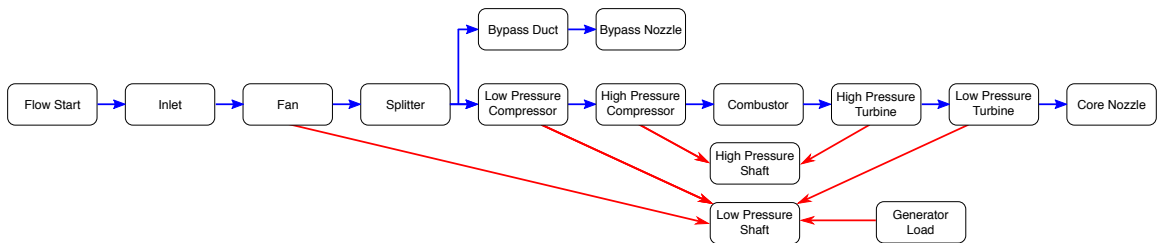


Figure 3.13: Diagram of how cycle elements are combined in a pyCycle model to construct a propulsion analysis for a specific engine cycle. Each box is a single element.

In pyCycle, all of these propulsion elements are constructed as OpenMDAO groups, which internally consist of a set of engineering components and thermodynamic solver sub-groups. The engineering calculations in pyCycle have been extracted directly from NPSS, and as such do not represent a significant new contribution in and of themselves. However, the structure of a pyCycle element is different than that of its analogous NPSS element due to the need to provide analytic derivatives. In NPSS the element itself is the lowest level computational class. If pyCycle had adopted this structure, then it would have been necessary to differentiate across the element level calculations by hand, in order to provide the analytic partial derivatives that OpenMDAO needed. This approach would have been tedious because it would have involved the chain-ruling across multi-step calculations that included multiple calls to the implicit thermodynamic solvers.

Instead of treating the element itself as the lowest level of calculation, pyCycle exposes an additional level of hierarchy to the OpenMDAO framework. This breaks the element calculations down into several smaller sub-component steps which are much simpler to differentiate and allows pyCycle to leverage OpenMDAO's built in efficient linear solver system to compute total derivatives without having to hand derive the chain rule for each new element. To illustrate this more clearly, two example elements are detailed via XDSM [1] diagrams in Figures 3.14 and 3.15. In both figures, the red components represent the engineering calculations and the blue components represent chemical equilibrium solvers. Figure 3.14 shows a very simple element, a duct, whose effect is to apply a pressure loss and heat addition to an input flow. This calculation is accomplished with a single enthalpy-pressure solver. Figure 3.15, representing a basic compressor element, shows a more complex calculation that requires two distinct enthalpy-pressure solvers, with engineering calculations in between them. The need for two chemical equilibrium solvers arises due to the definition of adiabatic efficiency ($\eta_{\text{adiabatic}}$) used for compressors:

$$h_{\text{total_out}} = \frac{Fl_{\text{ideal:h}} - Fl_{I:\text{tot:h}}}{\eta_{\text{adiabatic}}} + Fl_{I:\text{tot:h}}. \quad (3.27)$$

In order to apply this definition to compute the real exit enthalpy of the flow, first you must know the ideal enthalpy ($Fl_{\text{ideal:h}}$). That is computed by applying the prescribed pressure ratio (PR) to the incoming total pressure ($Fl_{I:\text{tot:p}}$) and using the resulting exit pressure as the input to an enthalpy-pressure solver that computes the ideal exit conditions. Once the ideal conditions are known, the real exit conditions can be computed by using the known exit pressure and the exit enthalpy — computed from Equation (3.27) — as the inputs to a second enthalpy-pressure solver.

The primary concept to understand from Figures 3.14 and 3.15 is that each propulsion

element is composed of potentially large number of calculations with multiple chemical equilibrium solvers used in series with each other. If the elements themselves were implemented as OpenMDAO components (rather than groups), in the same fashion as is done in NPSS, each one would require careful application of the chain-rule in combination with the direct or adjoint methods—Equations (2.1) and (2.5)—to compute the necessary partial derivatives for pyCycle. Instead, by building elements as groups of sub-components the pyCycle allows OpenMDAO’s built in capability to make the task of computing partial derivatives simpler.

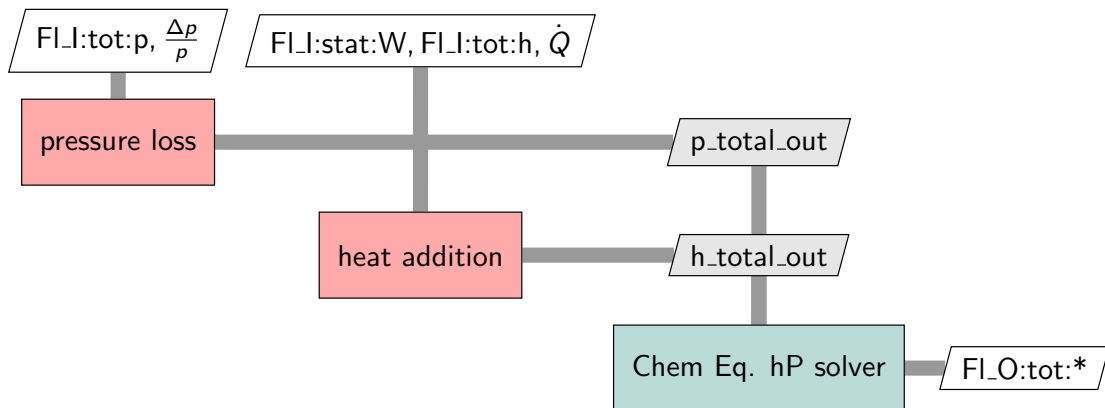


Figure 3.14: XDSM diagram for the pyCycle **Duct** element. Engineering calculations are shown as red boxes. Chemical equilibrium flow solves are shown in blue.

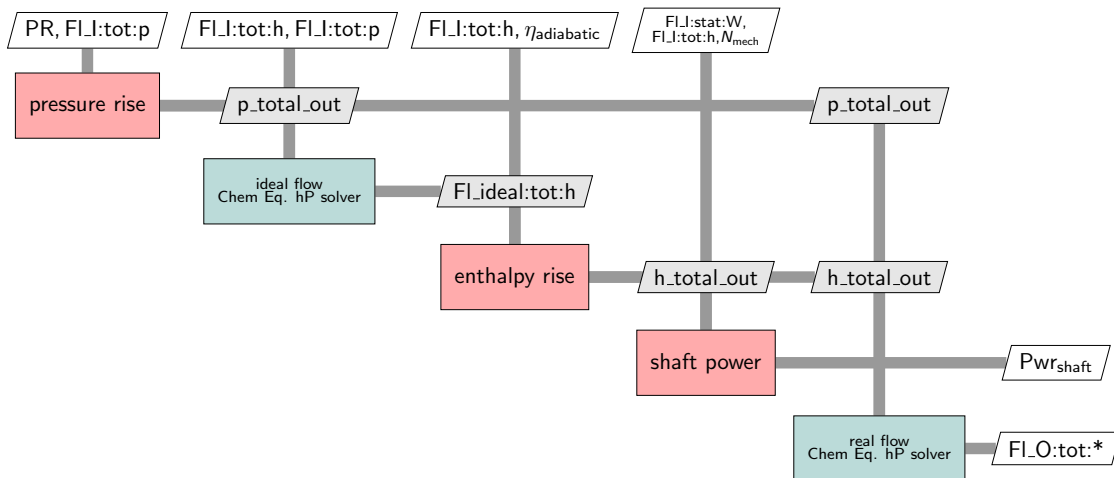


Figure 3.15: XDSM diagram for the pyCycle **Compressor** element. Engineering calculations are shown as red boxes. Chemical equilibrium flow solves are shown in blue.

3.3 Summary

The need to incorporate propulsion cycle modeling into the MDO of aircraft motivated the development of a new propulsion cycle analysis model that can efficiently compute derivatives. The first step in developing the new disciplinary analysis tools was to develop a new chemical equilibrium thermodynamics method that predicts the gas properties of air and fuel-air mixtures for a wide range of fuels in a computationally efficient manner. The major contribution of the new method was the addition of analytic derivative computation (both direct and adjoint). To enable the computation of derivatives, it was necessary to re-formulate the mechanism for handling trace-species in the chemical equilibrium solver to create a continuous analysis response.

The new method to converge a chemical equilibrium analysis was implemented inside the OpenMDAO framework. This implementation was verified by comparing its results against those obtained with the CEA code over a wide range of temperatures, pressures, and equivalence ratios. The verification results closely match, with a maximum discrepancy between the proposed implementation and CEA of less than 0.1%. In addition to validating the analysis, the accuracy of the analytic derivatives was verified by comparing them to finite-difference approximations. The analytic derivatives agree with the finite-difference approximations to within a relative error of $O(10^{-5})$.

The value of the analytic-derivatives approach was further demonstrated via two optimizations whose goal was to maximize the combustion temperature with respect to pressure and equivalence ratio. These optimizations compare the performance of the adjoint derivatives with that of the finite-difference derivatives and show that, even for an optimization with only two design variables, adjoint derivatives can significantly reduce the computational cost and increase the numerical stability. The improvements in speed and accuracy clearly demonstrate the value of the adjoint derivatives for optimization applications and suggest that similar improvements in performance for larger propulsion-cycle analyses are possible. With the verified analysis and derivatives, the thermodynamics solver was complete and could serve as the foundation for a general propulsion modeling tool called pyCycle. pyCycle is essentially a general purpose cycle modeling library, providing propulsion elements (e.g. inlet, compressor, nozzle, etc.) which can then be combined to construct an actual propulsion analysis. All of the propulsion analyses used in this research were built with pyCycle.

CHAPTER 4

Quantifying the importance of aeropropulsive coupling in BLI applications

The traditional approach to airframe and propulsion design is to work with them separately, and then size the engine to match the airframe using simple thrust scaling. This works well when the propulsion system is placed in freestream air, away from the aerodynamic influence of the airframe. In this case, it is reasonable to assume that small changes to either system do not affect the other.

This assumption is no longer completely valid for BLI configurations because changes to the airframe shape directly affect the flow coming into the propulsor, and conversely, changes in the propulsor design directly affect the flow over the airframe. The degree to which the assumption becomes invalid depends on the strength of the aeropropulsive coupling in any given aircraft. As discussed in Chapter 1, nearly all of the existing research into BLI propulsion systems has used an uncoupled formulation, and therefore implicitly has assumed that the coupling does not dominate the performance.

This chapter presents results showing that fully coupled models are necessary to accurately model the performance of BLI propulsion systems. To generate these results I developed a fully coupled aeropropulsive model of BLI propulsor on a simplified STARC-ABL fuselage configuration. I then examined the change in fuselage aerodynamic performance and propulsor performance when varying the propulsor fan pressure ratio (FPR), and analyze the results to quantify the importance of the aeropropulsive coupling.

4.1 Modeling

A simplified, axisymmetric model of the aft mounted BLI propulsor for the STARC-ABL aircraft configuration was created. The actual aircraft would not have perfectly axisymmetric flow entering the BLI propulsor, due to the presence of the tail, the downwash from the

wings, and the non-symmetric aft fuselage. However, for the sake of model simplicity and reduced computational cost, I have assumed that the flow is axisymmetric. This allows for a much more computationally efficient aerodynamic model and also allows for a more fundamental investigation of the aeropropulsive coupling because the confounding effects of the non-axisymmetric flow are not present. This simplified, axisymmetric, STARC-ABL-like configuration is pictured with relevant dimensions in Figure 4.1. The dimensions are based loosely off a 737-900, but the wings and tail have been removed to allow for the simplification.

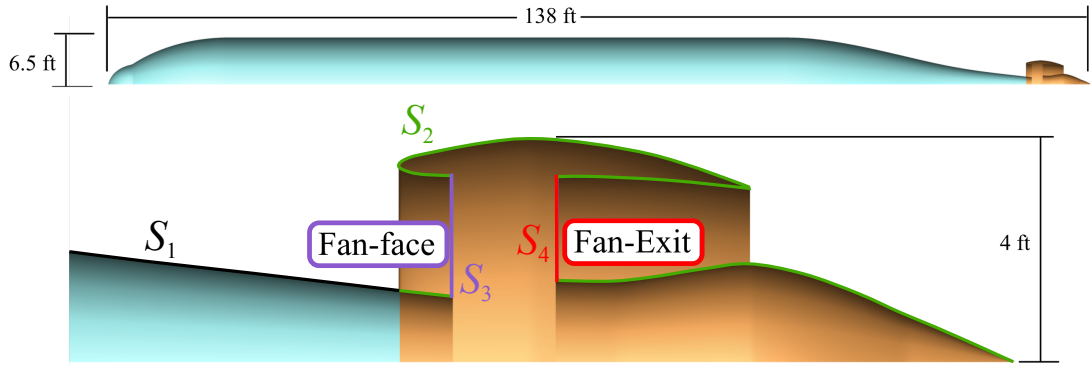


Figure 4.1: Axisymmetric fuselage with aft mounted BLI propulsor representing a simplified STARC-ABL configuration.

4.1.1 Propulsion model

The propulsor model used for this study is extremely simple, comprised only of a single compressor representing the fan. The model inputs are FPR, and total pressure and temperature at the fan-face ($p_t^{\text{FE}}, T_t^{\text{FE}}$) and the required fan shaft power ($\text{Pwr}_{\text{shaft}}$). The outputs are the total temperature and pressure at the fan exit, and the mass flow rate (\dot{m}) for the fixed shaft power of 3,500 hp. Welstead and Felder [27] selected 3,500 hp in their original work on STARC-ABL by sizing their propulsor to capture about 70% of boundary layer. The justification for this choice was based on an analysis that indicated that increasing the propulsor power beyond that level would achieve only marginal gains. For this study, I chose to retain that assumed shaft power of 3,500 hp in order to provide the most direct comparison against the original work. The XDSM diagram of this model is shown in Figure 4.2, including the Newton solver that is used to enforce the assumed 3500 hp on the shaft. The solver varies the \dot{m} until $\mathcal{R}_{\text{pwr}} = \text{Pwr}_{\text{shaft}} - 3500 = 0$.

The fan adiabatic efficiency ($\eta_{\text{adiabatic}}$) is computed as a function of FPR. At a lower FPR, less flow turning is required, and hence a higher adiabatic efficiency can be achieved.

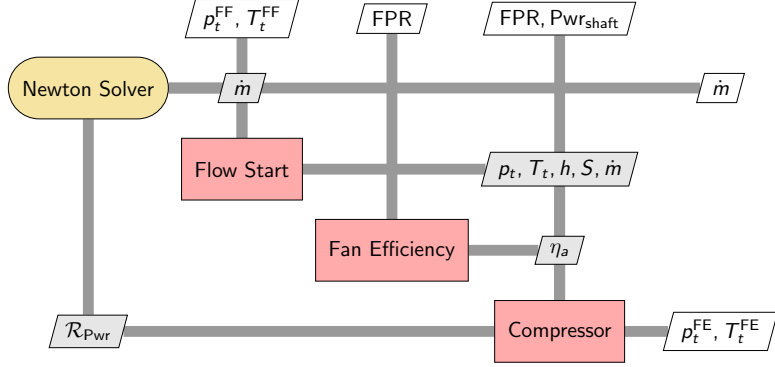


Figure 4.2: XDSM [1] diagram of the propulsor model, including the Newton solver used to find the required mass flow rate to satisfy the shaft power residual ($\mathcal{R}_{\text{pwr}} = \text{Pwr}_{\text{shaft}} - 3500 = 0$)

We assume the following linear relationship between η_a and FPR,

$$\eta_{\text{adiabatic}} = 1.066 - 0.0866\text{FPR} , \quad (4.1)$$

where the constants were chosen to give 96.2% efficiency at a FPR=1.2 and 95% efficiency at FPR=1.4. This linear fit for fan adiabatic efficiency is derived from data published in two studies on next-generation subsonic transport aircraft for the NASA Advanced Air Transport Technologies Project [23, 94]

The converged \dot{m} is ultimately passed to the aerodynamics solver so that it can find the correct nacelle diameter to give that value. There is a relationship between FPR and fan diameter because for a lower FPR the fan will consume more mass flow given the same shaft power. This relationship is communicated from the propulsion model to the aerodynamics model via the output \dot{m} .

4.1.2 BLI Aerodynamic Model

The aerodynamic model uses the RANS solver ADflow [70, 56], which is an efficient viscous adjoint with an in-memory interface to Python that greatly simplifies the integration with OpenMDAO. The axisymmetric geometry of the simplified fuselage configuration allows the use of a small structured multiblock mesh with 170,000 cells to capture the relevant physics. On a desktop computer with a 3.6 GHz, 4 core, Intel core-I7 processor and 8 GB of memory, this mesh can be converged 10 orders of magnitude in approximately 2 minutes.

A free-form deformation (FFD) approach [51] was used to parameterize the BLI propul-

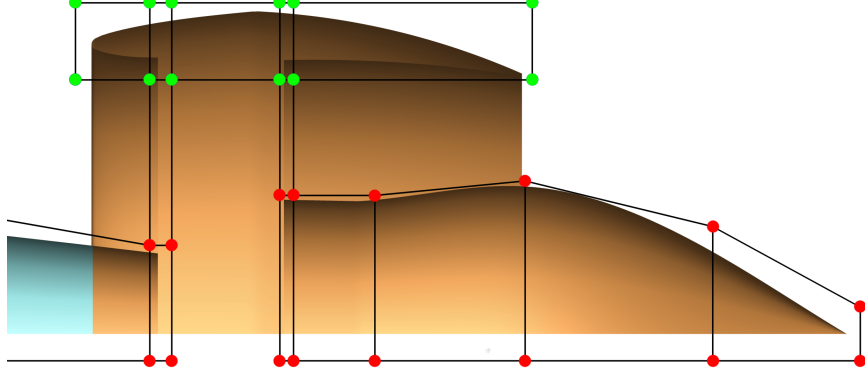


Figure 4.3: Free-form deformation defining the geometry parametrization. Green nodes are allowed to move while red nodes are fixed.

sor so that diameter changes could be represented in the geometry. This was accomplished by defining an FFD that rigidly translates the top of the nacelle up or down to scale the propulsor. Figure 4.3 shows the layout of the FFD boxes that parameterize the geometry, where the green nodes are the corners of the boxes that translate up and down to scale the nacelle diameter. The red nodes are held fixed to maintain the fuselage and nozzle plug geometry.

The propulsion-related inputs to this model are the diameter of the nacelle (d_{nac}) and the two sets boundary conditions that account for the fan: fan-face and fan-exit boundary conditions, as shown in Figure 4.1. At the fan-face, I apply an outflow boundary condition (flow leaving the CFD domain), where the static pressure is specified. At the fan exit, I apply an inflow boundary condition, where the total pressure and temperature are specified.

I compute the net horizontal force on the body, F_x , by integrating the pressure and viscous forces on all solid surfaces, and the pressure and momentum flux contributions on the fan-face and fan-exit, where all the contributions are resolved in the x -direction. This integration can be written as follows:

$$F_x = \iint_{S_1} (p\hat{\mathbf{n}} + \mathbf{f}_{\text{visc}}) \cdot \hat{\mathbf{x}} dS + \iint_{S_2} (p\hat{\mathbf{n}} + \mathbf{f}_{\text{visc}}) \cdot \hat{\mathbf{x}} dS + \iint_{S_3} (p\hat{\mathbf{n}} \cdot \hat{\mathbf{x}} + \rho_3 u_3^2) dS + \iint_{S_4} (p\hat{\mathbf{n}} \cdot \hat{\mathbf{x}} - \rho_4 u_4^2) dS, \quad (4.2)$$

Where S_1, S_2, S_3, S_4 are the surfaces shown in Figure 4.1. It is possible to look at partial integrations over sub sets of the surfaces as well. I will refer to the integrated forces over S_1 as F_{fuse} . Similarly I will refer to integrated forces over S_2, S_3, S_4 as F_{prop} . This is done to facilitate discussion of the results, but this does not imply that fuselage drag, nacelle drag, and thrust can be neatly separated. Neither of these quantities are integrated over a closed control volume and therefore they do not represent true body forces. Furthermore,

for a BLI configuration, thrust and drag are no longer independent quantities that can be separated in a meaningful way since changes in one will cause changes in the other. As part of the modeling, I also integrate the mass flow rates across both the fan-face and fan exit, and the mass-averaged total properties at the fan-face.

4.1.3 Podded configuration aerodynamic model

To provide a consistent point of reference modeled with the same tools and assumptions as the BLI configuration, I constructed an aerodynamic model that emulates a conventional podded configuration. This model consists of two separate aerodynamic simulations: one for the clean fuselage and another for the podded propulsor, as shown in Figure 4.4.

For this decoupled configuration, the aerodynamic performance of the fuselage and the propulsor are assumed to be independent of each other. Using the clean fuselage, I computed a baseline F_{fuse} , and then the F_x of the podded configuration can be found by adding F_{fuse} and F_{prop} from a converged simulation of the independent propulsor.

Other than replacing the fuselage with a rounded spinner in the podded propulsor model, the geometry of the nacelle and boundary conditions of the BLI aerodynamic model are identical to those of the podded one. This allows the same FFD parameterization to be used for both models, and it also means that the same coupling scheme can be used for both the BLI and podded configurations.

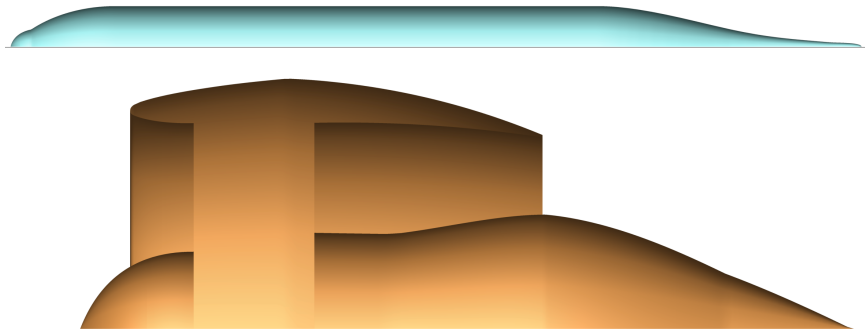


Figure 4.4: Podded propulsor configuration with clean fuselage (top) and detailed view of the propulsor (bottom).

4.1.4 Aeropropulsive coupling

Rodriguez [19] developed the first aeropropulsive coupling scheme, but there has been some more recent work developing coupled aeropropulsive models for supersonic applications. Heath et al. [95] manually coupled a RANS analysis to a propulsion model by

matching the flow areas and mass flow between the two, and by using the propulsion model to predict the static pressure for the fan-face boundary condition. They compared the installed performance and sonic boom for two discrete inlet designs, and the limited number of configurations made manual coupling a reasonable approach. Connolly et al. [96] developed a transient coupled model using an Euler aerodynamic model and 1D gas-dynamics propulsion model for aero-propulso-servo-elasticity applications. They iterated by passing boundary condition values at the interfaces between the two models at every time step to compute state derivatives for the time integration.

This work uses a similar scheme to that of Rodriguez [19] and Connolly et al. [96], where thermodynamic states are exchanged by the two models. However, my method differs in key implementation details. Connely et al. used an implementation that integrates the propulsion model directly into the aerodynamic solver, including the coupling terms as additional state variables to be converged with the rest of the simulation. In this work I use the OpenMDAO framework to manage the multidisciplinary analysis and converge the simulation. This approach is less much intrusive because it requires no modifications to either analysis code, which allows for much greater flexibility in model construction and nonlinear solver structure. The flexible nonlinear solver structure was particularly important for this work, because it was used to construct an efficient scheme for converging the aeropropulsive coupling.

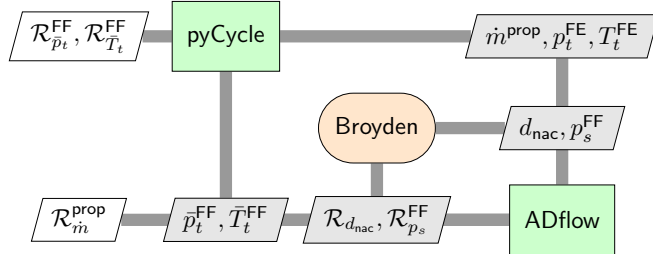


Figure 4.5: XDSM [1] for the coupled aero-propulsive analysis.

The coupling scheme for this work employed a two-level solver structure shown in Figure 4.5, which was used for both podded and BLI configurations. The top level is converged by a nonlinear Gauss–Seidel solver that manages three residuals defined by the following coupling variables: average fan-face total pressure (\bar{p}_t^{FF}), fan-face total temperature (T_t^{FF}), and propulsor mass flow rate (m^{prop}). The inner level is converged using a Broyden solver that handles two additional residuals: $\mathcal{R}_{p_s}^{FF}$ and $\mathcal{R}_{d_{nac}}$. The mass flow rate between the fan-face and fan-exit boundary conditions is balanced by varying fan-face static pressure (p_s^{FF})

to converge the static pressure residual:

$$\mathcal{R}_{p_s}^{\text{FF}} = \dot{m}^{\text{FF}} - \dot{m}^{\text{FE}} . \quad (4.3)$$

The mass flow rate between the aerodynamic and propulsion simulations is balanced by varying the nacelle diameter (d_{nac}) to converge the nacelle diameter residual:

$$\mathcal{R}_{d_{\text{nac}}} = \dot{m}^{\text{prop}} - \dot{m}^{\text{FE}} . \quad (4.4)$$

This last residual is formulated based on the assumption of a fixed input shaft power of 3,500 hp. The propulsion model finds \dot{m}^{prop} so that the fan consumes exactly 3,500 hp and then the nacelle diameter is varied until the mass flow in the aerodynamic model matches that value. This assumption provides a convenient way to compare different propulsor designs. Since they both have the same amount of input power, the configuration that provides the highest overall net F_x is the most efficient.

Note that an alternate reference point is also possible for which the power (and hence \dot{m}^{prop}) would be varied to achieve steady flight ($F_x = 0$). In this case, the design with the lowest power input to the propulsor would be the most efficient. Ultimately, this approach was discarded because part of the STARC-ABL thrust is produced by the under-wing engines and it is not a good assumption that the aft propulsor only zeros out the fuselage drag. The aft propulsor could produce either a larger or smaller portion of the overall thrust, meaning that this simplified configuration would not necessarily have a net zero force on its own. Hence the fixed-power reference lends itself more naturally to this specific simplified configuration because it allowed me to investigate different thrust splits.

4.2 Results

I conducted a trade study by performing a parameter sweep of FPR from 1.2 to 1.35, and then comparing the performance of the podded configuration to that of the BLI configuration. For the podded configuration, I assumed that changes to the fuselage only affect F_{fuse} , and changes to the propulsion system only affect F_{prop} . With BLI, this assumption is no longer valid, and the performance metric is based on the net force in the axial direction (F_x) of the combined fuselage-propulsor system. However, it was still useful to examine F_{prop} and F_{fuse} to understand how these quantities vary across the propulsor design space, and how the net performance is achieved.

All forces are nondimensionalized as follows:

$$C_F = \frac{2F}{\rho_\infty V_\infty^2 A_{\text{ref}}} , \quad (4.5)$$

where A_{ref} is the reference wing area for the STARC-ABL aircraft. The values used in the nondimensionalization are listed in Table 4.1. This table includes a reference length, l_{ref} , whose value is the baseline outer nacelle radius and will be used to nondimensionalize the coordinates in the boundary layer.

In the convention used here, the sign of the force indicates the direction of action: Positive values represent forward force that would cause acceleration, while negative values represent backward force that would cause deceleration. Note that this sign convention is retained even when breaking F_x into F_{prop} and F_{fuse} , so it is expected that F_{prop} is positive and F_{fuse} issues negative.

Table 4.1: Reference values used in the nondimensionalization.

p_∞	3.834 psi
ρ_∞	0.0008 slug/ft ³
V_∞	707.3 ft/sec
A_{ref}	1,400 ft ²
l_{ref}	4 ft

When working with force coefficients it is common to refer to *counts of force*, which correspond to $10^4 \times C_F$. The results presented below show that the BLI system outperforms the conventional podded configuration by at least 24 force counts across the range of FPR designs considered, and that the aerodynamics and the propulsive improvements both contribute equally to the gains. Thus, a fully coupled analysis is necessary to accurately capture the full BLI effect.

The aerodynamic benefit of the BLI configuration is shown qualitatively in Figure 4.6, which plots contours of Mach number. The bottom image represents the clean fuselage, the middle one is a BLI configuration with FPR = 1.35, and the top one is a BLI configuration with FPR = 1.2. As the FPR is reduced for a fixed input power to the fan, the mass flow rate increases, requiring a larger nacelle. The diameter of the nacelle has a strong influence on the height of the boundary layer on the aft fuselage. The largest nacelle, for FPR = 1.2, also has the thickest boundary layer. The boundary layer heights (δ) measured at the nacelle lip for the three configurations are listed in Table 4.2. The boundary layer grows 15% between the podded configuration and the FPR = 1.35 BLI configuration, while for the FPR = 1.2 design it grows by 25%. This variation in the boundary layer

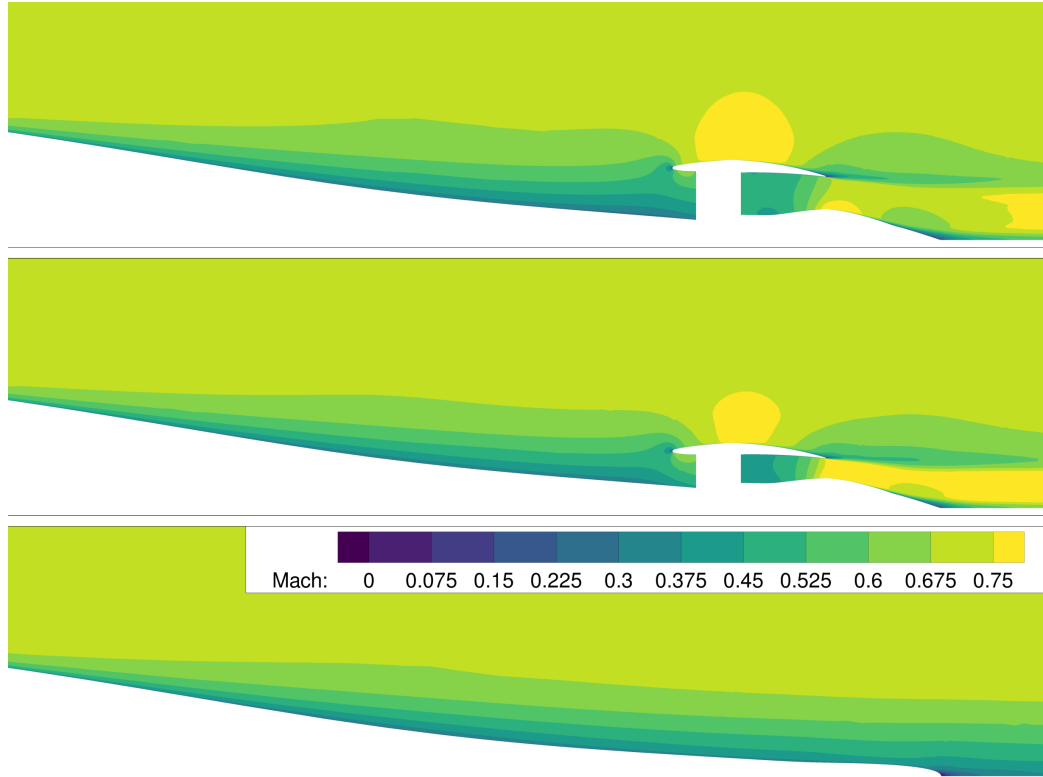


Figure 4.6: Converged flow solutions for FPR = 1.2 (top), FPR = 1.35 (middle), and the clean fuselage (bottom) designs

profile as a function of the nacelle design demonstrates a sensitivity of the aerodynamics with respect to the propulsion design variable (FPR).

Table 4.2: Boundary layer height at the nacelle lip for podded and BLI configurations.

Configuration	δ (ft)	Change
Podded	4.0	0 %
BLI with FPR = 1.35	4.6	15%
BLI with FPR = 1.20	5.0	25%

4.2.1 Net force as a function of FPR

The calculation of C_{F_x} must be handled slightly differently for the podded and BLI configurations. For the podded configuration, the force on the fuselage is constant and is independent of any changes to the pod. Therefore, the contribution of the fuselage can be computed at the given flight condition, and then combined with the contribution from the

podded propulsor for any given FPR as follows:

$$C_{F_x} = C_{F_{\text{prop}}} + C_{F_{\text{fuse}}}, \quad (4.6)$$

where $C_{F_{\text{fuse}}} = -0.008321$.

For the BLI configuration, I compute the net force integration on the whole wetted surface, and fan-face and fan exit, as detailed in Equation (4.2). A comparison of C_{F_x} between the podded and BLI configurations is plotted in Figure 4.7. The primary conclusion from Figure 4.7 is that BLI offers an additional 24 to 27 of net force counts. That represents a 33% increase relative to the conventional podded configuration. The data also shows two key trends: first, for the podded configuration net force is insensitive to FPR; and second, the BLI configuration clearly performs better at lower FPR designs. Further insight into these trends is gained by breaking C_{F_x} down into $C_{F_{\text{fuse}}}$ and $C_{F_{\text{prop}}}$ to look at the contributions from each discipline.

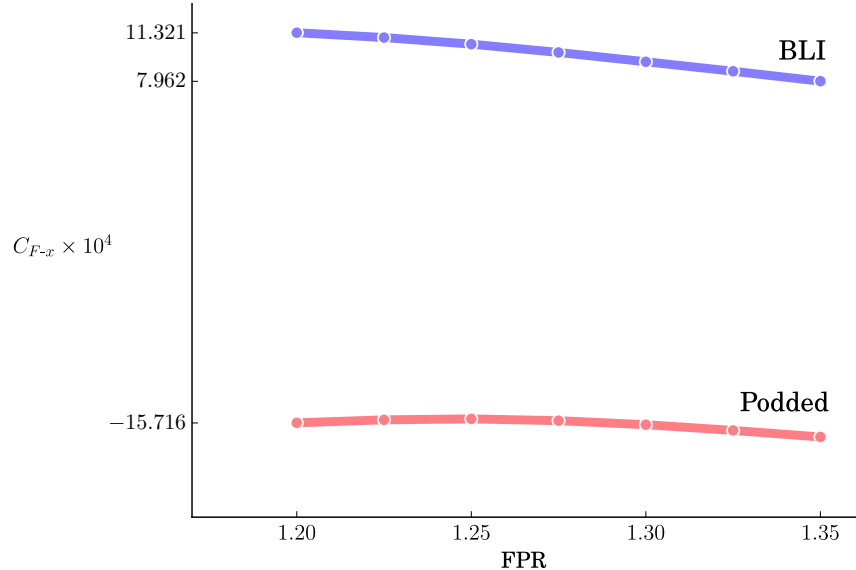


Figure 4.7: Net force on the body (fuselage and propulsor) as a function of design FPR.

4.2.2 Propulsor force as a function of FPR

Figure 4.8 shows the variation of the propulsor force with FPR for both podded and BLI configurations. For the podded configuration, where F_{fuse} is constant, the variation in C_{F_x} is solely due to changes in F_{prop} at different FPR designs. Figure 4.8 shows that there is only a 1.4 force count variation in F_{prop} as a function of FPR for the podded configuration.

This result might be surprising if viewed from a purely thermodynamic perspective. Thermodynamics would predict that F_{prop} would increase as the FPR is lowered due to higher propulsive efficiency and a higher adiabatic efficiency—defined by Eqn. (4.1). However, the coupled analysis accounts for both thermodynamic and aerodynamic installation effects. While the net thrust does go up, the nacelle drag also increases by nearly as much, and hence, the overall effect is a fairly flat response, with slightly better performance near $\text{FPR} = 1.25$.

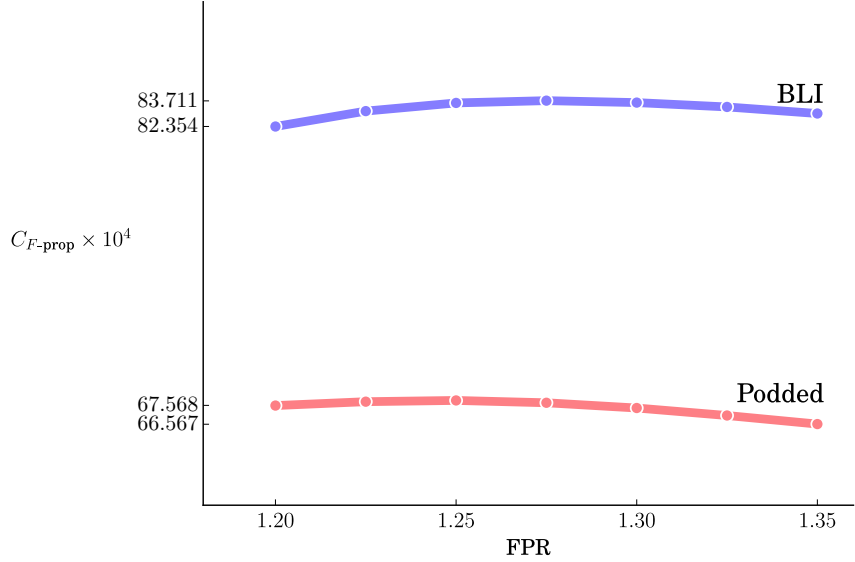


Figure 4.8: Force integrated over propulsor ($C_{F_{\text{prop}}}$) as a function of design FPR.

The drag increases for lower FPR designs because there is a stronger shock on the outer surface of the nacelle for the larger nacelles, as seen in Fig. 4.9. The presence of that shock in both configurations indicates that the nacelle geometry is not ideal. In fact, we can see that the same effect is present for the BLI configuration by looking at Fig. 4.6, where the area of high speed flow is larger for the $\text{FPR} = 1.2$ configuration on top. Although we would normally expect the larger nacelle with a correspondingly larger fan to have more drag, a more optimal aerodynamic shape would reduce this installation penalty considerably. This result highlights the fundamental importance of using optimized shapes when using RANS CFD aerodynamic analyses. Since the solver is highly sensitive to subtle changes in the shape, it becomes important to optimize the shape for each design examined in order to ensure that none are unfairly penalized by an easily corrected shock or otherwise drag-creating flow feature. Later chapters of this thesis introduce shape optimization into the problem to correct for this issue, however since this suboptimal inlet design is used for all the cases presented herein the performance comparison in this chapter is still valid.

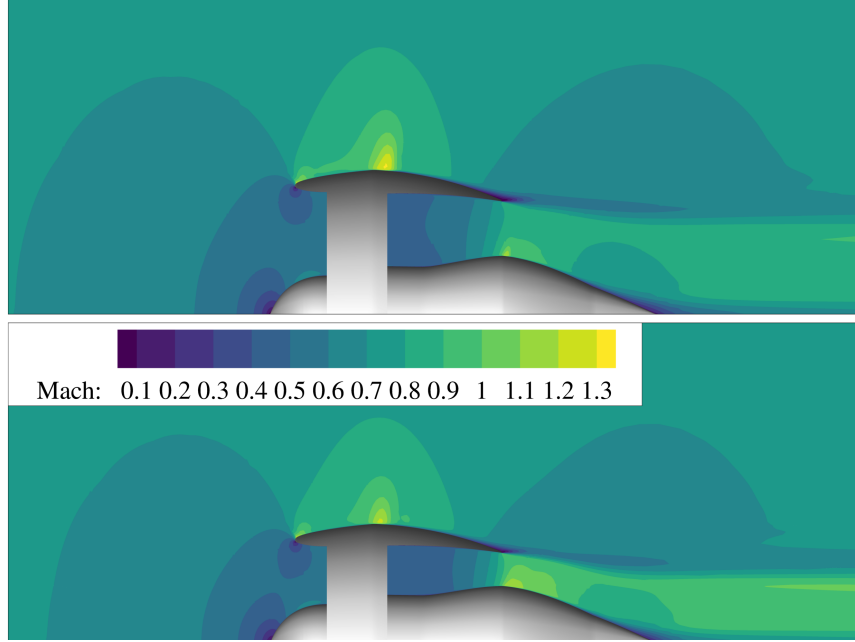


Figure 4.9: Mach contours for the propulsor simulation on the $FPR = 1.2$ (top) and $FPR = 1.35$ (bottom) designs of the podded configuration.

The propulsor force trend for the BLI configuration in Fig. 4.8 is different from the trend in Fig. 4.7. For $FPR = 1.35$, the BLI configuration outperforms the podded configuration by 15.8 force counts. For $FPR = 1.2$, the difference is 16.1 force counts. Although this variation is small, it is still opposite of the variation of C_{F_x} with FPR . This BLI trend occurs because as the nacelle grows, the BLI benefit decreases since a larger percentage of freestream flow is ingested, which results in increased ram drag. Hence, the BLI benefit to the propulsion system becomes less pronounced for lower FPR designs. Additionally, by comparing Fig. 4.7 with Fig. 4.8, we see that only considering the BLI effect on the propulsion analysis would both underpredict the benefit by between 27% and 36%, and result in a different optimal FPR value.

The difference in magnitude and trend between $C_{F_{\text{prop}}}$ and C_{F_x} highlights the importance of using a fully coupled analysis to study BLI. Another important difference between the uncoupled and coupled modeling can be seen by examining the mass-averaged fan-face total pressure, which is defined as

$$\bar{p}_t^{\text{FF}} = \frac{\int_0^{d_{\text{nac}}} p_t(y) \dot{m}(y) dy}{\int_0^{d_{\text{nac}}} \dot{m}(y) dy}. \quad (4.7)$$

For an uncoupled analysis, where we assume that the aerodynamics are unchanged from the podded configuration, $p_t(y)$ and $\dot{m}(y)$ in Eqn. 4.7 are extracted from the boundary

layer profile of the clean fuselage in the podded configuration, and are independent of any propulsion design variable. Therefore, for uncoupled analysis, \bar{p}_t^{FF} only depends on the nacelle diameter. This type of analysis was used by Welstead and Felder [27] in their study of the STARC-ABL configuration, and by Liu et. al [97] and Laskaridis et al. [98] in their studies of a HWB turbo-electric distributed propulsion configuration.

When the analysis is fully coupled, \bar{p}_t^{FF} and \dot{m} are not only a function of the nacelle diameter, but a function of the propulsor design as well, through the FPR. Figure 4.10 compares \bar{p}_t^{FF} as a function of FPR between podded configuration and the BLI configuration. The BLI results are computed using both uncoupled, and coupled analyses. For the podded configuration, \bar{p}_t^{FF} is independent of FPR, since the inlet just ingests from the freestream. The BLI configuration uncoupled analysis (dashed blue line), does capture the inverse relationship of \bar{p}_t^{FF} with FPR, but it over-predicts \bar{p}_t^{FF} by between 4% and 6% compared to the coupled method (solid blue line).

This over-prediction is significant because, as discussed in Chapter 1.2, it impacts the total thrust produced by a propulsor. For an uncoupled model, with the thrust prediction made by the propulsion model, it would mean that the propulsor was predicted to be smaller and lighter than it would need to be in reality. Another issue is that, since the total pressure is different, that means that the incoming average flow velocity must be overpredicted for the uncoupled model. Again, based on the analysis in Chapter 1.2, this means that the ram-drag will also be over-predicted and the BLI benefit under-predicted. So you could simultaneously under-predict the BLI benefit and over-predict the specific mass flow through the engine, giving potentially offsetting errors. This is why the coupled aeropropulsive model is so fundamentally important. Without that, it can become nearly impossible to even ensure that a simplified model is at least predicting performance conservatively.

4.2.3 Fuselage force as a function of FPR

Figure 4.11 shows the aerodynamic contribution to the overall performance. The podded data is constant by definition, since there is no aerodynamic interaction between the propulsor and the fuselage. The BLI configuration has better $C_{F_{\text{fuse}}}$ for all designs by at least 8.2 force counts. However, unlike the forces on the propulsor, $C_{F_{\text{fuse}}}$ for the BLI configuration exhibits a strong variation with FPR. From the FPR = 1.35 design to the FPR = 1.2 design, the $C_{F_{\text{fuse}}}$ improves by an additional 4.0 counts. The total variation in $C_{F_{\text{fuse}}}$ is larger than the total variation in $C_{F_{\text{prop}}}$ observed in Fig. 4.8, indicating that the aerodynamic performance is more sensitive to FPR—a propulsor design variable—than the propulsor performance is.

The sensitivity of the aerodynamics to FPR in the BLI configuration is due to variations

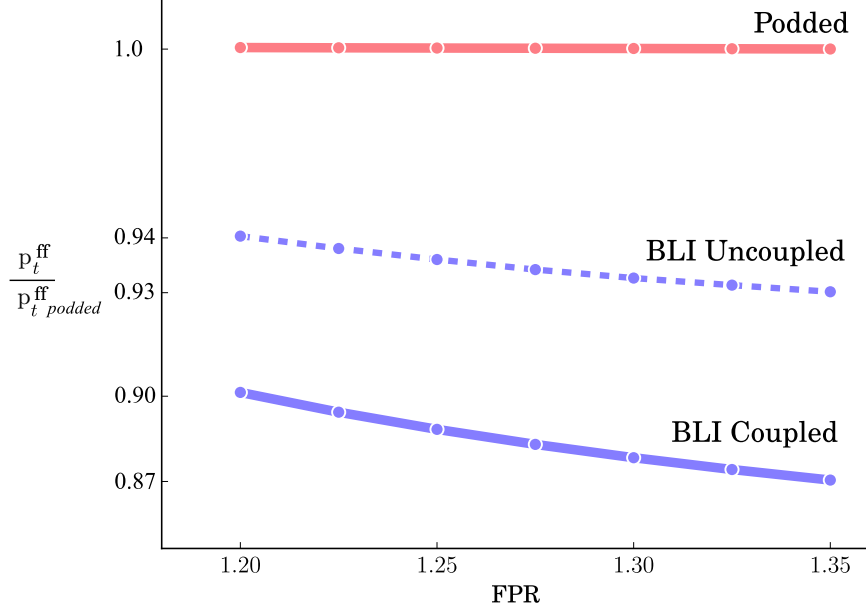


Figure 4.10: Mass-averaged total pressure normalized by the value for the podded configuration as a function of FPR for the podded configuration (pink), the BLI configuration with a fully coupled analysis (solid blue), and a decoupled analysis (dashed blue)

in the flow field in the aft fuselage. We can see this effect qualitatively in Fig. 4.6. The actual velocity profiles for the podded configuration, and the BLI configuration for FPRs of 1.35 and 1.2 are shown in Fig. 4.12, where all distances are normalized by the baseline nacelle outer radius, $l_{\text{ref}} = 4$ ft. We see that the propulsor slows down the flow near the surface, and that this effect extends to about one nacelle radius forward of the fan-face.

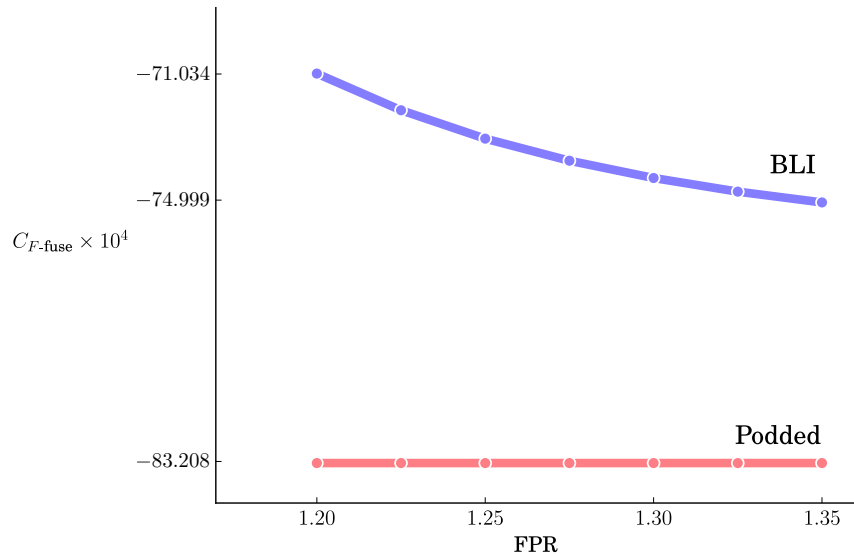


Figure 4.11: Force coefficient on the fuselage, $C_{F_{\text{fuse}}}$ as a function of design FPR.

Also, the larger propulsor for the $FPR = 1.2$ design has a more significant impact on the flow than the smaller propulsor for $FPR = 1.35$.

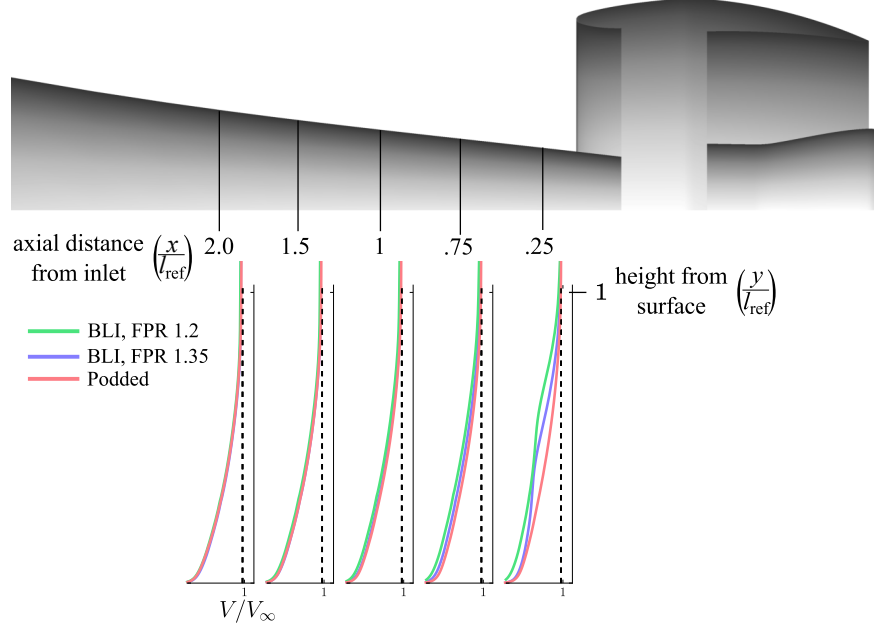


Figure 4.12: Comparison of boundary layer profiles at the aft fuselage between the podded and BLI configurations; $l_{ref} = 4ft$.

The boundary layer profiles demonstrate that the flow on the aft fuselage is influenced by the aft propulsor, and hence provide an aerodynamic justification for the results shown in Fig. 4.10. These profiles explain why the coupled analysis predicts a lower p_t^{FF} than the uncoupled analysis. Even for the uncoupled analysis, the dashed-blue line in Fig. 4.10 shows a loss of total pressure that varies with FPR, and thus with nacelle diameter as well. However, the uncoupled analysis assumes that the boundary layer velocity profile is fixed and independent of the propulsor design. The fully coupled analysis captures the change in the boundary layer as the propulsor diameter changes, which further lowers the total pressure compared to what the uncoupled analysis predicts. The lower flow speeds in the boundary layer might also partially explain the reduced $C_{F_{prop}}$ in the BLI configuration. However, the difference in boundary layer profiles only propagates about one nacelle radius forward, and qualitatively does not seem to indicate a significant reduction in viscous losses to justify the full effect seen in $C_{F_{prop}}$.

To better understand the aerodynamic cause for the change in $C_{F_{prop}}$, we examined the C_p distribution on the surface of the aft fuselage. Figure 4.13 confirms that there is a significant difference in the pressure along the aft fuselage, but it also shows that the effect

reaches farther upstream on the fuselage than the variation in boundary layer profiles. The C_p near the fan-face changes by 50%, but even at 3.5 nacelle radii away from the inlet, there are still differences in the C_p . Hence, the surface pressure effects of the BLI propagate much farther forward than the changes in the velocity profile would suggest. Even small variations in C_p can have a large effect on the body forces, since they act over a large area. The pressure distribution shown in Fig. 4.13 explains the trend for the BLI configuration in Fig. 4.11. As the FPR decreases and the propulsor increases in diameter, the effect of the higher pressure at the fan-face propagates farther upstream and further decreases $C_{F_{\text{prop}}}$.

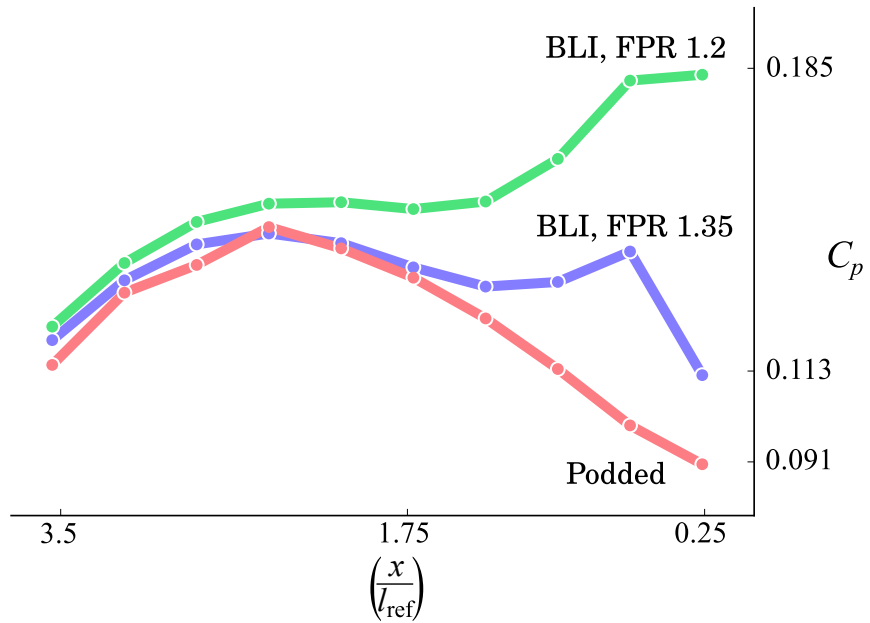


Figure 4.13: Comparison of surface C_p vs axial distance from the inlet (x/l_{ref}) between the podded and BLI configurations vs axial distance with FPRs of 1.35 and 1.2; $l_{\text{ref}} = 4\text{ft}$.

The trends in Fig. 4.13 summarize the most significant finding of this chapter: The presence of the propulsor in a BLI configuration can have a large impact on the pressure distribution along the aerodynamic surface it is attached to. Furthermore, we can see that the details of that interaction are highly sensitive to changes in the propulsor design and shaft input power, which affects the static pressure distribution.

These results show that there is an inverse relationship between the change in the mean static pressure on the fuselage and FPR, but this relationship could be altered by varying other aspects of the propulsor design not considered here. The fan-face static pressure—which affects the static pressure distribution on the aft fuselage—is a function of both throttle setting and inlet design. Throttling down would increase the fan-face static pressure and thus mean static pressure, while throttling up would decrease it. Even for a fixed FPR

and throttle setting, the inlet design could still allow an extra degree of design freedom. By making the inlet more or less diffusive you can alter the interdisciplinary coupling between the fan-face static pressure and the aft fuselage static pressure distribution. Such inlet design changes would have an impact on propulsor performance, but the multidisciplinary effects would allow aero-propulsive trades to seek highest overall system efficiency.

4.3 Summary

This chapter presents a new approach for building coupled aero-propulsive analyses of BLI propulsion systems using a 1D cycle model and a RANS CFD aerodynamic model. The approach was implemented in the OpenMDAO framework, using pyCycle and ADflow for the propulsion and aerodynamic analyses, respectively. A simplified version of NASA's STARC-ABL configuration was modeled, and a parameter sweep of propulsor FPR from 1.2 to 1.35 was performed to study the coupled performance of the aft-mounted BLI propulsor and characterize the contributions from each discipline.

The coupled analysis shows that BLI offers at least 24 force counts of increased performance relative to the podded configuration across the FPR range. This represents a 23% increase in thrust relative to the 67 force counts of thrust for the podded configuration, which clearly demonstrates the large potential for performance improvement due to BLI in this configuration.

The trends were further analyzed by breaking the net force down into aerodynamic and propulsive contributions. The breakdown of the improvements shows that 8 to 12 force counts were due to aerodynamics and 16 counts were due to propulsion. Thus, the BLI configuration benefits from aerodynamics and propulsion are essentially of equal importance. Interestingly, Hall et al. [28] found similar results using a different aircraft configuration and using the power balance method [2]. These results clearly prove the need for a fully coupled model to predict the performance of the BLI configuration, since considering only propulsion or only aerodynamics would only achieve a fraction of the possible improvement.

The BLI benefit to the propulsion system arises primarily from a decrease in incoming momentum flux (a reduction in ram drag). The thrust data presented here shows that this benefit is only a weak function of FPR because of the offsetting thermodynamic improvements and nacelle drag increases. Work in the next chapter will show that an optimized nacelle geometry alleviates some of the drag penalties for the lower FPR designs shown here, and thus alters the trend with respect to FPR. None the less but the general effect of decreased ram drag has been shown to be a fundamental factor in the improved BLI

performance.

The BLI benefit to the aerodynamics was due to higher mean static pressure along the aft section of the fuselage relative to the clean fuselage in the podded configuration, and this higher pressure was caused by the influence of the BLI fan. In the podded configuration the fan-face static pressure is higher than the local static pressure on the aft section of the clean fuselage. When the propulsor is moved down onto the fuselage the relatively higher fan-face static pressure is able to favorably alter the mean static pressure on the aft-fuselage without adversely affecting the pressure forces on the propulsor.

The reduced ram-drag on the propulsor combined with the increased mean static pressure along the aft fuselage combine to create the mutually beneficial affects in the BLI configuration. While the propulsion effect was slightly larger in magnitude, the aerodynamic effect was far more sensitive to FPR. This occurred because, with a fixed input shaft power, the FPR effectively determines the nacelle diameter (i.e., a lower FPR means a larger nacelle). The diameter of the nacelle had a direct effect on how far upstream the BLI effects propagated and meant that lower FPR designs had a much larger aerodynamic effect and a strong multidisciplinary coupling.

The variation in pressure along the surface of the aft fuselage indicates that BLI propulsion systems can have a strong impact on the static pressure distribution of the associated aerodynamic surfaces. For the STARC-ABL configuration, this yields a decrease in drag, but other configurations, such as the MIT D8 or the turbo-electric distributed propulsion HWB, could potentially see additional aerodynamic effects. For these aircraft, the variation in the surface pressure caused by the BLI propulsion system could cause not only propulsion-dependent drag effects, but also lift and pitching moments. This means that BLI could ultimately result in throttle-dependent angle of attack and trim settings. In fact, this exact effect was observed in the wind tunnel experiments on a D8 configuration with powered BLI propulsors [31]. Uranga et al. state that

“During the tests, the model angle of attack was found to change when the propulsor power was varied, through compliance of the force balance, due to lift-producing changes in the flow around the nacelles and reduced pressure on the top aft fuselage of the BLI configuration.”

To the best of my knowledge, this chapter presents the first ever quantitative analysis of the impact and importance of the coupled aeropropulsive effects on BLI. In particular these are the first quantitative results that demonstrate changes in surface pressure distributions as a function of propulsor design and throttle setting. The results clearly show that the overall efficiency gains are both aerodynamic and propulsive and that coupled models are needed to accurately predict magnitudes. Furthermore, the clearly suboptimal flow patterns on the outer nacelle walls also further motivate the use of gradient based optimization in

the subsequent chapters.

CHAPTER 5

Design optimization of a axisymmetric BLI propulsion system

In Chapter 4 results were presented demonstrating that fully coupled aeropropulsive models predict significantly different propulsor inlet conditions compared to uncoupled models. Additional results predicted propulsion dependent aerodynamic effects — changes in C_L , C_D , C_M — that vary with both propulsor design and throttle setting. Since fully coupled aeropropulsive models are necessary in order to accurately analyze BLI systems, it follows that it is equally necessary to consider such models in the design of such systems. In the specific case of the STARC-ABL configuration, the BLI propulsor system is only one part of the overall propulsion system and consequently trades can be made between the under-wing and aft propulsors. Hence in the case of STARC-ABL, there are not only aeropropulsive trades to be considered but fundamental propulsion system design trades which are also impacted by the aeropropulsive performance. This creates a large, highly coupled design problem which can only be solved optimally when using the coupled aeropropulsive model and varying all design variables involved simultaneously. This chapter presents an aeropropulsive sizing analysis for the STARC-ABL aircraft propulsion system, performed using gradient based optimization with analytic derivatives to navigate the large design space efficiently. A two-phased modeling approach was used, with the goal of predicting the best relative sizing for the under-wing and aft-mounted propulsors. In the first phase, the aeropropulsive fuselage is analyzed in isolation from the rest of the propulsion system to study the performance of the BLI propulsor itself and estimate its performance gains. In the second phase, the data from BLI focused analysis is used along with data of under-wing propulsor performance to estimate the best overall power split between the under-wing and aft-mounted propulsors, assuming that the aircraft is at a steady cruise condition. The results show that the BLI configuration offers between 1% to 4.6% reduction in required power at cruise, depending on the assumptions made about the efficiency of the system that transfers the power between the under-wing engines and the aft propulsor.

5.1 Design optimization of the aeropropulsive fuselage

5.1.1 Aerodynamic Model

The aerodynamic analysis for this chapter uses the same simplified, 2-D axisymmetric geometry that was used in Chapter 4, along with the same 170,000 cell grid, and the same outflow/inflow boundary conditions to interface with the propulsion model. The extremely low computational cost of this model motivates its use here, because the goal was to perform a design study composed of many optimizations. As before, two configurations of the simplified geometry are generated: BLI propulsor and podded propulsor. The outflow boundary condition on S_3 is a prescribed uniform static pressure. This assumption is consistent with boundary layer theory, which assumes a constant static pressure at the surface. The total pressure variation caused by the boundary layer and the associated velocity variation is thus carried out of the flow domain as a non-uniform flow at S_3 . The inflow boundary condition on S_4 is defined by a prescribed uniform p_t and T_t , which ultimately is defined by the propulsion model, so while the outflow condition allows for flow non-uniformity, the inflow condition does not. This means that the model assumes that the flow exiting the fan is well mixed.

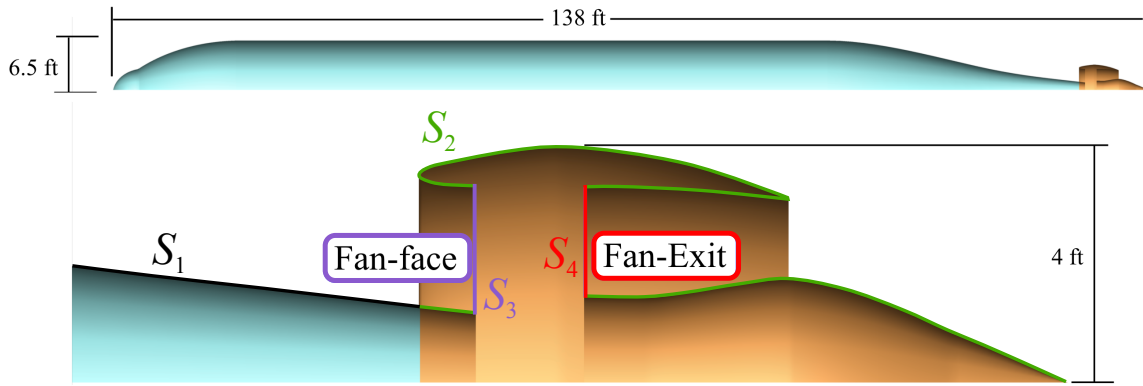


Figure 5.1: BLI configuration and boundary conditions: viscous walls (S_1, S_2), outflow face (S_3), and inflow face (S_4)

The podded configuration shown in Figure 5.2 is identical to the one used in Chapter 4. In this chapter the podded model is used not only as a reference to measure BLI performance against, but also as a means of predicting power usage for the under-wing propulsors as well.

Similarly to Chapter 4, for both configurations the geometry is parameterized via free form deformation (FFD) to modify the surface mesh [51]. The surface changes are propagated to the volume grid using an inverse distance weighted method of mesh deformation[99].

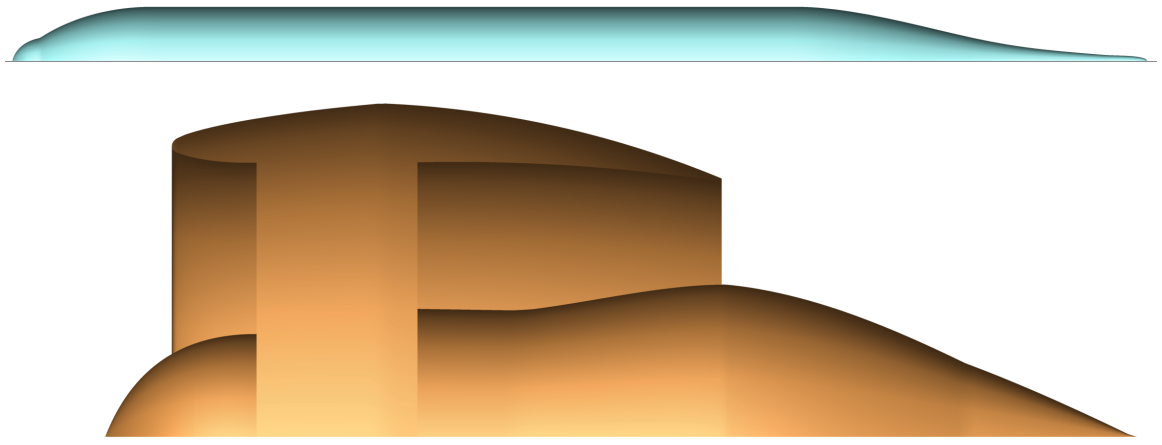


Figure 5.2: The podded configuration serves as a reference and models fuselage (top) and propulsor (bottom) separately.

However, the details of the FFD itself changed in this chapter. There are now many more control points on the FFD, including some new ones on the fuselage compared to Chapter 4. Also, fine shape variables have been introduced for the nacelle and nozzle plug sections that were not there in the previous chapter either. The majority of the fuselage shape remains fixed, but the shape of the aft taper section and of the nacelle and plug are allowed to vary. The FFD boxes and associated control points are shown in Figure 5.3 for the BLI configuration. The podded configuration uses the same FFD on the propulsor section (shown in orange) but keeps the clean fuselage unchanged.

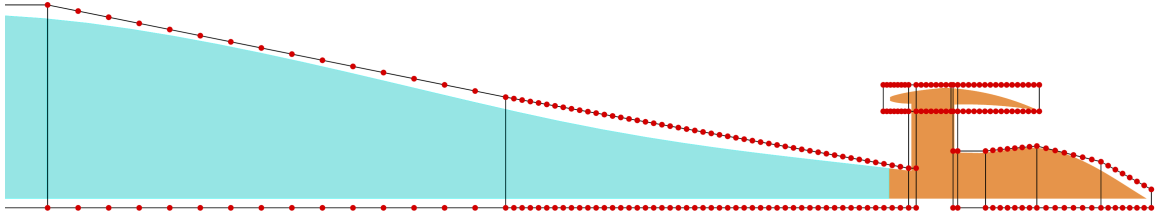


Figure 5.3: The shape of the BLI configuration is enveloped in FFD boxes (black lines) and parameterized using FFD control points.

One of the major challenges when modeling BLI propulsion systems is establishing a consistent scheme for bookkeeping all of the forces on the combined aeropropulsive system when some of the forces are computed by the aerodynamic analysis and other forces are computed by the propulsion analysis. As in Chapter 4, I avoid this problem by performing

all the force accounting directly within the aerodynamic analysis via Equation (5.1).

$$C_{F_x} = \frac{2}{\rho_\infty V_\infty^2 A_{\text{ref}}} \left(\iint_{S_1} (p\hat{\mathbf{n}} + \mathbf{f}_{\text{visc}}) \cdot \hat{\mathbf{x}} dS + \iint_{S_2} (p\hat{\mathbf{n}} + \mathbf{f}_{\text{visc}}) \cdot \hat{\mathbf{x}} dS + \iint_{S_3} (p\hat{\mathbf{n}} \cdot \hat{\mathbf{x}} + \rho_3 u_3^2) dS + \iint_{S_4} (p\hat{\mathbf{n}} \cdot \hat{\mathbf{x}} - \rho_4 u_4^2) dS \right), \quad (5.1)$$

Equation (5.1) accounts for all of the viscous, pressure, and momentum flux forces on the entire body. Each contribution is color coded to match the associated boundary condition in Figure 5.1. Note that the sign of C_{F_x} is significant: A positive value indicates a net decelerating force (i.e., drag) on the body, and a negative value indicates a net accelerating force (i.e., thrust). The reference values used for Equation (5.1) are given in Table 5.1.

Table 5.1: Reference values used in the force nondimensionalization

ρ_∞	0.0008 slug/ft ³
V_∞	707.3 ft/sec
A_{ref}	1,400 ft ²

5.1.2 Propulsion Model

The propulsor model used in this chapter is very similar to the one used in Chapter 4. Both models share the same set of pyCycle elements, but they differ because the one used here lacks its own internal Newton solver to converge mass flow rate. Instead of using an internal solver in this design optimization, I chose to use an IDF formulation where the optimizer converges the residual function to respect a given shaft power. The reason for choosing IDF for the optimization work was discussed in detail in Chapter 2.1.

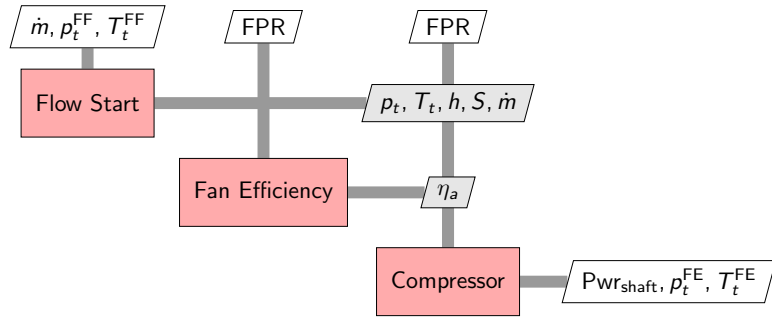


Figure 5.4: The propulsor fan model consists of three sub-models; It computes the shaft power and fan exit conditions given the FPR, mass flow, and fan face conditions.

The aft propulsor fan is modeled with three separate parts, as shown in the XDSM [1] diagram in Figure 5.4. The flow-start computes the enthalpy (h) and entropy (s) given mass flow rate (\dot{m}), mass-averaged total temperature (T_t^{FF}), and mass-averaged total pressure (p_t^{FF}) from the fan face (S_3 in Figure 5.1). The fan pressure ratio (FPR) is also given as an input and will be one of the design variables in the optimization. The model outputs fan exit total temperature (T_t^{FE}), total pressure (p_t^{FF}), and the required shaft power to handle the given mass flow rate. The fan efficiency is computed using a linear correlation with FPR, which is the same relationship used in Chapter 4 and sourced from the same reference material [23, 94].

$$\eta_a = 1.066 - 0.0866 \cdot \text{FPR}. \quad (5.2)$$

Equation 5.2 captures the change in fan performance as the design fan pressure ratio changes, but it does not account for the impact of inlet distortion caused by the boundary layer ingestion.

5.1.3 Optimization Problem

To capture the aeropropulsive interactions, I built a fully coupled model of the fuselage and BLI propulsor by combining the aerodynamic and propulsion models in the OpenMDAO framework. A sequential quadratic programming (SQP) optimizer implemented in the SNOPT [100] package was used to optimize the coupled model in order to perform the design studies. The aeropropulsive coupling is implemented using an IDF optimization architecture [101], which uses constraints imposed on the final solution to enforce multidisciplinary compatibility. There are four IDF constraints, represented by $\mathcal{R}(\text{Pwr})$ and $\mathcal{R}(\text{B.C.})$ in Fig. 6.9 that force the target values—any value with the $(\cdot)^*$ superscript—to match the values computed using the actual models. We use the same optimization problem formulation for both the BLI and the podded configurations. The grids for the aerodynamic analysis are different between the two configurations, as shown in Figure 5.1 (BLI configuration) and Figure 5.2 (podded configuration).

The goal of the optimization is to minimize $\text{Pwr}_{\text{shaft}}$ with respect to FPR, static pressure at the fan face (p_s^{FF}), and 311 aerodynamic shape variables ($X_{\text{nacelle}}, X_{\text{shape}}$), subject to a prescribed net force ($C_{F_x}^*$) on the fuselage. The FPR is allowed to vary from 1.2 to 1.5. These bounds are applied to keep the fan designs within a reasonable range. The shape variables have no upper bound but are given lower bounds based on the limits of the mesh deformation algorithm. Specifically, the lower limits prevent the nozzle plug from being forced to shrink below a minimum radius.

The optimization problem formulation is detailed in Table 5.2. In addition to the design

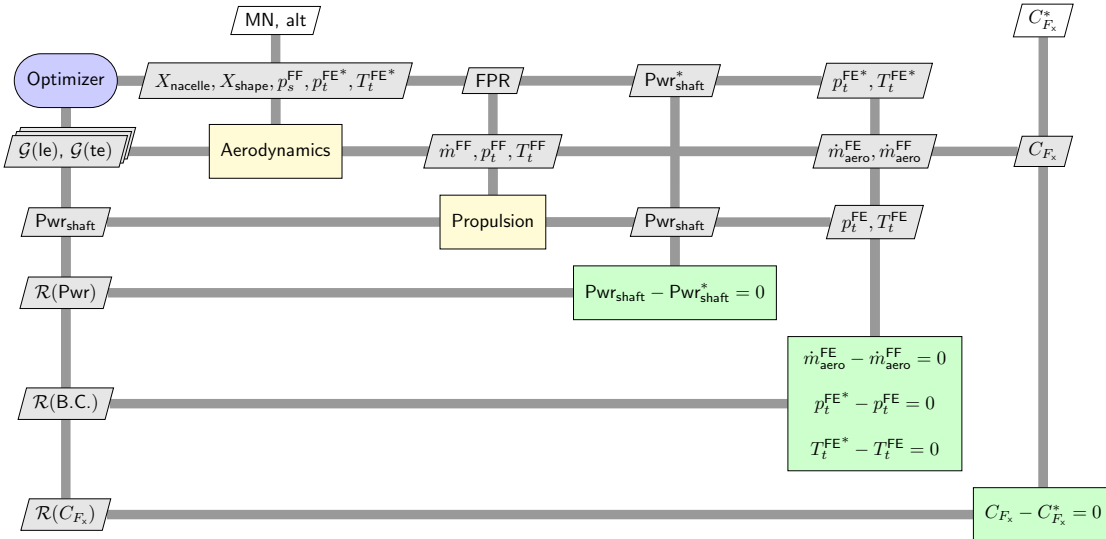


Figure 5.5: XDSM diagram of the full optimization problem formulation, including the compatibility constraints that enforce the aeropropulsive coupling.

variables mentioned above, there are three additional design variables listed in Table 5.2: P_{shaft}^* , $p_t^{\text{FE}*}$, and $T_t^{\text{FE}*}$); however, these are not true design degrees of freedom because they are used by the optimizer to satisfy the IDF constraints. Two sets of geometric constraints (\mathcal{G}_{LE} and \mathcal{G}_{TE}) are imposed on the leading and trailing edge of the propulsor nacelle profile to ensure that the optimizer does not make them unrealistically thin.

In Fig. 6.9, the C_{F_x} constraint appears similar to the four IDF constraints, except that the target value ($C_{F_x}^*$) is given as a parameter external to the optimization. This constraint is not needed for multidisciplinary compatibility, but instead it is used to ensure a well posed optimization problem. This constraint is needed because the relative size of the BLI and under-wing propulsors is not known a priori. Depending on what the optimal sizing turns out to be, the net force on the fuselage could range from a net drag to a net thrust.

In the first phase of this work, I performed a set of optimizations for a range of $C_{F_x}^*$ values. In the second phase, using the data from these optimizations, I found the most efficient size for the BLI propulsor.

5.1.4 Aeropropulsive Optimization Results

Two sets of 13 optimizations were performed for different net thrust constraint values, ranging from $C_{F_x}^* = 0.0025$ to $C_{F_x}^* = -0.156$, corresponding to 3000 N net drag and 17 000 N net thrust, respectively. One set of optimizations was run on the BLI configuration, and a second set was run on the podded configuration to serve as a reference. All of the optimized

Table 5.2: Optimization problem for the fuselage aeropropulsive design.

	Variable/Function	Description	Quantity
minimize	P_{shaft}	Propulsor shaft power	
with respect to	FPR	Fan pressure ratio	1
	X_{nacelle}	Global nacelle shape variables	3
	X_{shape}	Nacelle and fuselage local shape variables	308
	p_s^{FF}	Static pressure at the fan face	1
	P_{shaft}^*	Propulsor shaft power target	1
	p_t^{FE*}	Total pressure target at the fan exit	1
	T_t^{FE*}	Total temperature target at the fan exit	1
	Total		316
subject to	$C_{F_x}^{\text{net}} = C_{F_x}^{\text{net}*}$	Specified net force on full body	1
	$\mathcal{R}_m = 0$	Mass residual	1
	$\mathcal{R}_P = 0$	Propulsor shaft power residual	1
	$\mathcal{R}_{p_t^{FE}} = 0$	Total pressure residual	1
	$\mathcal{R}_{T_t^{FE}} = 0$	Total temperature residual	1
	$0.9 < \mathcal{G}_{\text{LE}} < 2$	Leading edge thickness	3
	$0.9 < \mathcal{G}_{\text{TE}} < 2$	Trailing edge thickness	3
	Total		11

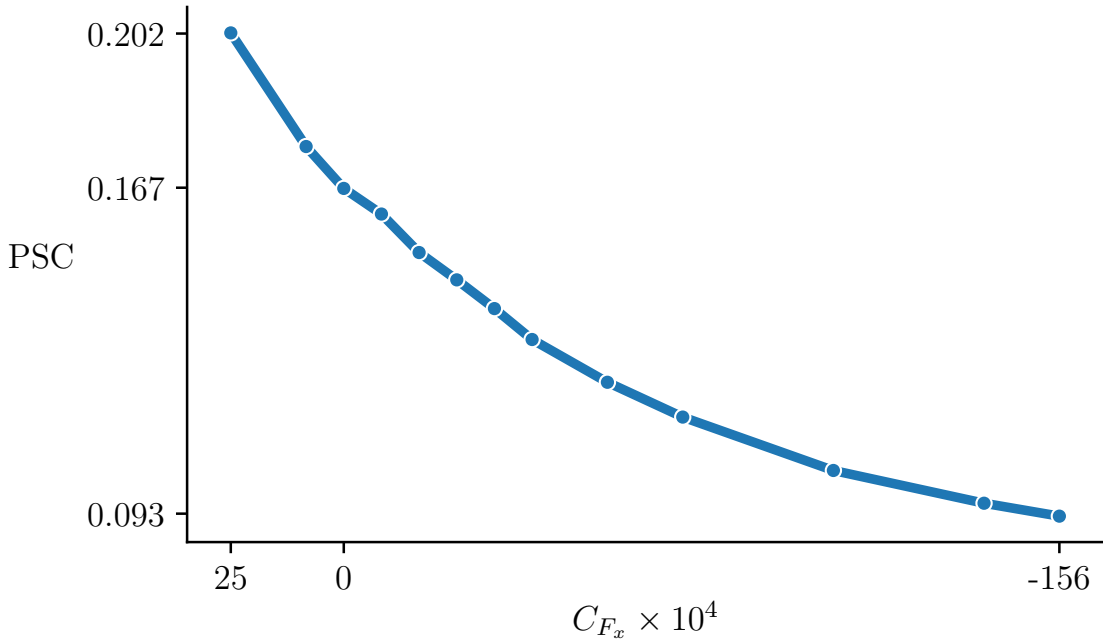


Figure 5.6: Power saving coefficient vs C_{F_x} shows that smaller BLI propulsors (small positive C_{F_x}) offer greater power savings than larger ones.

configurations ended up with a FPR of 1.2, which was the lower bound for that design variable. The PSC, defined in Equation (1.1), was computed for each net thrust coefficient value by using the shaft power for the optimized podded configuration as the reference. Figure 5.6 shows that the PSC takes a maximum value of 0.202 for $C_{F_x} = 0.0025$ and that the PSC decreases smoothly to 0.093 for $C_{F_x} = -0.156$. At $C_{F_x} = 0.0025$, there is a slight net decelerating force on the fuselage, which corresponds to a small BLI propulsor. Conversely, $C_{F_x} = -0.156$ yields a net accelerating force on the fuselage, which corresponds to a larger BLI propulsor. Note that the results in Fig. 5.6 are computed only on the fuselage and BLI propulsor. In the next section, we extend this problem to estimate the sizing for the whole propulsion system, including the under-wing propulsors.

5.2 BLI Propulsor Sizing Analysis

5.2.1 Podded Propulsor Performance

Although traditional thrust and drag accounting is not valid for the BLI configuration, the podded configuration can still be examined using a force-based metric because in that case, the propulsor and fuselage are two separate items; thus, the propulsor thrust ($C_{F_{\text{pod}}}$) is a well

defined quantity, computed using Equation (5.1) applied to the podded propulsor surfaces (the orange surfaces in Figure 5.2). Figure 5.7 plots the data for each of the optimized podded propulsors normalized by counts of net force on the propulsor. Given that FPR= 1.2 for all of the optimized configurations, from a pure thermodynamic cycle analysis perspective, one would expect a flat line in Figure 5.7; however, since the thrust data computed here includes the nacelle drag it represents installed thrust and some dependence on nacelle diameter is expected.

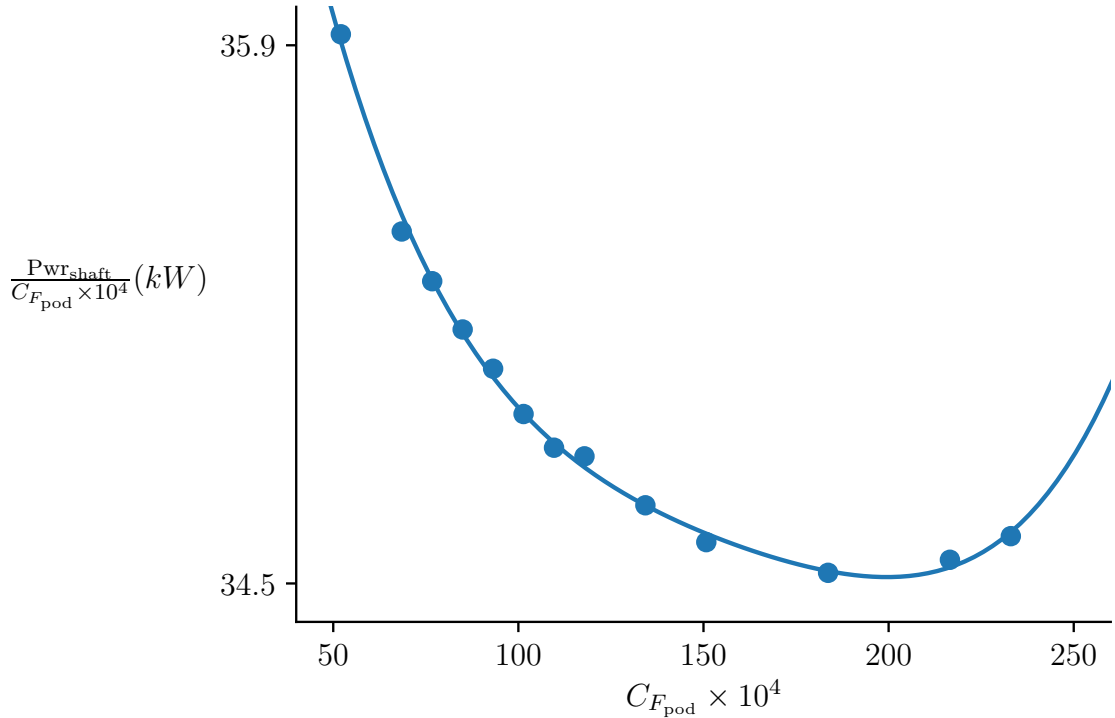


Figure 5.7: $P_{\text{shaft}}/C_{F_{\text{pod}}}$ data (circles) and 4th order polynomial fit (solid line) for the podded propulsor.

The solid line in Fig. 5.7 is a 4th order polynomial fit of the data, given by

$$\frac{P_{\text{shaft}}}{C_{F_{\text{pod}}} \times 10^4} = 38.89 - 0.00867x + 7.474 \times 10^{-4}x^2 - 3.013 \times 10^{-6}x^3 + 4.729 \times 10^{-9}x^4. \quad (5.3)$$

This equation can be used to predict the required shaft power for an underwing engine given a specified $C_{F_{\text{pod}}}$. For any podded engine thrust value, we should stay within the bounds of the fitted data to avoid extrapolation issues. One caveat with this equation is that it was fit based on results from a single under-wing propulsor, so when applying it to compute power requirements for the whole aircraft, it is important to consider that there are two engines and hence each one only produces half the thrust and hence half the force coefficient.

5.2.2 Propulsion System Sizing Method

Equation (5.1) computes only the force coefficient on the fuselage component of the aircraft. To size the propulsion system, we must consider additional drag contributions from the lifting surfaces—wings, vertical tail, and horizontal tail. This lifting surface drag is computed using the empirical drag methods in the FLOPS tool [102], using appropriate inputs for the STARC-ABL configuration. In this case, FLOPS predicts a lifting surface drag of 216 counts ($C_D = 0.0216$).

At a steady cruise condition, the aircraft should remain at a constant speed, meaning that the net force is zero. With the assumed C_D and any prescribed value of C_{F_x} , it is possible to compute the required additional force coefficient from the under-wing propulsors that satisfy this zero-net-force constraint as follows

$$C_{F_{\text{pod}}} = -(C_D + C_{F_x}), \quad (5.4)$$

where, as previously mentioned, the sign of the force coefficients is significant: Positive values result in deceleration and negative impart acceleration.

By combining Equations (5.3) and (5.4), the required shaft power from the under-wing propulsors can be computed. To provide a reference, we use the net drag on the clean fuselage from the podded configuration and assume that 100% of the thrust—and hence all of the required shaft power—is generated by the under-wing engines. For each optimized BLI fuselage design, the C_{F_x} is known because it is prescribed as an optimization constraint; therefore, the required additional shaft power from the under-wing propulsors can be computed using Equation 5.4 for each BLI configuration. The total shaft power required by all propulsors for the steady cruise condition can then be computed as

$$\text{Pwr}_{\text{tot}} = \frac{\text{Pwr}_{\text{BLI}}}{\eta_{\text{trans}}} + \text{Pwr}_{\text{pod}}, \quad (5.5)$$

where the combined transmission efficiency (η_{trans}) is accounted for. η_{trans} is the efficiency of the system that generates the power from the under-wing engines and transmits it to the aft fuselage to power the electric drive motor. Three values for η_{trans} are considered: 0.9, 0.95, and 0.98. An η_{trans} of 0.9 represents the expected transmission efficiency for a traditional AC/DC power system [27]. The values for η_{trans} of 0.95 and 0.98 are assumed for future performance of systems based on the use of superconducting motors, generators, and power lines. The percentage reduction in power consumption at cruise for a fuselage with a particular C_{F_x} and assumed η_{trans} can then be computed by taking the ratio of the power required for the BLI configuration to the reference power required for the configuration

without BLI (the podded configuration).

5.2.3 Propulsion Sizing Results

Figure 5.8 shows the combined results from the analysis described by Equations (5.3), (5.4), and (5.5) plotted versus the power split between the aft BLI propulsor and the under-wing propulsors. The results show that the optimal propulsor sizing depends strongly on the assumed value for η_{trans} . Assuming current power transmission technology levels (i.e., $\eta_{trans} = 0.9$), BLI yields a 1% reduction in net shaft power required at cruise, and the aft propulsor uses 15.3% of the total power. This small improvement in overall performance is significantly lower than the 9% to 20% improvement in the standalone BLI propulsor seen in Figure 5.6. This makes it clear that η_{trans} is having a massive effect on overall system performance. Losing 10% of the power by converting mechanical energy to electrical and back to mechanical is driving the overall system to a very small BLI propulsor, which is limiting the overall effect on overall fuel burn.

As η_{trans} improves, the overall results improve as well. For $\eta_{trans} = 0.95$, PSC values of 2% to 2.5% are achieved across the whole range of power splits. These results are notable for the large flat plateau to the right of the optimum power split of 34.3%, which implies that there is a large amount of design freedom in terms of aft propulsor sizing. In the best case scenario, $\eta_{trans} = 0.98$, the best PSC occurs at the largest power split analyzed. At very high η_{trans} , this result is expected because the best performance would come from making as much thrust from the BLI propulsor as possible.

I must emphasize that this sizing analysis is done from a purely thermodynamic perspective. The optimum power split between the BLI and under-wing propulsors is estimated considering only the aeropropulsive effects and the overall power usage of the system. Furthermore, only a single cruise condition is examined. A complete aircraft design process would need to consider other factors, including the overall mass of the turboelectric propulsion system with respect to BLI propulsor size, multiple flight conditions, thermal performance for the power transmission system, tail rotation angle at takeoff, and center of gravity movement. Additionally, the axisymmetric analysis done here does not account for impact of the wing and tail on the inflow conditions of the BLI propulsor. Despite missing these elements in the analysis, these results do provide a conclusive picture of how the propulsion system performance is affected by the inclusion of a BLI propulsor, and how the optimum sizing of that propulsion system varies with changes in electric power transmission efficiency.

5.2.4 Qualitative Analysis of the Optimized Configurations

Figure 5.9 compares the optimal power split designs for $\eta_{\text{trans}} = (0.9, 0.95, 0.98)$. The most notable change between the three designs is the size of the aft propulsor, which grows significantly as the assumed transmission efficiency improves. The outermost streamline of the flow entering the propulsor is shown as a black line on each design. For $\eta_{\text{trans}} = 0.98$, the propulsor is very large and is clearly ingesting non-boundary layer flow. Closer examination of the nacelle and nozzle plug shapes between the three cases shows significant differences in shape between each case. The nozzle plug shows the greatest variation in shape, with a nearly flat profile for the smallest propulsor and the development of the ramp shape to create a stronger nozzle throat as the propulsor grows. The nacelle also changes shape, though more subtly. As the nacelle moves up into the faster moving flow, it takes on a slightly larger tilt to better align with the local flow and becomes slightly thicker. These shape variations highlight the importance of using an optimization-based design approach for this coupled problem. The aerodynamic analysis is sensitive to these small changes in the shape, and hence the overall trends that are reported are sensitive to them as well, and an optimizer is required to make sure each design considered in the parametric sweep is

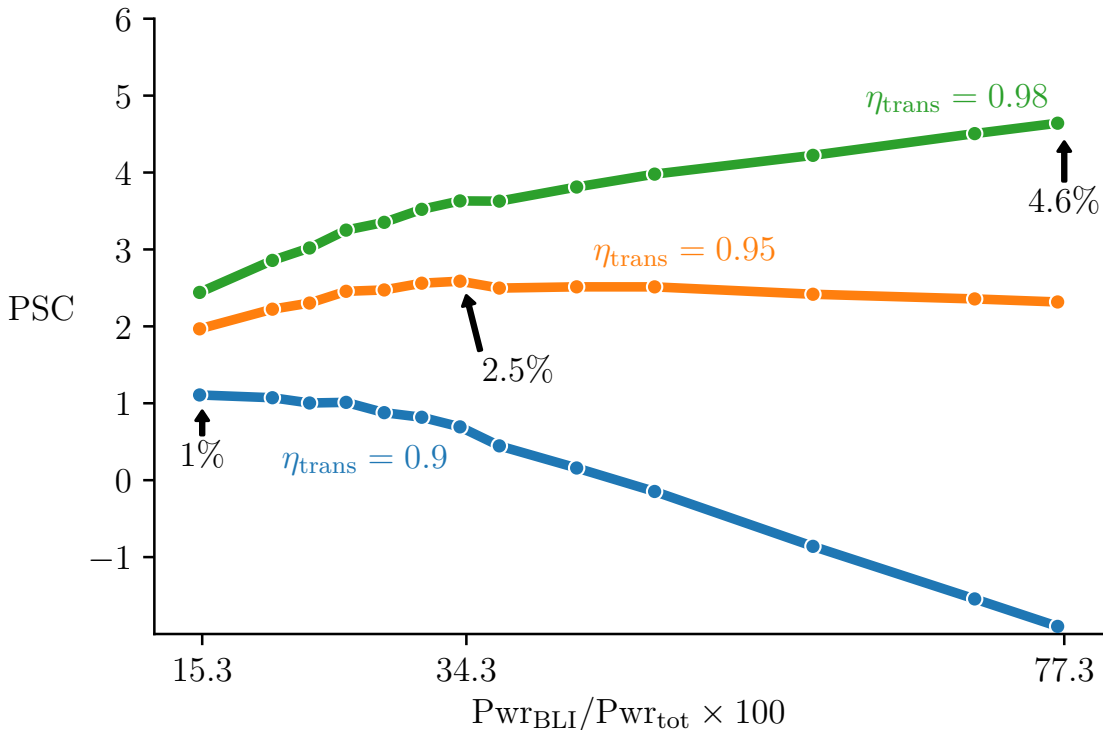


Figure 5.8: Overall aircraft PSC at cruise vs the fraction of shaft power used for BLI at different assumed values of transmission efficiency, η_{trans} .

performing as well as it can.

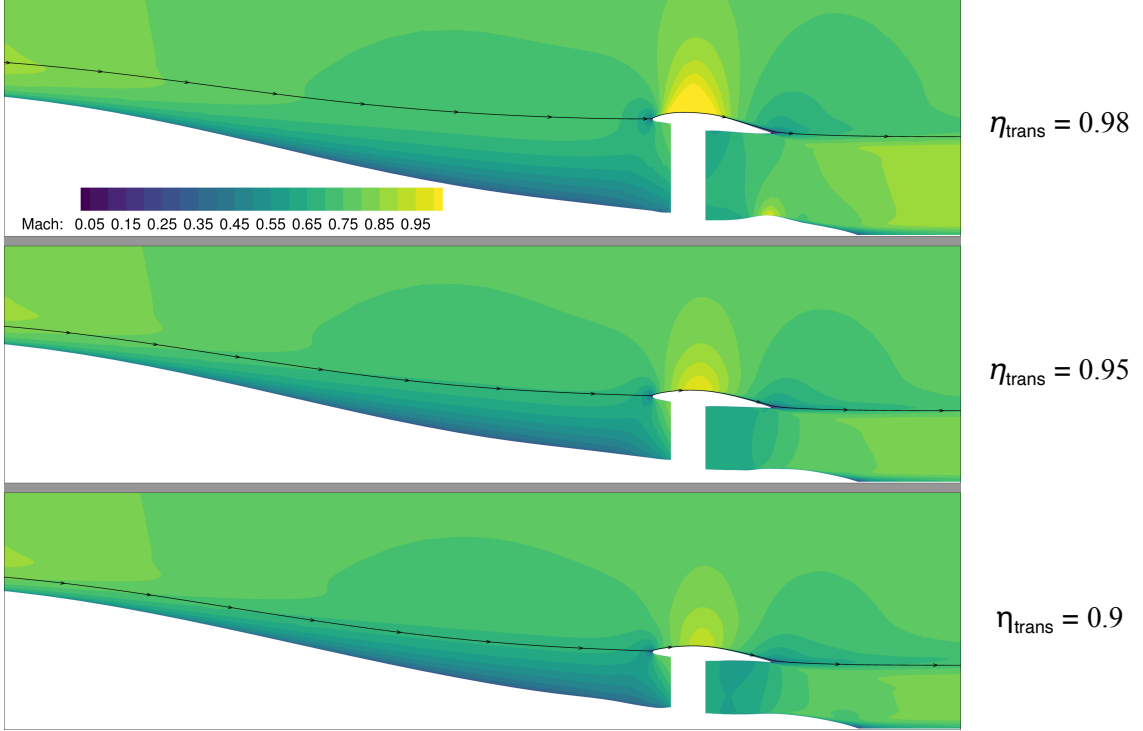


Figure 5.9: Best-performing designs for three assumed values of η_{trans} . Increased transmission efficiency drives the design to larger BLI propulsors relative to the under-wing engines.

The variation in the Mach contours between each design in Fig. 5.9 is worth discussing. There are two places where these variations are most significant and obvious. The flow over the top of the nacelle changes dramatically as the propulsor grows larger. For $\eta_{\text{trans}} = 0.9$, the nacelle is effectively in the shadow of the fuselage and the nacelle wall sees very low speed flow. As the nacelle grows bigger, the flow becomes faster, and the high speed region over the top of it grows larger. This variation in flow results in a variation in the amount of viscous drag on the nacelle for the BLI case that is greater than was observed for the podded configuration in clean flow.

The second flow feature that displays variation with changing propulsor is the boundary layer profile near the inlet of the propulsor. The variation in boundary layer profiles and surface pressure distributions on the aft fuselage as a function of propulsor design were discussed in greater detail in Chapter 4.2.3, but that work performed only aeropropulsive analysis for a fixed nacelle shape. Those results indicated that, although the flow field was changed with a variation in the inlet height, the trends were sensitive to p_s^{FF} , which I acknowledged could change in a final optimized result if nacelle shape was allowed to change. Figure 5.10 examines the boundary layer profiles—defined using the total pressure

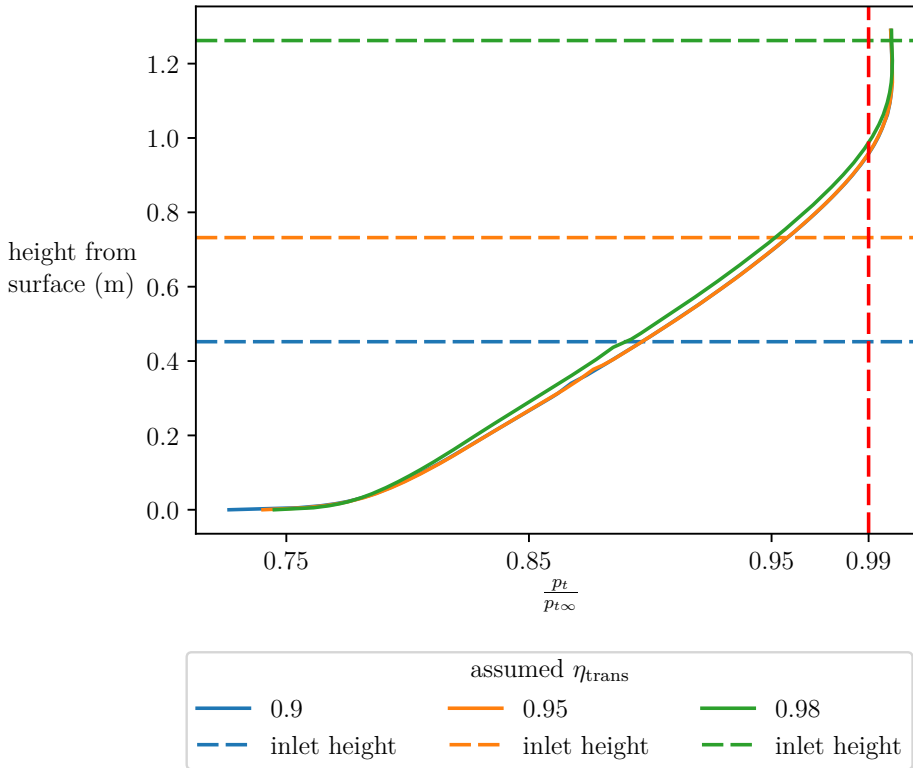


Figure 5.10: Boundary layer profiles (measured via $p_t/p_{t\infty}$) for the best designs found for each assumed value of η_{trans} . The horizontal dashed lines indicate the height of the inlet lip for each design.

ratio with freestream—half a meter ahead of the inlet lip for the best design found for each assumed value of η_{trans} . Total pressure ratio is used to define the boundary layer, rather than the more traditional velocity metric, because the flow around the tailcone is undergoing inviscid diffusion, which makes a comparison with the freestream velocity less accurate as a means of defining the boundary layer. The edge of the boundary layer is denoted by the vertical red dashed line at $p_t/p_{t\infty} = 0.99$. In Figure 5.10, the largest propulsor design (corresponding to $\eta_{\text{trans}} = 0.98$) shows a pronounced difference in boundary layer profile compared to the two smaller designs. The larger propulsor applies a greater backpressure to the flow, which causes the boundary layer to grow thicker. We can also clearly see from the horizontal dashed lines that denote the inlet height for each design that the largest propulsor ingests a significant amount of flow from outside the boundary layer. The two smaller propulsors, however, ingest only boundary layer flow. Although the profiles for the two smaller propulsors look very similar, there is a small difference very close to the fuselage where variations in the surface pressure distribution become apparent. Overall, these results show less variation in the boundary layer profile than what is shown in Chapter 4, but it

is clear that the aeropropulsive coupling still has an impact on the boundary layer near the propulsor.

5.3 Summary

A series of design optimizations of a simplified version of NASA's STARC-ABL aircraft configuration were performed using a fully coupled aeropropulsive model. The goal of the STARC-ABL configuration is to utilize an aft-mounted, electrically-driven BLI propulsor to achieve a significant reduction in mission fuel burn. The aircraft configuration was simplified by representing the fuselage and aft-mounted propulsor as an axisymmetric body. The aerodynamic model of the fuselage and propulsor combination was based on a RANS CFD model, and this was coupled with a 1-D thermodynamic model of the propulsor fan via outflow and inflow boundary conditions that modeled the fan face and fan exit, respectively. The coupling was formulated using an IDF formulation so that it was enforced as part of the optimization. The entire model was constructed and optimized using gradient-based optimization with analytic derivatives in the OpenMDAO framework. The shaft power was minimized, with respect to both aerodynamic shape variables and propulsion design variables while enforcing a prescribed constraint on the net force of the fuselage and propulsor combination. A series of optimizations was performed with different values for the net force constraint for both a BLI and a reference podded configuration for the aft-mounted propulsor.

The performance of the BLI propulsor was measured by comparing the required power of the optimized BLI configuration to that of the optimized podded configuration for the same net force on the overall body (i.e., computing the PSC). This comparison showed that smaller propulsors achieved the best PSC. For small values of net drag on the fuselage, the BLI configuration had a PSC of 0.202. A PSC value of .202, or a 20.2% reduction in required shaft power, seemingly represents a significant potential savings, however this point also corresponds to the smallest BLI propulsor design. The BLI propulsors were found to get progressively less efficient as they grew in size, reaching a minimum power savings coefficient of 0.093 for the largest propulsor.

The variation in PSC as a function of propulsor sizing is significant because it means that the designs with the highest PSC values do not necessarily translate to the best overall design of the propulsion system because the STARC-ABL only gets part of its thrust from the aft-mounted BLI propulsor. Despite being significantly more efficient, the smaller BLI propulsors produce a smaller portion of the overall thrust, and hence can only reduce the energy usage of the whole propulsion system by a small amount.

In order to identify the best overall design for the whole propulsion system, I performed a propulsion sizing analysis by examining the combined power requirements of both the BLI propulsor, accounting for the effect of power transmission efficiency, and under-wing engines to provide a metric of overall efficiency. The sizing analysis indicated that, assuming current electrical power transmission technology, 1% power savings is achieved when 15.3% of the aircraft power is transmitted to the aft propulsor. Using a moderately advanced power transmission system with an efficiency of 95%, the optimum PSC reaches .025. As an extremely high power transmission efficiency of 98%, the best performance is achieved by making as much thrust as possible from the BLI propulsor.

The aeropropulsive analysis and design performed for this work demonstrates the importance of using fully coupled models to predict the performance of physically coupled systems. The standalone BLI propulsor analysis shows a large potential efficiency gain from this aeropropulsive concept. The challenge is to integrate BLI technology into an aircraft configuration to make the most of it. Analysis of the full propulsion system for the STARC-ABL configuration shows that propulsion-airframe integration will have a large impact on the overall performance. There are two key coupling effects that each affect how the full propulsion system performs. First, the aeropropulsive effects on the BLI propulsor are shown to vary in strength as a function of propulsor sizing which, contributes to a nonlinear variation in BLI benefit. Second, the impact of electrical power transmission efficiency is shown to have a first order effect on the relative sizing of the under-wing vs BLI propulsors. Although they can be described separately, in reality these two coupling effects cannot be considered in isolation of each other in the context of aeropropulsive design. As one varies the power transmission efficiency, the propulsion system must be redesigned to maximize benefits and the relative sizing of the under-wing and BLI propulsors can vary significantly.

CHAPTER 6

Distortion constrained optimization of a 3-D BLI propulsor

In Chapter 4 I demonstrated the importance of using a fully coupled aeropropulsive model — versus an uncoupled model — to predict BLI performance because the coupled model predicts different propulsor inlet conditions and a different surface pressure distribution on the fuselage compared to an uncoupled model. That analysis was performed on a simplified 2-D configuration based on of NASA’s STARC-ABL aircraft. Chapter 5 further investigated that simplified configuration with a design study focused on the question of relative propulsor sizing Those results showed that the BLI system offered between 1% and 4.6% reduction in total power required for cruise, depending on the assumption made about the power transmission efficiency (η_{trans}) of the turboelectric system. The design study further demonstrated the importance of using a fully coupled aeropropulsive model, and established η_{trans} as a key design assumption for the overall design and performance of the aircraft.

While the simplified 2-D axisymmetric models were sufficient to establish the fundamental trends and perform basic sizing, recent aerodynamic analysis of the STARC-ABL configuration has clearly shown that three-dimensional aerodynamic models are necessary in order to accurately predict the airflow at the aft fuselage. Kenway an Kiris examined the inlet distortion for the BLI propulsor on the aft-fuselage of the full 3-D STARC-ABL configuration [39]. Their work identified two causes of non-axisymmetric flow at the propulsor fan face: the non-axisymmetric fuselage and the wing downwash. The results they presented showed that the fuselage geometry causes some minor asymmetry, but the wing downwash contributed much more significantly to the distortion. Using aerodynamic shape optimization they were able to reduce distortion to less than 2%. Beyond the conclusions about distortion, their results clearly demonstrate the importance of using 3-D models of the airframe, including the wings, for the aerodynamic analysis. In that work the nacelle design variables only allowed for shape changes at the front section of the nacelle. Signif-

ificant changes to the nacelle diameter, the shape of the nozzle plug, or to the shape at the aft of the nacelle were not part of the design space. The somewhat limited design freedom present was sufficient for the distortion minimization objective function they used, but was not sufficient to consider large variations in the propulsor sizing.

In this chapter I present aeropropulsive design optimization of the BLI propulsor, at a cruise condition of Mach 0.785 and altitude of 37000 ft. The optimization is performed using the same optimizer from Chapter 5, SNOPT [100]. The coupled model was constructed in the OpenMDAO framework with a 3-D RANS CFD aerodynamic analysis coupled to a 1-D thermodynamic cycle model of the aft mounted propulsor. The aeropropulsive coupling is implemented in a significantly different manner than was done in for the optimization of the 2-D configuration, from the previous chapter. For the 2-D case inflow and outflow boundary conditions were used to create a pair of interface planes between the aerodynamic model and propulsion model. In this chapter, a different approach is taken, where different aspects of the propulsion system are modeled separately in the aerodynamics and propulsion models. This splitting of the physical system into two different disciplinary models is done in order to allow the usage of a more detailed fan model, based on a body-force model[97, 103], to enable the measurement of distortion.

The optimization problem is set up to minimize the shaft power required to generate a given net force on the entire aircraft (fuselage, wings, tail, propulsor). At a steady cruise condition the net force on the entire aircraft must be zero, but in this work the under-wing propulsors are not modeled so the net force on the body is non-zero. Distortion is computed using the method developed by Kenway and Kiris [39]. The optimization is run for a series of different propulsor sizes to study the impact of propulsor sizing on BLI performance in the presence of a constraint on inlet distortion.

6.1 Aerodynamic Model

6.1.1 Aircraft Geometry

The geometry shown in Figure 6.1 is modeled with the OpenVSP geometry engine[104], which outputs a surface discretization for each body in the mesh individually. Then a rigid links interpolation scheme is used to connect the OpenVSP surface discretization to the surface discretization of the CFD mesh. Changes in the surface mesh are propagated to the volume mesh via an inverse distance weighting implementation of mesh-morphing following the formulation of Luke et al.[99, 105, 73]

Figure 6.2 illustrates the shape parameterization for the aft-fuselage and BLI propul-

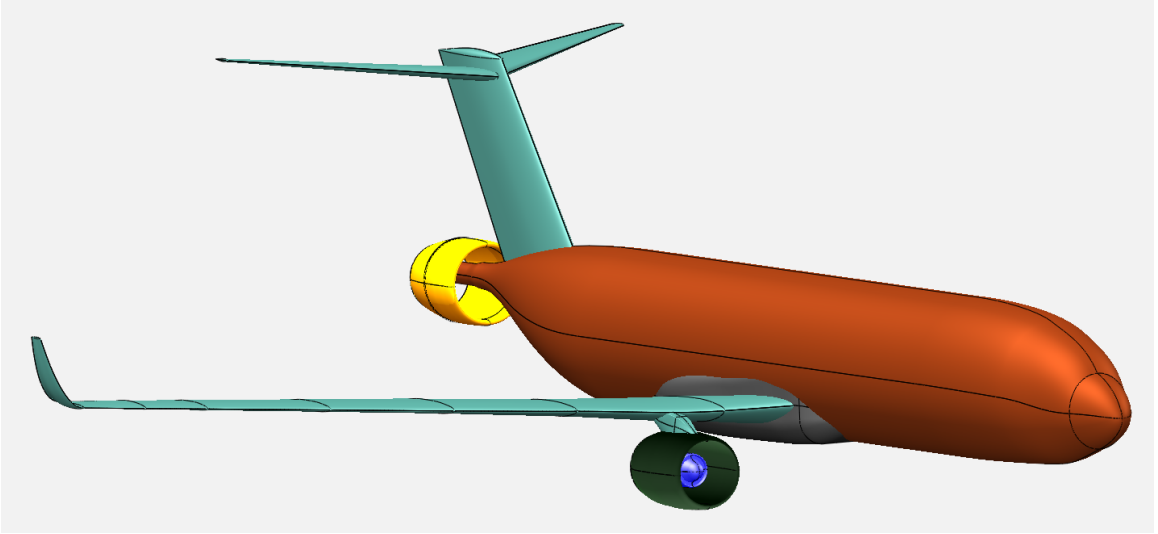


Figure 6.1: openVSP model of the STARC-ABL aircraft geometry including the vertical tail and aft mounted BLI propulsor.

sors. OpenVSP defines surfaces using Beizer curves which for the fuselage and nacelle are parameterized using cross sections to define surface radii and then local tangent strength and angle to define surface curvature. The red cross sections indicate elliptical shapes, with independent control over height and width. The yellow cross sections indicate circular shapes, with only a single diameter variable. In addition to separate control over each cross section, there is also a global design variable for the nacelle diameter which scales all the cross sections together, which is noted in black in Figure 6.2. OpenVSP enables a fairly flexible surface parameterization with a relatively small number of design variables. In all 25 shape variables are used to define the surface of the aft-fuselage, nacelle, and nozzle plug.

6.1.2 RANS Solver: ADflow

The aerodynamic analysis is a 3-D RANS CFD run with ADflow code, using overset meshes. The overset meshes were generated using the Chimera Grid Tools and an implicit hole cutting scheme[71, 105]. The mesh, shown in Figure 6.3, is composed of 8 different sub-meshes for a total of 6 million cells.

The aircraft wing was optimized for minimum drag in prior work, using a 5 point multipoint stencil around the cruise condition [106, 107, 108]. The wing geometry was held fixed at this previously optimized design for all studies done in this work. The BLI propulsor is modeled using a body-force zone[103] that imparts the effect of the fan on the flow without needing to model the fan itself. The effect of the body-force zone is highlighted in

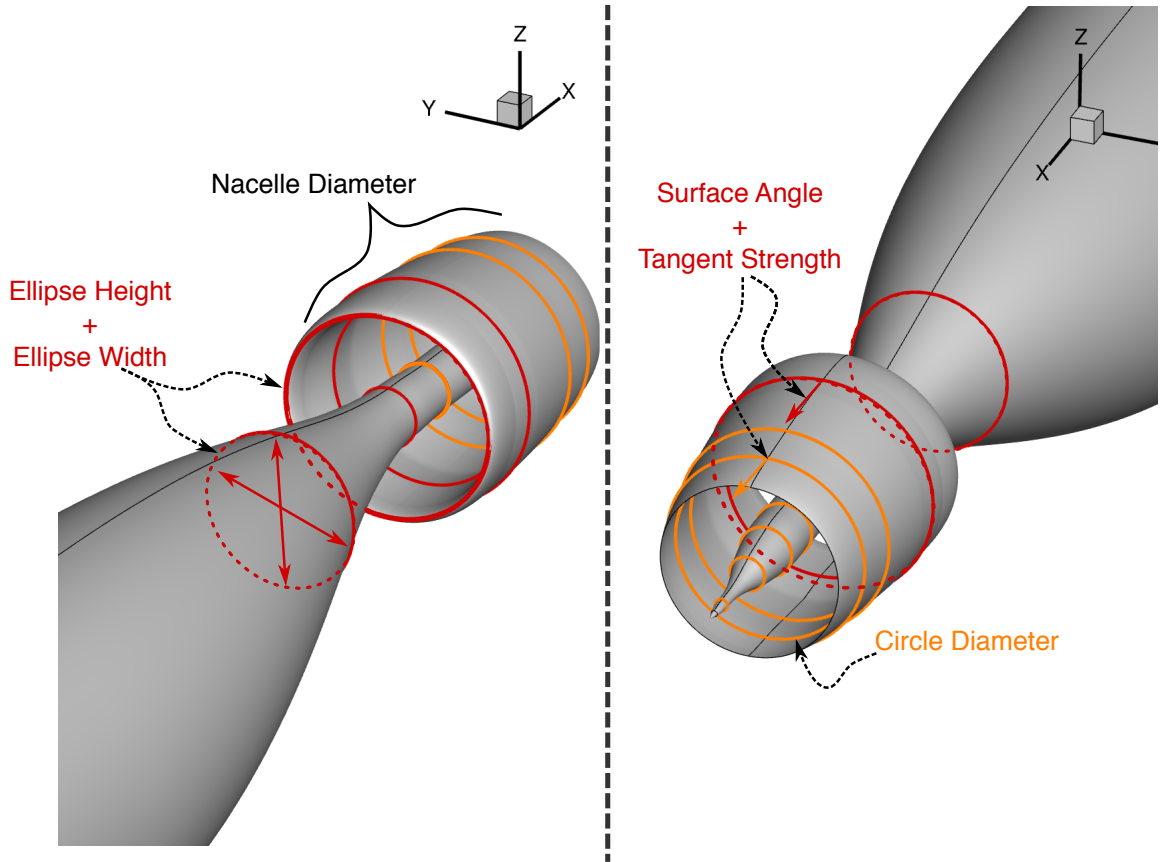


Figure 6.2: Diagram of the shape parameterization for the aft fuselage and BLI propulsor. The red curves represent elliptical cross sections and the yellow curves represent circular cross sections. Each cross section on the BLI nacelle also has tangent strength and angle design variables which control the surface bezier curves.

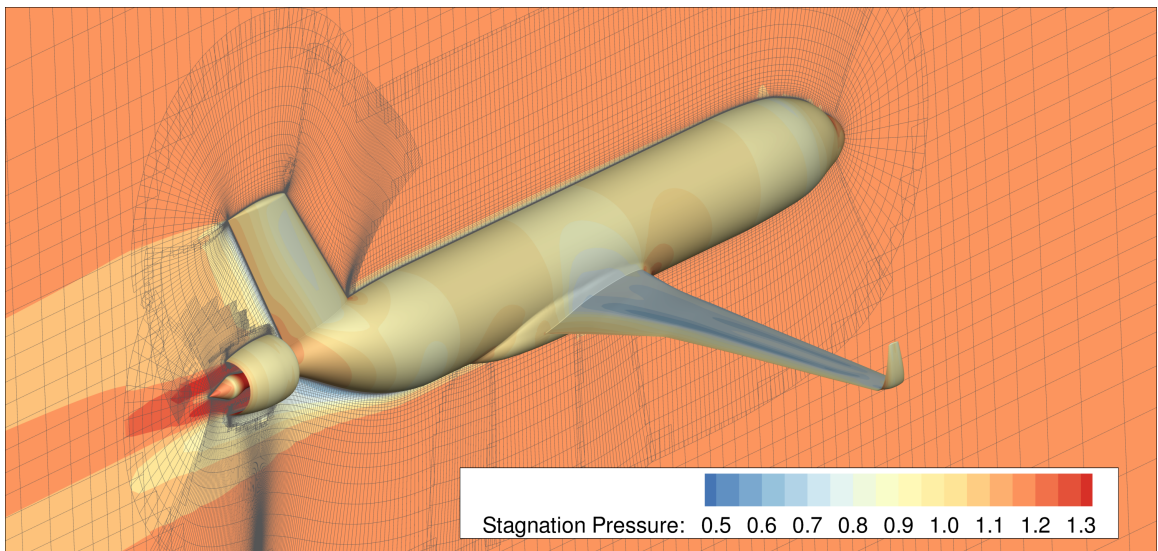


Figure 6.3: Overset mesh of the model with surface C_p color contours.

Figure 6.4, where contours of total pressure indicate the pressure rise which captures the effect of the fan.

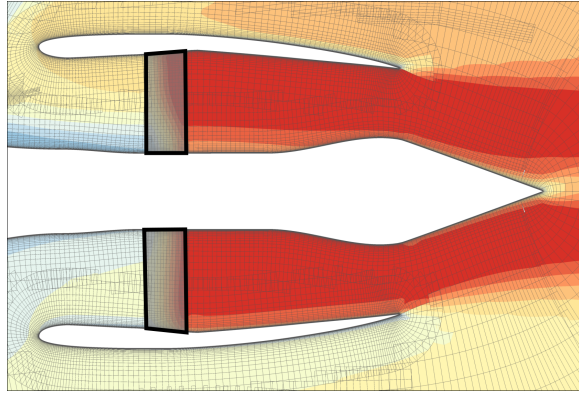


Figure 6.4: Side view of the aft mounted BLI propulsor including the body-force zone that simulates the fan. The p_t color contours show the effect of the van via the increased pressure.

6.1.3 Grid Convergence Study

A grid convergence study was performed to verify the model convergence properties. This study considered three different grid refinement levels: coarse, medium, and fine. These grids had roughly 6 million, 17 million, and 49 million cells respectively. All the analyses for this grid convergence study were done on the baseline aft fuselage baseline, with the pre-optimized wing shape. Richardson extrapolation is used to estimate the continuum value of two key metrics to demonstrate that the model converges to a reasonable value as the grid spacing is decreased toward 0. For grid convergence results for the coefficient of net force (C_F) are shown in Figure 6.5, which presents a continuum value of 66 force counts. I also examined the distortion metric in order to ensure that this relatively new aerodynamic functional value also displays good convergence properties. Figure 6.6 shows that Richardson extrapolation predicts a continuum value of 0.04255 for the aggregated distortion metric ($\hat{\kappa}$). These convergence studies adhere to the expected second order convergence behavior, given that ADflow uses a second order finite volume scheme.

6.1.4 Force Accounting

In typical aircraft analysis the force accounting scheme assumes that the fuselage, wings, and other components create drag and the propulsion system produces thrust. This traditional thrust/drag accounting scheme breaks down for aeropropulsive systems because

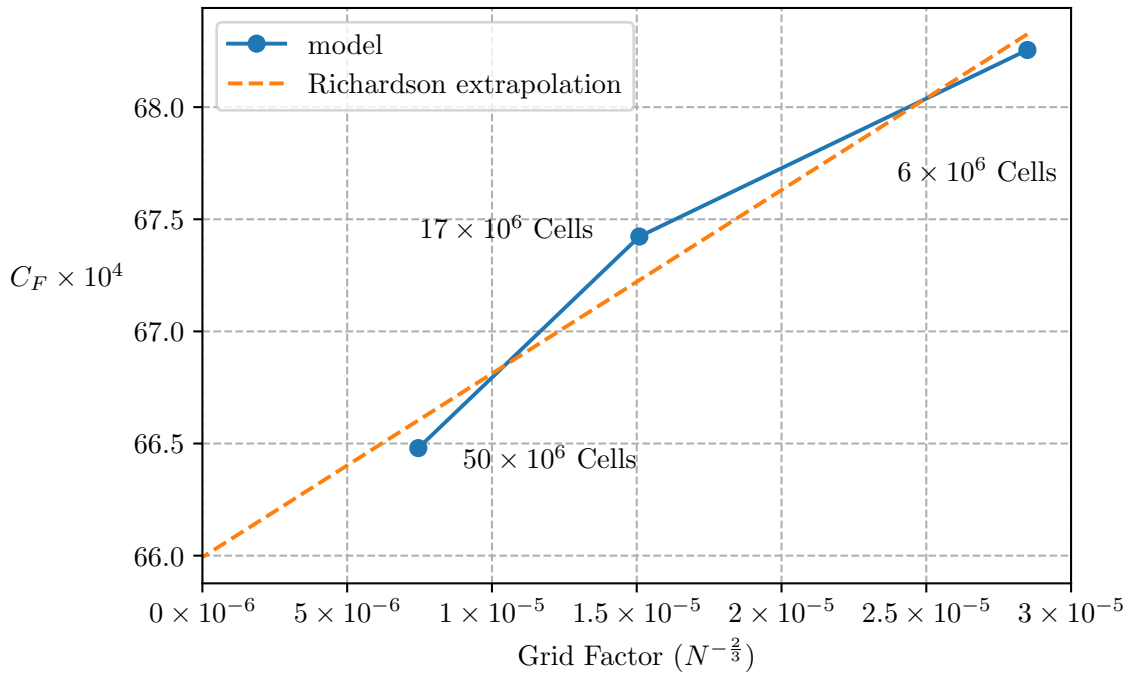


Figure 6.5: Grid convergence study on the convergence of the coefficient of net force (C_F) for the 3-D STARC-ABL aerodynamic model.

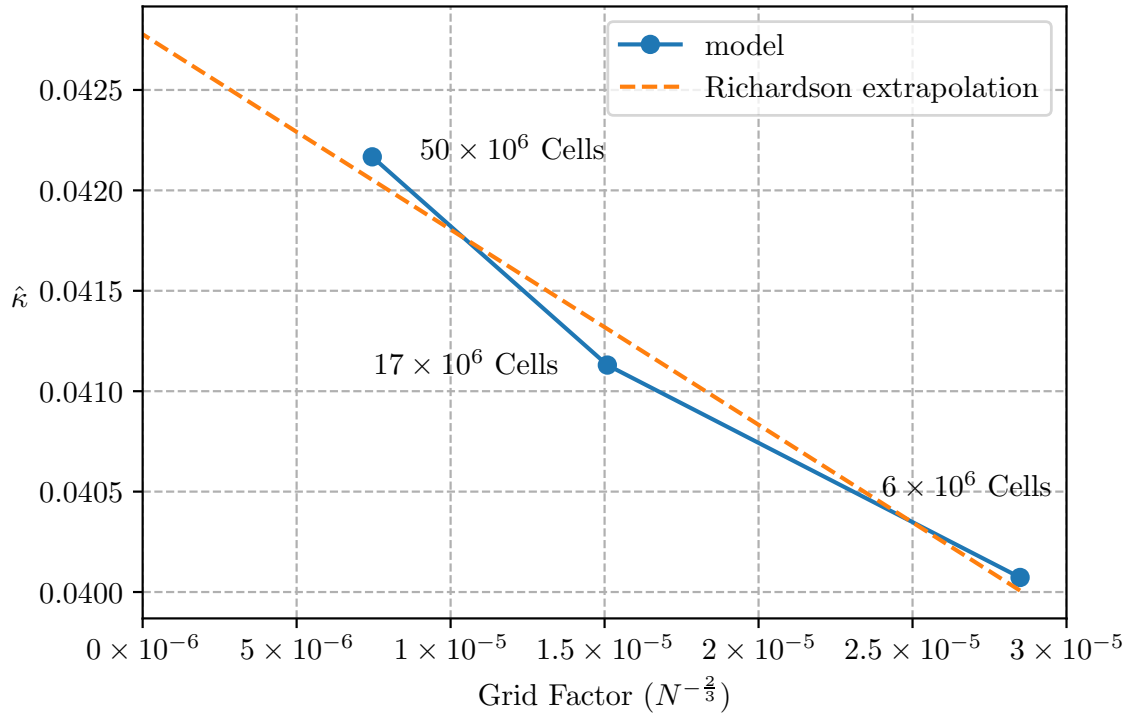


Figure 6.6: Grid convergence study on the convergence of the aggregated distortion metric ($\hat{\kappa}$) for the 3-D STARC-ABL aerodynamic model.

the interactions between the aerodynamic and propulsion systems makes it impossible to neatly separate out thrust and drag components.

In this work, when forces are required, thrust-drag components are not separated out at all. Instead, a signed force (or force coefficient) is computed by integrating pressure and viscous forces across all the walls in the aerodynamics model and then adding any force contribution from body-force zone. The total force coefficient on the aircraft is computed by:

$$C_F = \frac{2}{\rho_\infty V_\infty^2 A_{\text{ref}}} \left[\iint_S \left(((p - p_\infty) \hat{\mathbf{n}} + \vec{\mathbf{f}}_{\text{visc}}) \right) dS + (\vec{F}_{\text{BLI}} \cdot \hat{\mathbf{n}}_{\text{BLI}}) \right]. \quad (6.1)$$

In Equation (6.1), F_{BLI} represents the force contribution from body-force zone of the aft propulsor. This is not the same as the net thrust from that propulsor, but rather is the net force that would be felt by the fan itself. The integration surface, S , is composed of every wall of the airframe: wing, tail, fuselage, and the inside and outside of the propulsor nacelle. C_F represents the net force coefficient of the entire wing-fuselage-tail-propulsor system, and as such it is a signed quantity. A positive value indicates a net decelerating on the body, while a negative value indicates a net accelerating force on the body. Note that C_F does not include the contribution from the under wing propulsor because they are not modeled in this work. For a cruise condition with a constant velocity the net force coefficient of the entire aircraft should be 0, but here C_F is a positive quantity representing a net decelerating force because the under wing propulsor is excluded from the force summation. Effectively, C_F represents the required force coefficient that must be generated by the under wing engines to reach a steady cruise condition.

At the specified cruise conditions (Mach 0.785 and 37000 ft) the values are used to normalize all force calculations are given in Table 6.1.

Table 6.1: Reference values for force normalization.

	value	units
ρ_∞	0.3506	kg/m ³
A_{ref}	105.8	m ²
V_∞	231.7	m/s

6.1.5 Computing BLI Propulsor Power

In order to interface with the propulsion model the power being used by the BLI fan needs to be computed via an volume integral over body-force zone:

$$\text{Pwr}_{\text{flow}} = \iiint \left(\vec{V}_{\text{local}} \cdot \vec{\mathbf{f}}_{\text{local}} \right) dv, \quad (6.2)$$

where \vec{V}_{local} is the local velocity vector and $\vec{\mathbf{f}}_{\text{local}}$ is the local body-force contribution for the infinitesimal fluid volume. $\vec{\mathbf{f}}_{\text{local}}$ is computed by distributing the input \vec{F}_{BLI} across all cells within the body force zone according to the relative volume of each cell.

Note that Equation (6.2) computes only the power imparted to the flow by the fan, which does not equal the total shaft power needed to drive the fan. The shaft power and the flow power differ because of the fan adiabatic efficiency, η_{fan} . Thermodynamically, η_{fan} causes a slight increase in temperature of the flow, relative to what you would expect for ideal case. The implementation of the body-force zone used in this work assumes an isentropic pressure rise, based on the formulation of Hall et. al. [103]. Since the pressure ratio of the fan is so small, the lack of the temperature rise in the flow does not introduce major aerodynamic error. However the effect is significant to the propulsion system, which must ultimately provide the necessary shaft power, so η_{fan} is accounted for in the propulsion model.

6.2 Propulsion Model

6.2.1 1D Cycle Model: pyCycle

The propulsion model used is a one-dimensional thermodynamic cycle model, built with pyCycle, which was discussed in Chapter 3. The 1-D propulsion model requires scalar flow quantities as inputs, but the aerodynamic analysis computes the flow quantities as a nonuniform distribution over a two-dimensional plane. At the interface between the aerodynamic analysis and the propulsion model the two-dimensional data needs to be averaged into equivalent one-dimensional values, but it is important for this process to be done in a conservative fashion so that the correct net force on the boundary is retained in both analyses.

There are a number of different approaches to do this averaging, which conserve different flow quantities. Livesey [109, 110] compared a number of different methods, from the perspective of computing scalar values from rake data measured in a experiment, concluding that an entropy conserving approach was the most useful in that context because

that ensured that physically meaningful pressure loss coefficients are computed when the averaged values are compared at multiple axial locations.

In this application, the interface plane represents a transition from one analysis to another and the principal concern is that the net force on the interface plane is the same between the two analyses. The forces are governed by the static pressure and momentum flux through the interface plane, so these are the quantities we seek to conserve. In the aerodynamic analysis, the force normal to any plane is computed by

$$F_S = \iint_S \left[(p - p_\infty) + \rho(V - V_\infty)(\vec{V} \cdot \hat{\mathbf{n}}) \right] dS. \quad (6.3)$$

If we assume uniform values across the plane, so the flow can be represented by scalar values, Equation (6.3) simplifies to

$$F_S = \left[(\bar{p} - p_\infty)A_S + \dot{m}(\bar{V} - V_\infty) \right] \hat{\mathbf{n}}. \quad (6.4)$$

Over any given plane, the total mass flow rate and area can be computed via

$$\dot{m} = \iint_S \rho \vec{V} \cdot \hat{\mathbf{n}} dS, \quad (6.5)$$

$$A = \iint_S dS. \quad (6.6)$$

Equating Equations (6.3) and (6.4), canceling out the p_∞ and V_∞ terms, and separating the pressure and velocity components yields

$$\bar{p} = \frac{1}{A} \iint_S p dS, \quad (6.7)$$

$$\bar{V} = \frac{1}{\dot{m}} \iint_S V \rho (\vec{V} \cdot \hat{\mathbf{n}}) dS \quad (6.8)$$

These equations show that a force-conserving averaging scheme requires the inflow conditions to the propulsion model should be chosen such that the static pressure matches the area averaged static pressure, and the flow velocity should match the mass averaged velocity on the interface plane. To implement this I varied the 1-D propulsor inlet conditions to find the total pressure (p_t), total temperature (T_t), and mach number (MN) to match the static conditions computed by the propulsion model to the computed values from the

aerodynamic model. This gives three implicit residuals to converge:

$$\mathcal{R}_p(p_t) = p_s^{\text{prop}} - p_s^{\text{aero}} = 0 \quad (6.9)$$

$$\mathcal{R}_T(T_t) = V^{\text{prop}} - V^{\text{aero}} = 0 \quad (6.10)$$

$$\mathcal{R}_{\text{MN}}(\text{MN}) = A^{\text{prop}} - A^{\text{aero}} = 0. \quad (6.11)$$

The \dot{m} computed by the aerodynamic model is used as a direct input to the propulsion model, which provides the last value needed to fully describe the 1-D propulsion model flow state.

6.2.2 BLI Propulsor Model

Although the thrust from the BLI propulsor is modeled via a body-force actuator zone in the aerodynamics model, a propulsion model is still needed to compute the shaft power required to produce that thrust. The BLI propulsor model is composed of four cycle elements: *CFD Start*, *Fan*, *Atmosphere*, and *Performance*. The model structure is shown in Figure 6.7, including these four elements and the Newton solver used to converge the implicit relationships.

The *CFD Start* relies on the Newton solver to implement the force conserving flow averaging scheme described in Chapter 6.2.1. The *Atmosphere* component uses a 1976 standard atmosphere to compute the freestream flow properties. The *Fan* and *Performance* elements handle the actual thermodynamic calculations that compute a required shaft power, given \dot{m} and FPR computed by the aerodynamic analysis and the assumed power transmission efficiency η_{trans} . Figure 6.7 shows the connections between the four cycle elements of this model.

The fan efficiency is computed such that the polytropic efficiency ($\eta_{\text{polytropic}}$), is held constant at 97%, which matches the technology assumptions for NASA's N+3 high bypass ratio turbofan engine [30]. The effect of holding a constant η_{poly} is that the adiabatic efficiency of the fan, $\eta_{\text{adiabatic}}$, — the quantity that directly impacts the shaft power— varies with respect to fan pressure ratio (FPR) and is always less than 97%. The resulting variation of $\eta_{\text{adiabatic}}$ is nearly linear because of the very low FPR, as shown in Fig. 6.8. Although the trend in this situation is nearly linear, the actual relationship between $\eta_{\text{polytropic}}$ and $\eta_{\text{adiabatic}}$ is highly nonlinear:

$$\eta_{\text{polytropic}} = \frac{R \ln(\text{FPR})}{R \ln(\text{FPR}) + S_{\text{out}} - S_{\text{in}}}, \quad (6.12)$$

where R is the specific gas constant for air and S_{in} and S_{out} are the entropy of the air entering and exiting the fan respectively. The entropy of the air exiting the fan is related

to the adiabatic efficiency of the compressor via the compressor calculations described in Chapter 3. In order to enforce the assumed constant polytropic efficiency, a Newton solver is used to drive an additional residual to 0:

$$\mathcal{R}_\eta(\eta_{\text{adiabatic}}) = \eta_{\text{polytropic}} - \eta_{\text{polytropic}}^* = 0. \quad (6.13)$$

This model outputs the required generator power, which takes into account both the fan efficiency ($\eta_{\text{adiabatic}}$) and the power transmission efficiency (η_{trans}) and the nozzle pressure ratio (NPR). This output shaft power is used as objective function in the overall optimization and the nozzle pressure ratio is used as a constraint.

6.3 Aeropropulsive Optimization

6.3.1 Optimization Problem

The performance of the BLI system was analyzed at the cruise condition, Mach 0.785 and 37000 ft. For a steady cruise, there will be zero net force over the entire aircraft, including the under-wing propulsors, wings, tail, fuselage, and aft-propulsor. A portion of the thrust

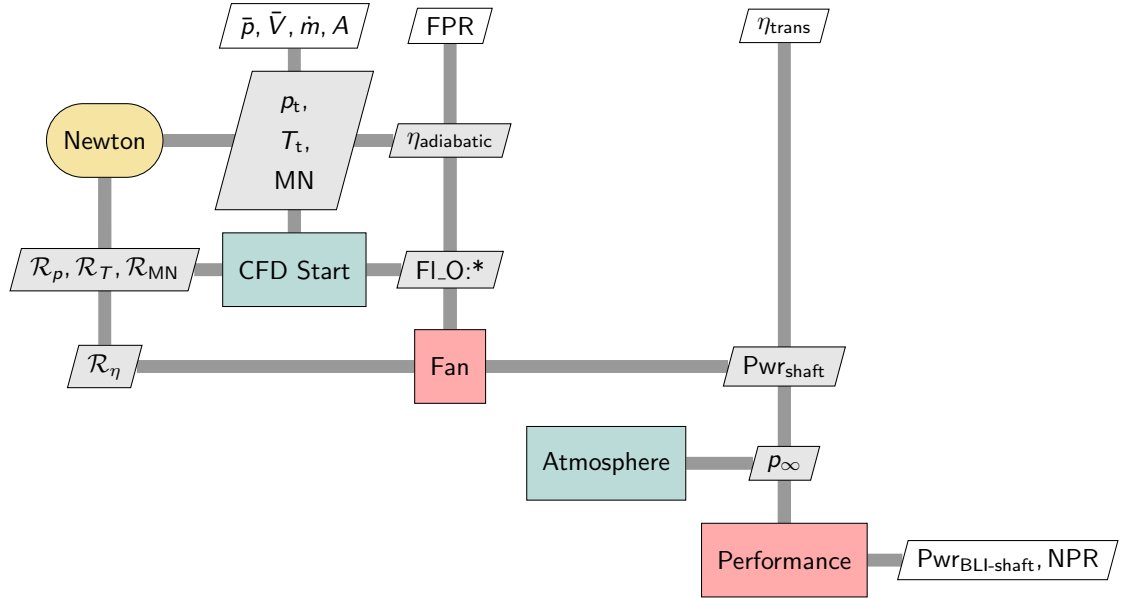


Figure 6.7: Cycle elements in the pyCycle model of the BLI propulsor. Red elements are explicit calculations, blue elements are implicit calculations.

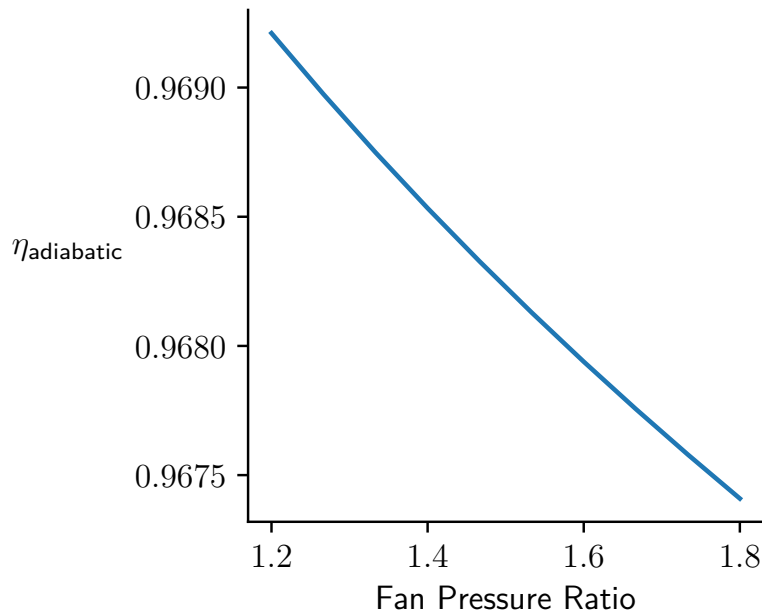


Figure 6.8: Fan adiabatic efficiency versus FPR, assuming a constant polytropic efficiency of 97%.

will come from the under-wing propulsor and a portion from the aft-propulsor. One primary consideration in the propulsion system design is what the optimal split between the under-wing and aft propulsors should be to achieve the lowest overall fuel consumption. For a full aircraft design process addressing this question requires many considerations, such as thermodynamic performance, propulsion system weight, and aircraft center of gravity. In this work I have modeled only the thermodynamic performance of the aft-propulsor, and hence I cannot fully address this design question. However, in recognition of the importance of propulsor sizing to the overall aircraft performance I consider optimized designs of BLI propulsors for three different sizes and compare their relative performance.

All optimizations were set up to minimize the shaft power required by the BLI propulsor at the cruise condition with respect to fuselage shape design variables and propulsion design variables, subject to set of constraints. Two sets of optimizations were run: one without a distortion constraint and one with it. The problem formulation for the non-distortion constrained optimization is given in Table 6.2, which describes the 26 design variables and 14 constraints. Of the 14 constraints, the F_{net} constraint is the most physically significant because that is what ultimately sizes the BLI propulsor. The 10 geometric thickness constraints are cheap to evaluate because they do not involve the CFD analysis at all, so overall, the problem requires just four expensive quantities of interest that involve the CFD analysis. The lower number of quantities of interest means that the it is more efficient to

use OpenMDAO’s reverse mode (adjoint) linear solves to compute the derivatives for the gradient based optimizer. The use of the nozzle pressure ratio constraint is notable here, because it is not normally used to govern the design of a fan. In this work, the NPR constraint was used in lieu of a constraint on FPR because it was more well behaved for shape optimization of the propulsor duct.

Table 6.2: Optimization problem definition for the aero-propulsive design of the propulsion system without a distortion constraint.

	Variable/Function	Description	Quantity
minimize	$P_{\text{BLI-shaft}}$	Shaft power required for the BLI propulsor	
with respect to	α	angle of attack	1
	F_{BLI}	BLI propulsor body-force applied	1
	X_{shape}	Fuselage and propulsor nacelle shape variables	25
	Total		27
subject to	$C_L = 0.5$	Lift coefficient at cruise	1
	$0.99 < g_{\text{geo}} < 3.0$	Geometric thickness constraints	10
	$\text{NPR} > 1.65$	Nozzle pressure ratio constraint	1
	$F_{\text{net}} = F_{\text{net}}^*$	Required net force on the body	1
	Total		14

Using a sign convention derived from the aerodynamic model with the origin located at the aircraft nose, positive values of net force represent a decelerative force on the body. Since the aerodynamic model only includes the aft propulsor, the F_{net} value computed from it represents the amount of net thrust required from the under-wing propulsors for a steady cruise condition. In other words a larger F_{net} indicates larger under-wing propulsors and a smaller aft-propulsor.

Figure 6.9 shows the XDSM[1] of the fully coupled aeropropulsive optimization, indicating how data is passed between the different analyses. The four different analyses are coupled using OpenMDAO, which both solves the nonlinear analysis and computes the total derivatives needed by the optimizer using an adjoint formulation. As in Chapter 5, the IDF [63] optimization architecture is used to enforce the coupling.

In Figure 6.9, there is a component labeled *VSP Preprocessing*. The geometry engine for this work is OpenVSP, which is integrated directly inside the *ADflow* discipline. OpenVSP exposes a number of parameters that control the shape and diameters of cross-sections on both the fuselage, BLI nacelle, and wing. However, for this work, a number of those parameters were linked together to provide a more physically meaningful geometry parameterization. For example, in the OpenVSP model the sharp trailing edge of the nacelle is

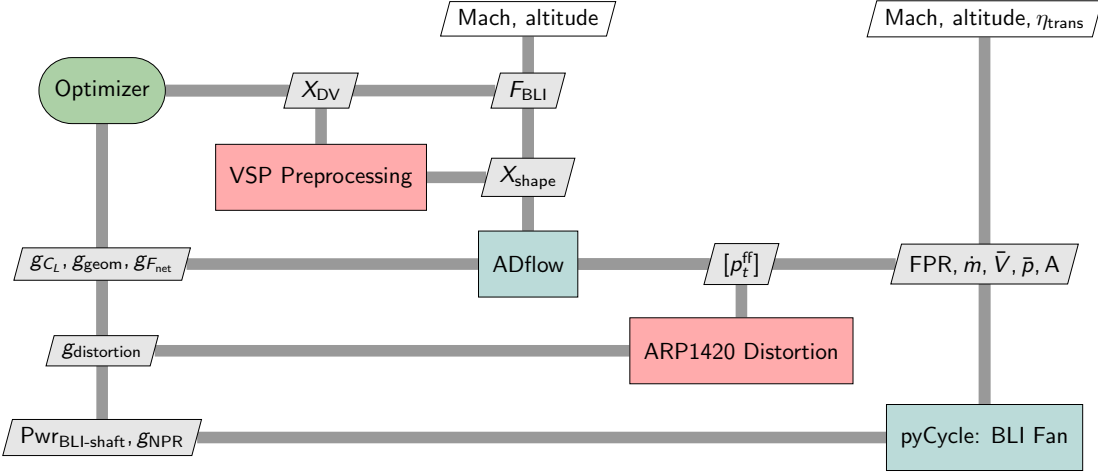


Figure 6.9: XDSM diagram of the full optimization problem formulation.

parameterized with two separate diameters: one for the upper surface and one for the lower surface. It is important that both these diameters are always forced to take the same value, so the geometry stays water tight. This is accomplished via the *VSP Preprocessing* component in the model, which takes a set of design variables and relates them to the actual OpenVSP model inputs.

The *ARP1420 Distortion* component implements the distortion metric from the “Gas Turbine Engine Inlet Flow Distortion Guidelines” ARP1420 standard[111], using the scheme developed by Kenway and Keris [39]. The metric captures the magnitude of the circumferential variation in total pressure across the fan face as

$$\kappa^i = \frac{\hat{p}_t^i - \bar{p}_t^i}{\bar{p}_t^i}, \quad (6.14)$$

where \hat{p}_t and \bar{p}_t represent two different average total pressure values: average total pressure below the mean and overall mean total pressure. These two pressures are more clearly understood graphically, via the right side of Figure 6.10. That is a notional pressure trace taken at a single radial measurement location, with the two relevant pressure averages denoted.

The i superscript in Equation 6.14 denotes a specific radial ring of pressure measurements. In this model, five radial measurement locations are used each with 30 sensors distributed evenly in the circumferential direction yielding a total of 150 sensors. The pressure rake is shown graphically on the right side of Figure 6.10. The five distortion measurements from each of the five radii are aggregated with a KS function [112], giving a smoothed maximum value that can be used as an additional constraint on the optimization

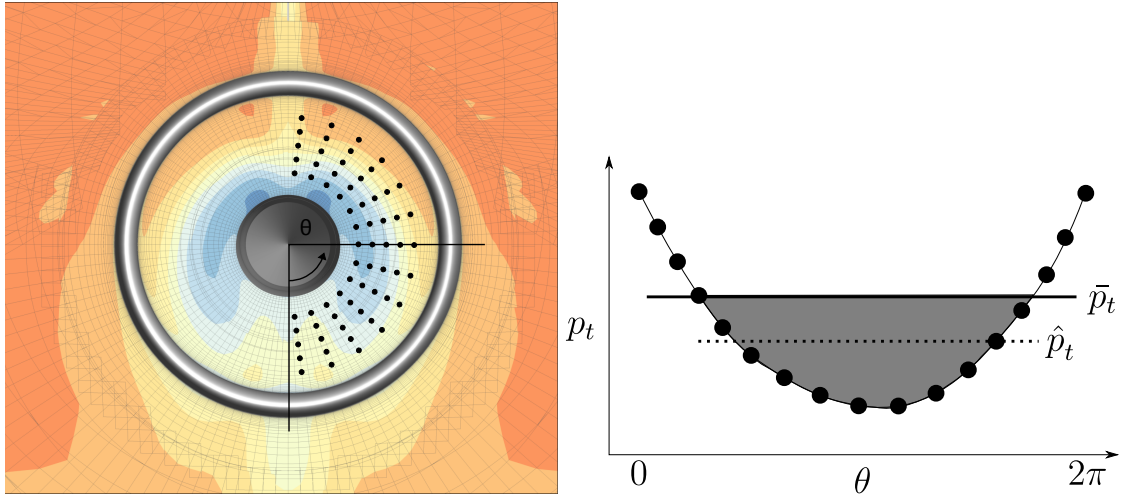


Figure 6.10: ARP1420 distortion calculation diagram, showing the notional pressure rake locations (left) and a notional pressure trace taken across a single radial measurement stations (right).

$(\hat{\kappa})$. The modified optimization problem formulation, including the additional aggregated constraint on distortion, is shown in Table 6.3

Table 6.3: Optimization problem definition for the aero-propulsive design of the propulsion system with a distortion constraint.

	Variable/Function	Description	Quantity
minimize	$\text{Pwr}_{\text{BLI-shaft}}$	Shaft power required for the BLI propulsor	
with respect to	α	angle of attack	1
	F_{BLI}	BLI propulsor body-force applied	1
	X_{shape}	Fuselage and propulsor nacelle shape variables	25
		Total	27
subject to	$C_L = 0.5$	Lift coefficient at cruise	1
	$0.99 < g_{\text{geo}} < 3.0$	Geometric thickness constraints	10
	$\text{NPR} > 1.65$	Nozzle pressure ratio constraint	1
	$F_{\text{net}} = F_{\text{net}}^*$	Required net force on the body	1
	$\hat{\kappa} < .035$	aggregated distortion metric	1
	Total		15

6.3.2 Optimization Results

Three pairs of optimizations were performed for F_{net}^* values of 9000 N, 11000 N, and 13000 N. When normalized these forces correspond to $C_F \times 10^4$ if 90.39, 110.5, and 130.6 re-

Table 6.4: Optimization results for the 3-D STARC-ABL aeropropulsive optimization with and without a distortion constraint

$C_F \times 10^4$	unconstrained			κ constrained		
	FPR	$\kappa (\hat{\kappa})$	Pwr _{shaft} (kW)	FPR	$\kappa (\hat{\kappa})$	% Δ Pwr _{shaft}
90.39	1.233	0.0440 (0.0447)	3646.5	1.236	0.0300 (0.0350)	1.2
110.5	1.271	0.0426 (0.0434)	3177.9	1.308	0.0313 (0.0348)	0.9
130.6	1.286	0.0403 (0.0413)	2623.3	1.286	0.0312 (0.0350)	0.12

spectively. One set was performed without the distortion constraint, and the other with it. Key performance parameters from each optimization are reported in Table 6.4. The 9000 N case yields the largest aft-propulsor and hence requires the most shaft power. Compared to the 9000 N case, the 11000 N case requires 22% more thrust from the under-wing propulsors and uses 14.6% less shaft power for the BLI propulsor. The 13000 N case requires 44% more thrust from the under-wing propulsors and uses 29.2% less shaft power for the aft propulsor. For all three cases, the constraint on NPR limits the fan pressure ratio from going below 1.23. The main conclusion from the data in Table 6.4 is that the impact of the distortion constraint on the BLI propulsor performance is dependent on the propulsor size. The largest BLI propulsor ($C_F \times 10^4 = 90.39$) requires 1.2% more shaft power to reach the same overall net force on the body. That case also had the highest distortion for the non-constrained optimization, which partially explains the large impact of the distortion constraint because for that case the distortion constraint was effectively more restrictive. The largest propulsor is ingesting some non-boundary layer air on the upper side of the aircraft fuselage, which contributes to the increased distortion in the non-constrained case.

Figure 6.11 shows the side and front views of the baseline and optimized geometries for the three F_{net}^* cases. The color contours show the total pressure levels around the aircraft, where the front view contours highlight the distortion in the inlet for the BLI propulsors. In all three cases some shaping on the nozzle plug also helps alleviate some minor flow separation and yield slightly better overall performance. Compared to the baseline geometry, the nacelle walls are thicker near the leading edge and much thinner near the trailing edge compared to the baseline. The pressure contours also indicate that the flow is more uniform exiting the nozzle in the optimized cases.

All cases (baseline and three optimized geometries) have a zone of higher total pressure at the bottom of the BLI propulsor inlet near the hub. Out toward the tip, the bottom of the propulsor inlet has a lower total pressure zone. This would create a one-per-revolution excitation in the fan blades and that would require careful aerostructural design. This circumferential distortion is what the added constraint seeks to limit for the second set of

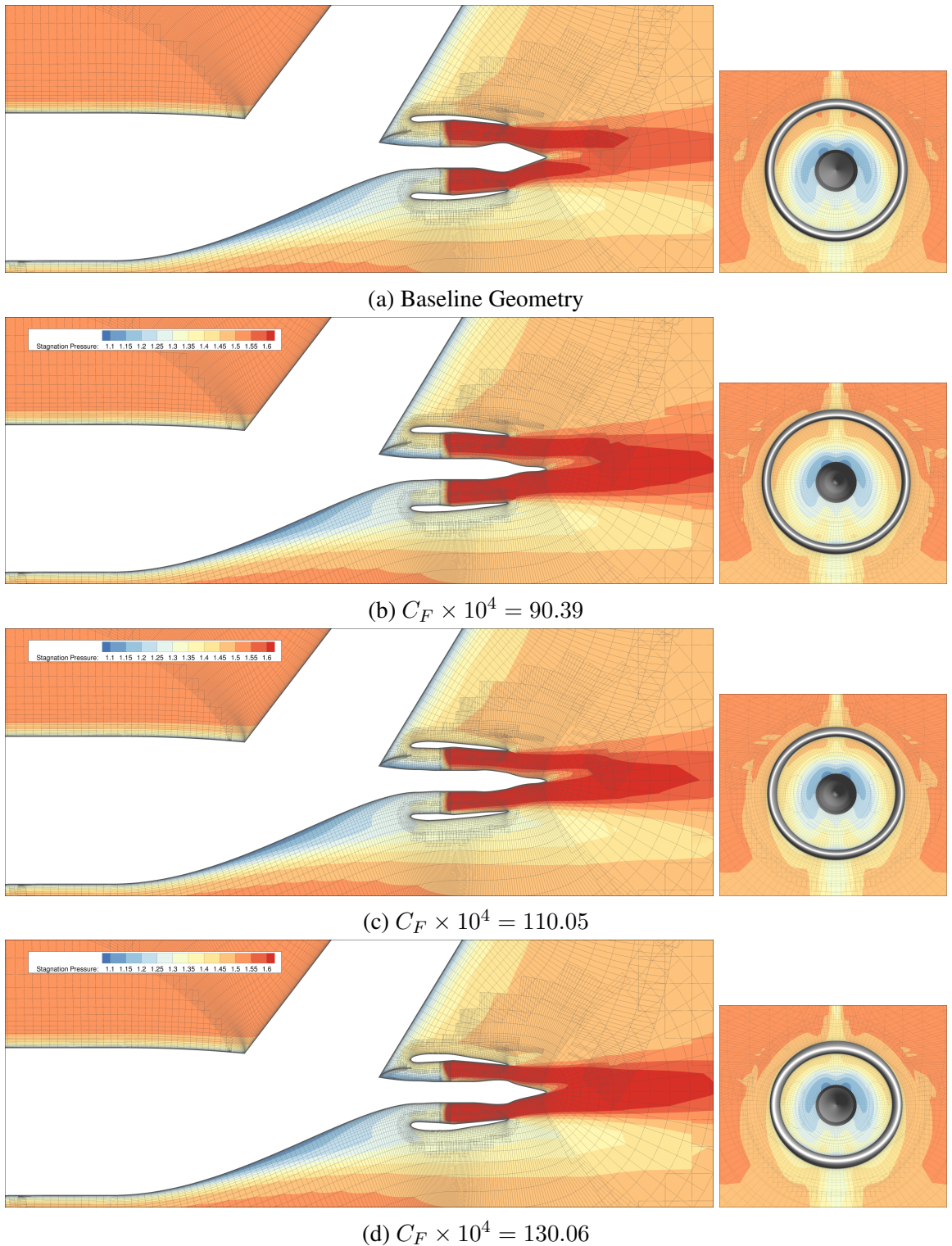
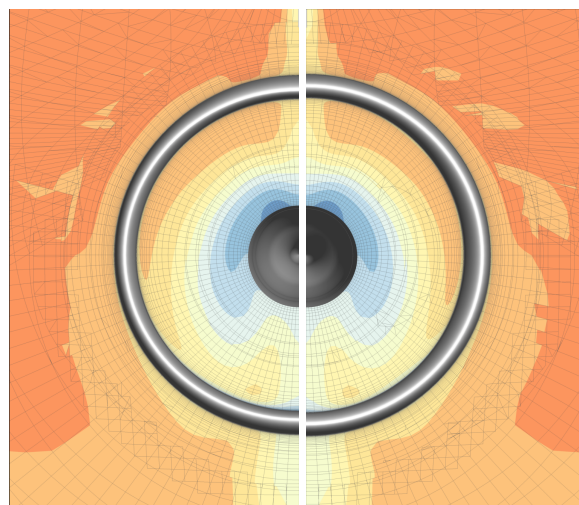


Figure 6.11: Contours of stagnation pressure for the baseline and three optimized geometries.

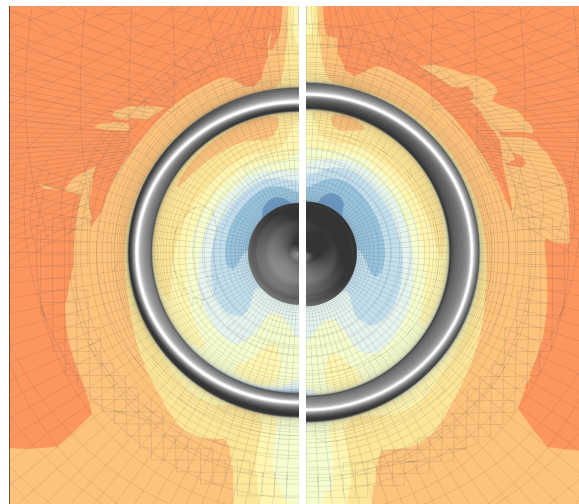
optimizations. The results of the distortion constrained optimizations are shown in Figure 6.12. These front views of the inlet highlight now the optimizer was able to restrict the distortion to the allowable levels. In all cases, the optimizer respected the overall constraint on the aggregated distortion ($\hat{\kappa}$), but because of the conservative nature of the KS function used to aggregate the actual maximum distortion (κ) is always a bit lower than the aggregated value.

Figure 6.12 shows some consistent geometric trends between the three sets of cases run. In all cases, the distortion constrained inlet has a thicker inlet profile than the unconstrained one. The inlet lips tend to move radially outward somewhat as well, creating a more sharp lipped profile. The overall inlet diameters do not vary strongly between the constrained and unconstrained cases. A more quantitative understanding of how the distortion constraint changed the inlet flow is presented in Figures 6.14, 6.15, and 6.16 which present the pressure measurements taken by the sensor rake, which is shown in Fig. 6.13. The color of each sensor ring in Fig. 6.13 matches with the pressure plot in Figures 6.14, 6.15, and 6.16. The most notable conclusion from the data in the pressure plots is the relatively minor changes to the overall pressure levels that are caused by the distortion constraint. The fairly large physical variations in the inlet design shown in Fig. 6.12 yield much more subtle changes in the fan face total pressure distribution which give a 1%–1.5% reduction in maximum distortion.

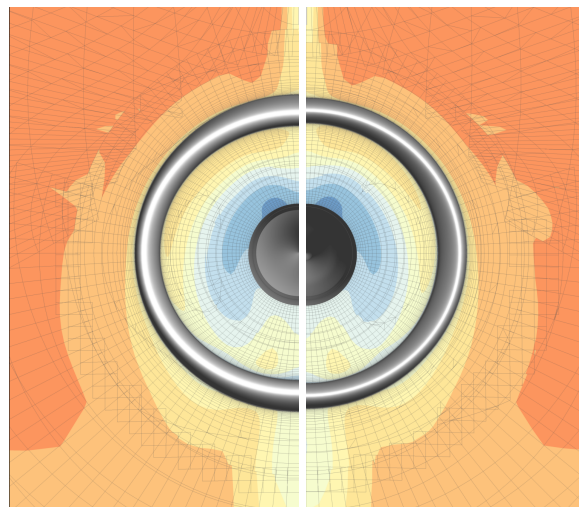
Effectively all of the change between the unconstrained and constrained cases occurs in the outermost purple ring for all three cases. This makes sense because that ring shows the largest variation in total pressure signal around the annulus, and hence will be the dominant contribution to the aggregated constraint ($\hat{\kappa}$). From a fan blade structural perspective the outer annulus is also the most important because it has the longest moment arm on the blade to create bending loads. Another important trend in these three figures, which carries through all three propulsor sizes, is how the inner (r_0) and outer (r_4) rings have pressure signatures that are nearly 180 degrees out of phase with each other. In other words, the r_0 ring has a lower pressure at the same circumferential location that the r_4 has a high pressure. This trend was also noted in the qualitative results displayed in Figure 6.11, but its much more clearly seen in the pressure traces from Figures 6.14, 6.15, and 6.16. There is a smooth transition in phase angle between the rings as they progress farther outward, and the overall amplitude of the signal increases as you move outward as well. The r_1 , r_2 , and r_3 show relatively light distortion, because the variation from the mean is fairly weak. The major distortion is at the hub and top radial stations r_0 and r_4 respectively.



(a) $C_F \times 10^4 = 90.39$



(b) $C_F \times 10^4 = 110.05$



(c) $C_F \times 10^4 = 130.06$

Figure 6.12: Front view comparison between the optimized designs for the unconstrained (left) and distortion-constrained (right) BLI propulsor inlet for the different cases considered.

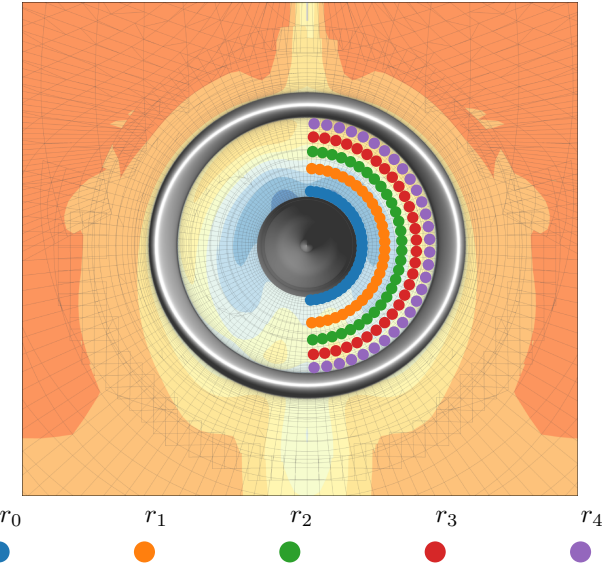


Figure 6.13: Actual numerical pressure rake used to compute distortion metric, with 150 measurement locations arranged in 5 semicircular rings (r_0-r_4) of 30 sensors each. θ starts at the bottom location and rotates counter-clockwise toward the top.

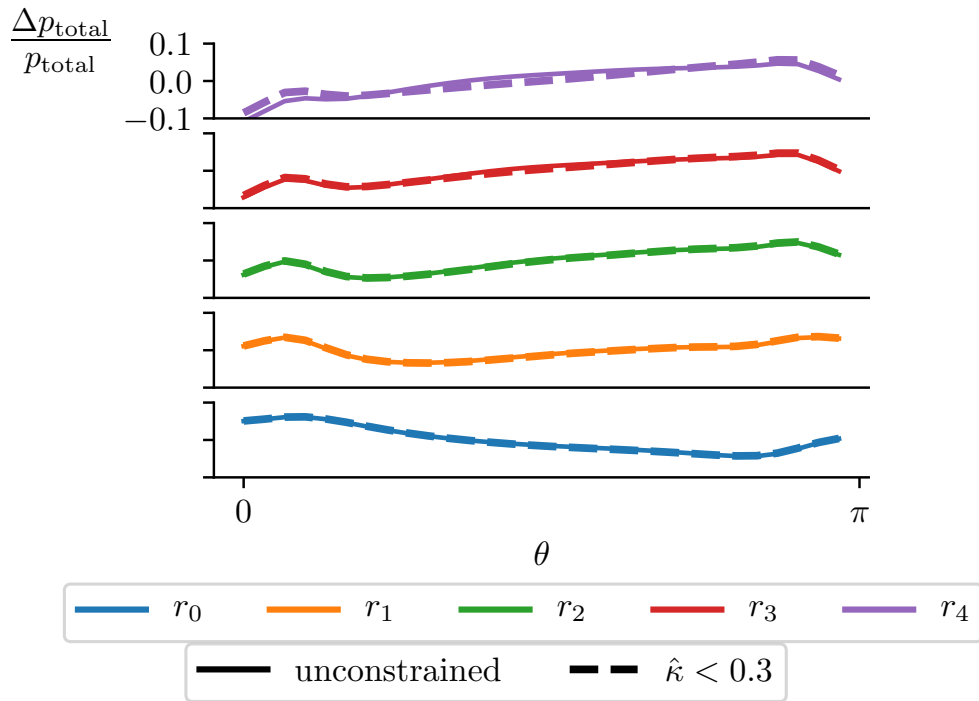


Figure 6.14: $\Delta p_{\text{total}}/p_{\text{total}}$ vs annular location (θ) for rakes 0-4, for the $C_F \times 10^4 = 90.39$ case.

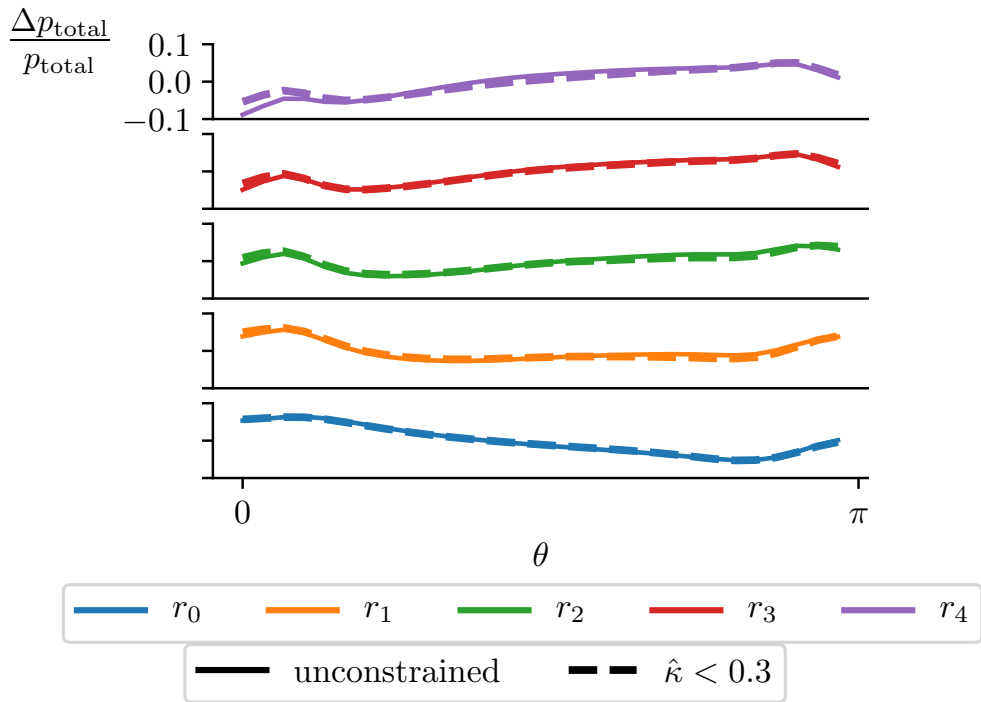


Figure 6.15: $\Delta p_{\text{total}}/p_{\text{total}}$ vs annular location (θ) for rakes 0-4, for the $C_F \times 10^4 = 110.05$ case.

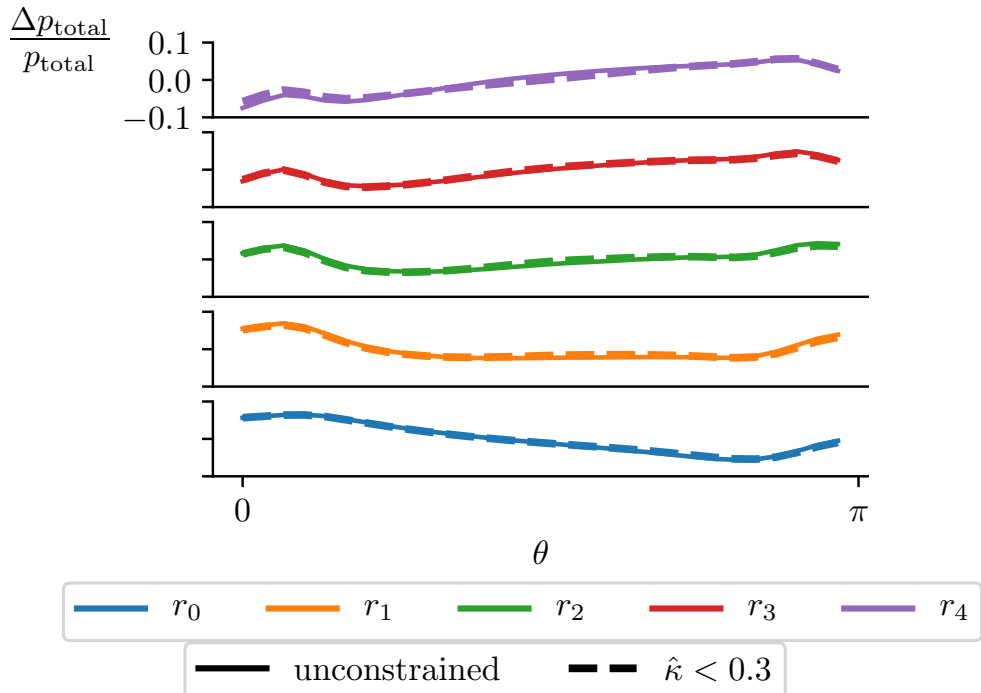


Figure 6.16: $\Delta p_{\text{total}}/p_{\text{total}}$ vs annular location (θ) for rakes 0-4, for the $C_F \times 10^4 = 130.06$ case.

6.4 Summary

This study used design optimization of a coupled aeropropulsive model with full 3-D aerodynamics to study the impact of a distortion constraint on BLI propulsor performance for the STARC-ABL aircraft configuration. The aeropropulsive model used a novel coupling strategy that combined a body-force zone to predict propulsor thrust with a 1-D thermodynamic cycle model to predict propulsor power usage.

Six separate aeropropulsive optimizations were run: two sets of cases (with and without a distortion constraint) for three different propulsor sizes. The results presented in Figures 6.12 and 6.11, combined with the data from Table 6.4, show conclusively that aeropropulsive optimization can be used to impose a constraint on distortion by changing the shape of the inlet. The aeropropulsive model is necessary in so that the model can provide shaft power for the objective function and overall net force to use as a constraint. This is necessary to create an apples-to-apple comparison between the distortion-constrained and unconstrained cases which gives an indication of overall efficiency between the two.

The data shows that imposing a distortion constraint causes an increase in required propulsor shaft power relative to the unconstrained case. The magnitude of that increase varies from 1.2% to 0.12% between the largest propulsor and the smallest. From a design standpoint, this poses an interesting dilemma. The purpose of the distortion constraint is to ensure that the fan adiabatic efficiency can be maintained and to reduce the structural loads on the blades so the fan remains light weight. However, if imposing that constraint makes the aeropropulsive system less efficient, then it may be preferable to accept a small penalty on fan efficiency or increased fan weight rather than design for lower distortion. The particular design tradeoff that is best will ultimately depend heavily on the specifics of the actual system being considered. Even within the context of a single aircraft configuration, such as STARC-ABL, the size of the aft propulsor may influence the choice made. Hence, beyond the fundamental results shown in this chapter, the data serves to further underscore the importance of using fully coupled aeropropulsive models for the design of BLI propulsion systems because simply changing the size of the propulsor by $\pm 10\%$ can have an impact on inlet distortion and BLI efficiency.

CHAPTER 7

Concluding Remarks

7.0.1 Summary and Future Work

Boundary layer ingestion (BLI) is an aeropropulsive concept that has the potential to provide a significant reduction in energy usage for aircraft by offering more efficient thrust production. Although the concept was first conceived of almost simultaneously with the development of the jet engine itself, in the late 1940's, it wasn't until the mid 2000's that the concept has seen significant interest in the aircraft community. The delayed interest was due in part to the lack of suitable analysis tools and design methods to handle the coupled multidisciplinary modeling challenge presented by BLI. Another factor in the delay was the availability of performance improvements via single disciplinary optimization (e.g. aerodynamic improvements or improved engine designs). However, by 2012 all the fundamental building blocks were finally in place in the aerodynamics, propulsion, and MDO communities to begin to fully address the coupled modeling challenge of BLI. Additionally, the available single disciplinary improvements have started to dry up. So the time is finally right for the serious investigation into BLI propulsion systems for aircraft.

This thesis presents my research toward addressing the modeling and design method developments required in order to design BLI systems with fully coupled aeropropulsive models. My results have shown that BLI can offer up to 4.6% reduction in power requires for cruise for NASA's STARC-ABL aircraft configuration, and more broadly that improvements of over 10% could be possible for more aggressive BLI applications. These results are not fundamentally novel in and of themselves, because as discussed in Chapter 1.3, many prior studies have predicted the performance potential of BLI propulsion. What is fundamentally new from this work is the use of fully coupled aeropropulsive models to make these predictions, hence providing a much greater degree of confidence in the results.

I performed this research in three phases: (1) Establish the fundamental need for aeropropulsive models; (2) Perform the first ever aeropropulsive design optimization on fully coupled aeropropulsive model using 2-D aerodynamics; (3) Perform a more complex

design optimization using a 3-D aerodynamic model.

In the first two phases I used a simplified 2-D axisymmetric configuration, based on the STARC-ABL, to look at the core of the aeropropulsive behavior for the aft BLI propulsor. These results established that the aeropropulsive interactions are a dominating factor in BLI performance. The BLI benefit comes from essentially equal parts aerodynamic and propulsive improvements, and interaction effects cause throttle dependent C_L , C_D , and C_M that pose serious challenges for the standard decoupled aircraft design and analysis methods.

In the third phase, I graduated to a fully 3-D aerodynamic model of the STARC-ABL in order to account for the important 3-D effects that impact BLI performance. The presence of the tail, non-axisymmetric fuselage, and wing downwash all contribute to distortion at the fan-face which has the potential to erode some of the BLI benefit. This work leveraged design optimization to study the impact of enforcing a constraint on inlet distortion, which was respected via aerodynamic shape changes in the fuselage and inlet shape. I found that enforcing a distortion constraint had an measurable effect with a variable magnitude dependent on the size of the aft propulsor. Larger propulsors suffered larger performance degradation from the enforcement of the distortion constraint than smaller ones. Though I have established that it is possible to limit distortion using design optimization, the negative impact on BLI efficiency begs the question as to whether a distortion constraint is the right fundamental design approach or not.

Overall, I believe this thesis has established the fundamental worth of BLI propulsion systems in general, and specifically for the STARC-ABL configuration that I studied in detail. Although this thesis provides a significantly more detailed understanding of the BLI propulsor design than what has come before, specifically studying the issue of aft-propulsor sizing in great detail, I have not dealt with several important aircraft design considerations such as tail-strike considerations, weights and sizing, and mission related thrust requirements (e.g. engine-out and second segment climb). Future work needs will need to focus on ways of integrating these considerations into fully coupled design models, or alternatively to leverage aeropropulsive models such as the one used here to provide data for semi-empirical design approaches.

I would like to conclude by saying that that I sincerely hope to see a BLI propulsion system on a production aircraft within my lifetime. I feel that my work, summarized in this thesis, along with the results of the many researchers who's shoulders I stood upon, has shown the tremendous potential of BLI. Hopefully this work contributes to the field and helps to enable the BLI concept to realize its potential on an actual aircraft.

7.0.2 Contributions

The contributions of this thesis are as follows:

1. *I developed the core thermodynamic module and element design for pyCycle, the first 1-D thermodynamic cycle analysis model with analytic derivatives suitable for design optimization of aeropropulsive systems.*

By 2012 almost all of the fundamental analysis and method building blocks for aeropropulsive design optimization were in place, except for one: propulsion models. The state of the art tool for propulsion modeling is NASA's NPSS tool, which is suitable for single disciplinary analysis but can not be effectively used in multidisciplinary optimization context. To overcome this I developed a new formulation for the core thermodynamics module which would enable analytic derivatives to be computed, then I leveraged that new module to build a flexible propulsion modeling tool that I named pyCycle. pyCycle is the first complete propulsion modeling tool to provide analytic derivatives, and hence the first model well suited for use in aeropropulsive design optimization with gradient based optimization.

Throughout the time that I performed research for this thesis, pyCycle has been continually developed by several researchers at NASA Glenn Research Center. However, the core thermodynamics module and the element design patterns were developed by me and represent my contributions to the effort. The other researchers have contributed specific elements and engine models to the code as needed for other research.

2. *I presented the first quantitative study of the importance of aeropropulsive interaction in BLI systems and the mechanisms by which it affects aircraft performance.*

There has been much prior work studying BLI, but nearly all of it has used uncoupled models. The only exception was work from David Rodriguez in 2001 which did use a coupled aeropropulsive model, but only included aerodynamic design variables. The results presented in Chapter 4 are the first to ever include aerodynamic and propulsion design variables in a design space exploration that used a fully coupled aeropropulsive model. The fully coupled model allowed these results to expose the fundamental mechanisms by which BLI efficiency gains are achieved. Additionally the results are the first to provide a quantitative analysis to show that the BLI benefit comes equally from aerodynamic and propulsive benefits.

3. *I implemented the first ever aeropropulsive design optimization of a BLI propulsion system using gradient based optimization and analytic derivatives.*

The initial work on the STARC-ABL aircraft design used manual design space exploration with uncoupled models in order to establish a relative sizing between the under-wing and aft-mounted propulsors. The work I have presented in Chapter 5 is the first ever design optimization of a BLI propulsor using gradient based optimization with analytic derivatives. Implementation of this model required building a coupled model in the OpenMDAO framework that combined a RANS CFD aerodynamic analysis with a 1-D propulsion model. The optimization results presented here represent the first application in OpenMDAO that used a tightly coupled high-fidelity analysis (RANS CFD).

Although the development of OpenMDAO itself is not a direct contribution of this thesis, the framework was conceived with the primary goal of enabling the integration of high-fidelity analyses into the design process. The results presented here represent the realization of that goal. Furthermore they represent the generalization of the tools and methods first developed by Martins and later by Kenway, Kennedy, and Mader and the first application of these methods outside of aerodynamic and aerostructural optimization applications.

4. *I presented the first quantitative sizing study results for the BLI propulsor of the STARC-ABL aircraft concept, using efficient design optimization to demonstrate how BLI efficiency varies with aft-propulsor sizing.*

By leveraging the efficiency of the gradient based optimization with analytic derivatives, in Chapter 5 I was able to use the aeropropulsive model with a RANS CFD aerodynamics analysis to perform the first sizing study for the aft mounted BLI propulsor of the STARC-ABL aircraft configuration. I showed that the assumed transmission efficiency of the turboelectric propulsion system is the most important design assumption governing the overall performance of the BLI propulsor. Depending on the assumed value of that efficiency, the overall power savings of the STARC-ABL aircraft at cruise is between 1% and 4.6%. The results further show that the size of the BLI propulsor necessary to achieve the best performance changes significantly as the assumed transmission efficiency varies. Both the actual efficiency results and the relationship between propulsor sizing and transmission efficiency are fundamentally new results that were not previously known for the STARC-ABL concept.

5. *I presented the first results that show the impact of an inlet distortion constraint on BLI performance by comparing unconstrained and constrained design optimization results of a 3-D coupled aeropropulsive model.*

Chapter 6.4 presents the first ever aeropropulsive design optimization of a BLI propulsor using a fully coupled model with both aerodynamic and propulsion design variables. By leveraging the aeropropulsive model, I present the impact of a distortion constraint on BLI efficiency. The results presented compare unconstrained to distortion-constrained optimized BLI propulsor configurations for a range of propulsor sizes. The results show that a distortion constraint will negatively impact the STARC-ABL aft mounted BLI propulsor between 0.12% and 1.2% depending on propulsor size. The relationship between distortion constraint and BLI efficiency has not been previously presented, nor has the impact of propulsor sizing on that relationship. Both of these results represent new contributions to the BLI literature.

BIBLIOGRAPHY

- [1] Lambe, A. B. and Martins, J. R. R. A., “Extensions to the Design Structure Matrix for the Description of Multidisciplinary Design, Analysis, and Optimization Processes,” *Structural and Multidisciplinary Optimization*, Vol. 46, 2012, pp. 273–284.
- [2] Drela, M., “Power Balance in Aerodynamic Flows,” *AIAA Journal*, Vol. 47, No. 7, 2009, pp. 1761–1771.
- [3] Smith, A. M. O. and Roberts, H. E., “The Jet Airplane Utilizing Boundary Layer Ingestion for Propulsion,” *Journal of Aeronautical Sciences*, Vol. 14, No. 2, 1947, pp. 97–109.
- [4] Lynch, F. T., “A Theoretical Investigation of the Effect of Ingesting Boundary Layer Air on Turbofan Engine Fuel Consumption,” Tech. Rep. SM 23981, Douglas Aircraft Co., 1960.
- [5] Douglass, W. M., “Propulsive Efficiency with Boundary Layer Ingestion,” Tech. Rep. MDC J0860, McDonnell Douglas Corp., 1970.
- [6] Wislicenus, G. F., “Hydrodynamics and Propulsion of Submerged Bodies,” *Journal of the American Rocket Society*, Vol. 30, December 1960, pp. 1140–1148.
- [7] Gearhart, W. S. and Henderson, R. E., “Selection of a Propulsor for a Submersible System,” *Journal of Aircraft*, Vol. 3, No. 1, 1966, pp. 84–90.
- [8] Bruce, E. P., Gearhart, W. S., Ross, J. R., and Treaster, A. L., “The Design of Pump-jets for Hydrodynamic Propulsion,” NASA CR NASA SP-304, National Aeronautics and Space Administration, 1974.
- [9] Betz, A., *Introduction to the Theory of Flow Machines*, Pergamon Press, 1966.
- [10] Smith, L. H., “Wake Ingestion Propulsion Benefit,” *Journal of Propulsion and Power*, Vol. 9, No. 1, February 1993, pp. 74–82.
- [11] Jones, W. P. and Launder, B. E., “The Prediction of Laminarization with a Two-Equation Model of Turbulence,” *International Journal of Heat and Mass Transfer*, Vol. 15, 1972, pp. 301–314.
- [12] Spalart, P. and Allmaras, S., “A One-Equation Turbulence Model for Aerodynamic Flows,” Vol. 439, 01 1992.

- [13] Kim, S., Alonso, J., and Jameson, A., “Two-dimensional high-lift aerodynamic optimization using the continuous adjoint method,” *8th Symposium on Multidisciplinary Analysis and Optimization*, 2000.
- [14] Jameson, A., “Aerodynamic Design via Control Theory,” *Journal of Scientific Computing*, Vol. 3, No. 3, Sept. 1988, pp. 233–260.
- [15] Reuther, J., Jameson, A., Farmer, J., Martinelli, L., and Saunders, D., “Aerodynamic Shape Optimization of Complex Aircraft Configurations via an Adjoint Formulation,” *Proceedings of the 34th AIAA Aerospace Sciences Meeting and Exhibit*, Reno, Nevada, Jan. 1996, AIAA 1996-0094.
- [16] Reuther, J. J., Jameson, A., Alonso, J. J., Rimlinger, M. J., and Saunders, D., “Constrained Multipoint Aerodynamic Shape Optimization Using an Adjoint Formulation and Parallel Computers, Part 1,” *Journal of Aircraft*, Vol. 36, No. 1, 1999, pp. 51–60.
- [17] Reuther, J. J., Jameson, A., Alonso, J. J., Rimlinger, M. J., and Saunders, D., “Constrained Multipoint Aerodynamic Shape Optimization Using an Adjoint Formulation and Parallel Computers, Part 2,” *Journal of Aircraft*, Vol. 36, No. 1, 1999, pp. 61–74.
- [18] Anabtawi, A., *Experimental Investigation of Boundary Layer Ingestion into Diffusing Inlets*, Ph.D. thesis, Univ. of Southern California, Los Angeles, 1999.
- [19] Rodriguez, D. L., *A multidisciplinary optimization method for designing boundary layer ingesting inlets*, Ph.D. thesis, Stanford University, CA, 2001.
- [20] Liebeck, R., Page, M., and Rawdon, B., “Blended-wing-body subsonic commercial transport,” *36th AIAA Aerospace Sciences Meeting and Exhibit, Aerospace Sciences Meetings*, American Institute of Aeronautics and Astronautics, 1998.
- [21] Daggett, D. L., Kawai, R., and Friedman, D., *Blended Wing Body Systems Studies: Boundary Layer Ingestion Inlets With Active Flow Control*, 2003, NASA CR-2003-212670.
- [22] Kawai, R. T., Friedman, D. M., and Serrano, L., “Blended Wing Body (BWB) Boundary Layer Ingestion (BLI) Inlet Configuration and System Studies,” NASA CR CR-2006-214534, National Aeronautics and Space Administration, 2006.
- [23] Greitzer, E., Bonnefoy, P., la Rosa Blanco, E. D., Dorbian, C., Drela, M., Hall, D., Hansman, R., Hileman, J., Liebeck, R., Lovegren, J., Mody, P., Pertuze, J., Sato, S., Spakovszky, Z., Tan, C., Hollman, J., Duda, J., Fitzgerald, N., Houghton, J., Kerrebrock, J., Kiwada, G., Kordonowy, D., Parrish, J., Tylko, J., Wen, E., and Lord, W., “N+3 Aircraft Concept Designs and Trade Studies, Final Report,” NASA CR 2010-216794, National Aeronautics and Space Administration, 2010.
- [24] Drela, M., “Simultaneous Optimization of the Airframe, Powerplant, and Operation of Transport Aircraft,” Tech. rep., MIT, 2010.

- [25] Drela, M., “Development of the D8 Transport Configuration,” *9th AIAA Applied Aerodynamics Conference*, 2011, AIAA 2011-3970.
- [26] Felder, J. L., Kim, H. D., and Brown, G. V., “Turboelectric Distributed Propulsion Engine Cycle Analysis for Hybrid-Wing-Body Aircraft,” *47th AIAA Aerospace Sciences Meeting including The New Horizons Forum and Aerospace Exposition*, 2009, AIAA 2009-1132.
- [27] Welstead, J. R. and Felder, J. L., “Conceptual Design of a Single-Aisle Turboelectric Commercial Transport with Fuselage Boundary Layer Ingestion,” *54th AIAA Aerospace Sciences Meeting*, 2016, AIAA 2016-1027.
- [28] Hall, D. K., Huang, A. C., Uranga, A., Greitzer, E. M., Drela, M., , and Sato, S., “Boundary Layer Ingestion Propulsion Benefit for Transport Aircraft,” *Journal of Propulsion and Power*, Vol. 33, No. 5, 2017, pp. 1118–1129.
- [29] Jones, S., “An Introduction to Thermodynamic Performance Analysis of Aircraft Gas Turbine Engine Cycles Using the Numerical Propulsion System Simulation Code,” Tech. rep., Glenn Research Center, 2007, NASA TM-2007-214690.
- [30] Jones, S. M., Haller, W. J., and Tong, M. T., “An N+3 Technology Level Reference Propulsion System,” 2017, NASA/TM2017-219501.
- [31] Uranga, A., Drela, M., Greitzer, E. T., Lieu, N. A., M. K., S., N. M., H., A. C., G., M., G., and Hannon, J. A.
- [32] Pandya, S. A., Uranga, A., Espitia, A., and Huang, A., “Computational Assessment of the Boundary Layer Ingesting Nacelle Design of the D8 Aircraft,” *52nd AIAA Aerospace Sciences Meeting*, 2014, AIAA-2014-0907.
- [33] Uranga, A., Drela, M., Greitzer, E. M., Hall, D. K., Titchener, N. A., Lieu, M. K., Siu, N. M., Casses, C., Huang, A. C., Gatlin, G. M., , and Hannon, J. A., “Boundary Layer Ingestion Benefit of the D8 Transport Aircraft,” *AIAA Journal*, Vol. 55, No. 11, 2017, pp. 3693–3708.
- [34] Turnbull, A., “Independent Assessment of the D8 Concept’s Risk,” Tech. rep., NASA, September 2014.
- [35] Marien, T., Welstead, J. R., and Jones, S. M., “Vehicle Level System Impact of Boundary Layer Ingestion for the NASA D8 Concept Aircraft,” *2018 AIAA Aerospace Sciences Meeting*, Kissimmee, FL, January 2018, AIAA-2018-0271.
- [36] Blumenthal, B., Elmiligui, A. A., Geiselhart, K., Campbell, R. L., Maughmer, M. D., and Schmitz, S., “Computational Investigation of a Boundary-Layer Ingestion Propulsion System for the Common Research Model,” *46th AIAA Fluid Dynamics Conference, Aviation Forum*, 2016, AIAA 2016-3812.

- [37] Vassberg, J. C., DeHaan, M. A., Rivers, S. M., and Wahls, R. A., “Development of a Common Research Model for Applied CFD Validation Studies,” 2008, AIAA 2008-6919.
- [38] Ordaz, I., Rallabhandi, S. K., Nielsen, E. J., and Diskin, B., “Mitigation of Engine Inlet Distortion through Adjoint-Based Design,” *35th AIAA Applied Aerodynamics Conference*, 2017, p. 3410, AIAA-2017-3410.
- [39] “Aerodynamic shape optimization of the STARC-ABL concept for minimal inlet distortion,” January 2018.
- [40] Florea, R. V., Matalanis, C., Hardin, L. W., Stucky, M., , and Shabbir, A., “Parametric Analysis and Design for Embedded Engine Inlets,” *Journal of Propulsion and Power*, Vol. 31, No. 5, 2015, pp. 843–850.
- [41] Ochs, S. S., Tillman, G., Joo, J., and Voytovych, D. M., “Computational Fluid Dynamics-Based Analysis of Boundary Layer Ingesting Propulsion,” *Journal of Propulsion and Power*, Vol. 33, No. 2, 2017, pp. 522–530.
- [42] Florea, R. V., Matalanis, C., Hardin, L. W., Stucky, M., , and Shabbir, A., “Computational analysis of the effects of a boundary layer ingesting propulsion system in transonic flow,” *Proceedings of the Institution of Mechanical Engineers, Part G: Journal of Aerospace Engineering*, Vol. 227, No. 8, 2013, pp. 1215–1232.
- [43] Arend, D. J., Wolter, J. D., Hirt, S. M., Provenza, A., Gazzaniga, J. A., Cousins, W. T., Hardin, L. W., , and Sharma, O., “Experimental Evaluation of an Embedded Boundary Layer Ingesting Propulsor for Highly Efficient Subsonic Cruise Aircraft,” *53rd AIAA/SAE/ASEE Joint Propulsion Conference*, 2017, AIAA-2017-5041.
- [44] Turnbull, A., Jouan, H., Giannakakis, P., and Isikveren, A. T., “Modeling Boundary Layer Ingestion at the Conceptual Level,” *Proceedings of the 23rd ISABE Conference*, Fort Worth, TX, 2017, ISABE-2017-22700.
- [45] Ordaz, I., “Aero-Propulsive Analysis and Design Framework,” Tech. rep., NASA, December 2017.
- [46] Bryson, A. E. and Ho, Y.-C., *Applied Optimal Control: Optimization, Estimation, and Control*, John Wiley & Sons, 1975.
- [47] Arora, J. and Haug, E. J., “Methods of Design Sensitivity Analysis in Structural Optimization,” *AIAA Journal*, Vol. 17, No. 9, 1979, pp. 970–974.
- [48] Sobieszczanski-Sobieski, J., “Sensitivity Analysis and Multidisciplinary Optimization for Aircraft Design: Recent Advances and Results,” *Journal of Aircraft*, Vol. 27, No. 12, Dec. 1990, pp. 993–1001.
- [49] Martins, J. R. R. A., Alonso, J. J., and Reuther, J. J., “High-Fidelity Aerostructural Design Optimization of a Supersonic Business Jet,” *Journal of Aircraft*, Vol. 41, No. 3, 2004, pp. 523–530.

- [50] Martins, J. R. R. A., Alonso, J. J., and Reuther, J. J., “A Coupled-Adjoint Sensitivity Analysis Method for High-Fidelity Aero-Structural Design,” *Optimization and Engineering*, Vol. 6, No. 1, March 2005, pp. 33–62.
- [51] Kenway, G. K., Kennedy, G. J., and Martins, J. R. R. A., “A CAD-Free Approach to High-Fidelity Aerostructural Optimization,” *Proceedings of the 13th AIAA/ISSMO Multidisciplinary Analysis Optimization Conference*, No. AIAA 2010-9231, Fort Worth, TX, Sept. 2010.
- [52] Kenway, G. K. W., Kennedy, G. J., and Martins, J. R. R. A., “Scalable parallel approach for high-fidelity steady-state aeroelastic analysis and adjoint derivative computations,” *AIAA Journal*, Vol. 52, 2014, pp. 935–951.
- [53] Kennedy, G. J., Martins, J. R. R. A., and Hansen, J. S., “Aerostructural optimization of aircraft structures using asymmetric subspace optimization,” *12th AIAA/ISSMO Multidisciplinary Analysis and Optimization Conference, Victoria, BC*, AIAA, 2008, AIAA-2008-5847.
- [54] Kennedy, G. J. and Martins, J. R. R. A., “Parallel solution methods for aerostructural analysis and design optimization,” *Proceedings of the 13th AIAA/ISSMO Multidisciplinary Analysis Optimization Conference*, Fort Worth, TX, 2010, AIAA 2010-9308.
- [55] Marta, A. C., Mader, C. A., Martins, J. R. R. A., van der Weide, E., and Alonso, J. J., “A methodology for the development of discrete adjoint solvers using automatic differentiation tools,” *International Journal of Computational Fluid Dynamics*, Vol. 21, No. 9, 2007, pp. 307–327.
- [56] Mader, C. A., Martins, J. R. R. A., Alonso, J. J., and van der Weide, E., “ADjoint: An Approach for the Rapid Development of Discrete Adjoint Solvers,” *AIAA Journal*, Vol. 46, No. 4, April 2008, pp. 863–873.
- [57] Martins, J. R. R. A. and Hwang, J. T., “Review and Unification of Methods for Computing Derivatives of Multidisciplinary Computational Models,” *AIAA Journal*, Vol. 51, No. 11, November 2013, pp. 2582–2599.
- [58] Hwang, J. T. and Martins, J. R. R. A., “A computational architecture for coupling heterogeneous numerical models and computing coupled derivatives,” *ACM TOMS*, Vol. 44, No. 37, 2018.
- [59] Osusky, L. and Zingg, D. W., “A Novel Aerodynamic Shape Optimization Approach for Three-Dimensional Turbulent Flows,” *Proceedings of the 50th AIAA Aerospace Sciences Meeting including the New Horizons Forum and Aerospace Exposition*, Nashville, TN, Feb 2012, AIAA 2012-0058.
- [60] “Automatic Differentiation Adjoint of the Reynolds-Averaged Navier-Stokes Equations with a Turbulence Model,” *43rd AIAA Fluid Dynamics Conference and Exhibit*, June 2013, AIAA 2013-2581.

- [61] Gray, J. S., Hearn, T. A., Moore, K. T., Hwang, J. T., Martins, J. R. R. A., and Ning, A., “Automatic Evaluation of Multidisciplinary Derivatives Using a Graph-Based Problem Formulation in OpenMDAO,” *15th AIAA/ISSMO Multidisciplinary Analysis and Optimization Conference*, American Institute of Aeronautics and Astronautics, August 2014.
- [62] Lyu, Z., Xu, Z., and Martins, J. R. R. A., “Benchmarking Optimization Algorithms for Wing Aerodynamic Design Optimization,” *8th International Conference on Computational Fluid Dynamics (ICCFD8)*, Chengdu, China, July 2014, ICCFD8 2014-0203.
- [63] Martins, J. R. R. A. and Lambe, A. B., “Multidisciplinary Design Optimization: A Survey of Architectures,” *AIAA Journal*, Vol. 51, 2013, pp. 2049–2075.
- [64] Tedford, N. P. and Martins, J. R. R. A., “Benchmarking Multidisciplinary Design Optimization Algorithms,” *Optimization and Engineering*, Vol. 11, No. 1, February 2010, pp. 159–183.
- [65] Gray, J. S., Moore, K. T., Hearn, T. A., and Naylor, B. A., “Standard Platform for Benchmarking Multidisciplinary Design Analysis and Optimization Architectures,” *AIAA Journal*, Vol. 51, No. 10, Oct 2013, pp. 2380–2394.
- [66] Kenway, G. K. W., *A Scalable, Parallel Approach for Multi-Point, High-Fidelity Aerostructural Optimization of Aircraft Configurations*, Ph.D. thesis, University of Toronto, 2013.
- [67] Kenway, G. K. W. and Martins, J. R. R. A., “Multipoint High-fidelity Aerostructural Optimization of a Transport Aircraft Configuration,” *Journal of Aircraft*, Vol. 51, 2014, pp. 144–160.
- [68] “Review and Unification of Methods for Computing Derivatives of Multidisciplinary Computational Models,” *AIAA Journal*, Vol. 51, 2013, pp. 2582–2599.
- [69] Hwang, J. T. and Martins, J. R. R. A., “A computational architecture for coupling heterogeneous numerical models and computing coupled derivatives,” *ACM Transactions on Mathematical Software*, Vol. 44, No. 4, 2018.
- [70] van der Weide, E., G. Kalitzin, J. S., , and Alonso, J. J., “Unsteady Turbomachinery Computations Using Massively Parallel Platforms,” *In Proceedings of the 44th AIAA Aerospace Sciences Meeting and Exhibit*, 2006, AIAA 2006-0421.
- [71] Kenway, G. K. W., Secco, N. R., Martins, J. R. R. A., Mishra, A., and Duraisamy, K., “An Efficient Parallel Overset Method for Aerodynamic Shape Optimization,” *Proceedings of the 58th AIAA/ASCE/AHS/ASC Structures, Structural Dynamics, and Materials Conference, AIAA SciTech Forum*, January 2017.

- [72] Mader, C. A., Kenway, G. K., Martins, J., and Uranga, A., “Aerostructural Optimization of the D8 Wing with Varying Cruise Mach Numbers,” *18th AIAA/ISSMO Multi-disciplinary Analysis and Optimization Conference*, American Institute of Aeronautics and Astronautics, June 2017.
- [73] Brooks, T. R., Kenway, G. K. W., and Martins, J. R. R. A., “Benchmark Aerostructural Models for the Study of Transonic Aircraft Wings,” *AIAA Journal*, 2018, (In press).
- [74] Burdette, D. A. and Martins, J. R. R. A., “Impact of Morphing Trailing Edge on Mission Performance for the Common Research Model,” *Journal of Aircraft*, 2018, (In press).
- [75] Hendricks, E. S., Jones, S. M., and Gray, J. S., “Design Optimization of a Variable-Speed Power-Turbine,” *50th AIAA/ASME/SAE/ASEE Joint Propulsion Conference*, Cleveland, Ohio, July 2014, AIAA-2014-3445.
- [76] Geiselhart, K., Ozoroski, L. P., Fenbert, J. W., Shields, E. W., and Li, W., “Integration of Multifidelity Multidisciplinary Computer Codes for Design and Analysis of Supersonic Aircraft,” *49th AIAA Aerospace Sciences Meeting*, 2011, AIAA 2011-465.
- [77] Allison, D., Morris, C., Schetz, J., Kapania, R., Sultan, C., Deaton, J., and Grandhi, R., “A Multidisciplinary Design Optimization Framework for Design Studies of an Efficient Supersonic Air Vehicle,” *12th AIAA Aviation Technology, Integration, and Operations (ATIO) Conference and 14th AIAA/ISSMO Multidisciplinary Analysis and Optimization Conference*, 2012, AIAA 2012-5492.
- [78] Allison, D. L., Alyanak, E., and Bhagat, N., “High Fidelity, Nonlinear, Integrated Nozzle Installation Effects for Numerical Propulsion System Simulation,” *56th AIAA/ASCE/AHS/ASC Structures, Structural Dynamics, and Materials Conference*, 2015, AIAA 2015-0649.
- [79] Allison, D. L., Alyanak, E. J., and Shimmin, K., “Aircraft System Affects Including Propulsion and Air Cycle Machine Coupled Interactions,” *57th AIAA/ASCE/AHS/ASC Structures, Structural Dynamics, and Materials Conference*, 2016, AIAA 2016-0671.
- [80] Tran, D. H. and Snyder, C. A., “Effects of Chemical Equilibrium on Turbine Engine Performance for Various Fuels and Combustor Temperatures,” Tech. Rep. NASA-TM-105399, Glenn Research Center, 1992.
- [81] Nuzum, S. R., Donovan, A., Roberts, R. A., and Wolff, M., “Dynamic Modeling at a Vehicle Level of a Cryogenic Based Thermal System for a High Powered System,” *57th AIAA/ASCE/AHS/ASC Structures, Structural Dynamics, and Materials Conference*, 2016, AIAA 2016-0673.

- [82] Walter, M. A. T. and Owen, P. R., “Element Potential-Based Procedure for Meta-modeling of Combustion Products,” *Journal of Propulsion and Power*, Vol. 30, No. 6, 2014, pp. 1711–1720.
- [83] Gordon, S. and McBride, B. J., “Computer Program for Calculation of Complex Chemical Equilibrium Compositions, Rocket Performance, Incident and Reflected Shocks, and Chapman-Jouguet Detonations,” 1994, NASA RP-1311.
- [84] Schechter, W. D. and McAvoy, D. C., “MINEQL+: A Software Environment for Chemical Equilibrium Modeling,” *Computers, Environment and Urban Systems*, Vol. 16, No. 1, 1992, pp. 65–76.
- [85] Konigsberger, E. and Eriksson, G., “A New Optimization Routine for Chemsage,” *Calphad*, Vol. 19, No. 2, 1995, pp. 207–214.
- [86] Smith, W. R. and Missen, R. W., *Chemical Reaction Equilibrium Analysis: Theory and Algorithms*, Wiley, 1st ed., 1982.
- [87] Goodwin, D. G., Moffat, H. K., and Speth, R. L., “Cantera: An Object-oriented Software Toolkit for Chemical Kinetics, Thermodynamics, and Transport Processes,” <http://www.cantera.org>, 2014, Version 2.1.2.
- [88] Chin, J., Gray, J., Jones, S., and Berton, J., “Open-Source Conceptual Sizing Models for the Hyperloop Passenger Pod,” *56th AIAA/ASCE/AHS/ASC Structures, Structural Dynamics, and Materials Conference*, 2015, AIAA 2015-1587.
- [89] Haglind, F. and Singh, R., “Design of Aero Gas Turbines Using Hydrogen,” *Journal of Engineering for Gas Turbines and Power*, Vol. 128, No. 4, 2006, pp. 754–764.
- [90] Fulton, K., “Cryogenic Fueled Turbofans: Kuznetsov Bureau’s Pioneer Work on LH₂ and LNG Dual-Fuel Engines,” *Aircraft Engineering and Aerospace Technology*, Vol. 65, No. 11, 1993, pp. 8–11.
- [91] Leal, A. M., Blunt, M. J., and LaForce, T. C., “A Robust and Efficient Numerical Method for Multiphase Equilibrium Calculations: Application to CO₂-Brine-Rock Systems at High Temperatures, Pressures and Salinities,” *Advances in Water Resources*, Vol. 62, Part C, 2013, pp. 409–430.
- [92] Jr., M. W. C., “NIST-JANAF Thermochemical Tables, Forth Edition, Monograph 9,” *Journal of Physical and Chemical Reference Data*, 1998.
- [93] Lefebvre, A. H., *Gas Turbine Combustion*, CRC Press, 3rd ed., 1998.
- [94] Bradley, M. K. and Droney, C. K., “Subsonic Ultra Green Aircraft Research: Phase I Final Report,” NASA CR 2011-216847, National Aeronautics and Space Administration, 2011.
- [95] Heath, C. M., Slater, J. W., and Rallabhandi, S. K., “Inlet Trade Study for a Low-Boom Aircraft Demonstrator,” *Journal of Aircraft*, 2016.

- [96] Joseph W. Connolly, Pawel Chwalowski, M. D. S. J.-r. C. W. A. S. J. J. M. and Kopasakis, G., “Towards an Aero-Propulso-Servo-Elasticity Analysis of a Commercial Supersonic Transport,” *15th Dynamics Specialists Conference, AIAA SciTech Forum*, 2016.
- [97] Liu, C., Doulgeris, G., Laskaridis, P., and Singh, R., “Thermal cycle analysis of turbinelectric distributed propulsion system with boundary layer ingestion,” *Aerospace Science and Technology*, Vol. 27, No. 1, 2013, pp. 163 – 170.
- [98] Laskaridis, P., Pachidis, V., and Pilidis, P., “Opportunities and challenges for distributed propulsion and boundary layer ingestion,” *Aircraft Engineering and Aerospace Technology*, Vol. 86, No. 6, 2014, pp. 451–458.
- [99] Luke, E., Collins, E., and Blades, E., “A fast mesh deformation method using explicit interpolation,” *Journal of Computational Physics*, Vol. 231, No. 2, 2012, pp. 586 – 601.
- [100] Gill, P. E., Murray, W., and Saunders, M. A., “SNOPT: An SQP Algorithm for Large-Scale Constrained Optimization,” *SIAM Rev.*, Vol. 47, No. 1, Jan. 2005, pp. 99–131.
- [101] Martins, J. R. R. A. and Lambe, A. B., “Multidisciplinary Design Optimization: A Survey of Architectures,” *AIAA Journal*, Vol. 51, 2013, pp. 2049–2075.
- [102] McCullers, L. A., “Aircraft configuration optimization including optimized flight profiles,” NASA CR CP-2327, National Aeronautics and Space Administration, 1984.
- [103] Hall, D. K., Greitzer, E. M., and Tan, C. S., “Analysis of Fan Stage Conceptual Design Attributes for Boundary Layer Ingestion,” *Journal of Turbomachinery*, Vol. 139, No. 7, 2017.
- [104] Hahn, A., “Vehicle Sketch Pad: a Parametric Geometry Modeler for Conceptual Aircraft Design,” *48th AIAA Aerospace Sciences Meeting Including the New Horizons Forum and Aerospace Exposition, Aerospace Sciences Meetings*, 2010, AIAA 2010-657.
- [105] Secco, N. R., Jasa, J. P., Kenway, G. K. W., and Martins, J. R. R. A., “Component-based Geometry Manipulation for Aerodynamic Shape Optimization with Overset Meshes,” *AIAA Journal*, 2018, (Accepted subject to revisions 2018-02-08).
- [106] Kenway, G. K. W. and Martins, J. R. R. A., “Multipoint Aerodynamic Shape Optimization Investigations of the Common Research Model Wing,” *AIAA Journal*, Vol. 54, No. 1, January 2016, pp. 113–128.
- [107] Liem, R. P., Kenway, G. K., and Martins, J. R. R. A., “Multi-point, multi-mission, high-fidelity aerostructural optimization of a long-range aircraft configuration,” *Proceedings of the 14th AIAA/ISSMO Multidisciplinary Analysis and Optimization Conference*, Indianapolis, IN, September 2012.

- [108] Liem, R. P., Kenway, G. K. W., and Martins, J. R. R. A., “Multimission Aircraft Fuel Burn Minimization via Multipoint Aerostructural Optimization,” *AIAA Journal*, Vol. 53, 2015, pp. 104–122.
- [109] Livesey, J. L. and Hugh, T., “Suitable Mean Values in One-Dimensional Gas Dynamics,” *Journal of Mechanical Engineering Science*, Vol. 8, No. 4, 1966, pp. 374–383.
- [110] Livesey, J. L., editor, *Flow property averaging methods for compressible internal flows*, January 1982.
- [111] International, S., *Gas turbine inlet flow distortion guidelines. Aerospace Recommended Practice ARP1420*, 2017.
- [112] Kreisselmeier, G. and Steinhauser, R., “Systematic Control Design by Optimizing a Vector Performance Index,” *International Federation of Active Controls Symposium on Computer-Aided Design of Control Systems, Zurich, Switzerland*, 1979.

APPENDIX A

Derivation of Power Balance Method

This derivation is a more detailed version of the one provided by Drela's 2009 paper on the power balance method [2], with intermediate steps explicitly included. The derivation begins with the definition of a non-traditional control volume, illustrated shown in Figure A.1. The control volume is defined as a cylinder (or a rectangle in 2-D) taken at mid-field distance from the aircraft, with an infinitely thin section where the control volume folds in on itself to wrap around the body surface. This is shown as the diagonal slash in the left side of the control volume. An integral over the entire control volume can be converted to a

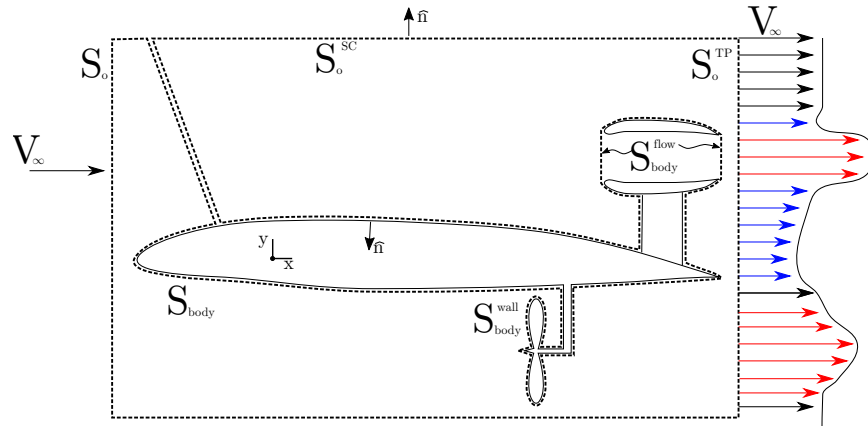


Figure A.1: Control volume definition for the derivation of the power balance equations. Modified from the original figure from Drela's power balance paper [2].

surface integral with Gauss's theorem:

$$\begin{aligned} \iiint \nabla \cdot (\phi) dV &= \iint (\phi) \cdot \hat{n} dS \\ &= \iint (\phi) \cdot \hat{n} dS_{body} + \iint (\phi) \cdot \hat{n} dS_o, \end{aligned} \quad (A.1)$$

where S_{body} is the surface fitted to the body and S_o is the outer surface.

A.1 Conservation of Mass

The conservation of mass for steady flow in divergence form is defined as

$$\nabla \cdot (\rho \vec{V}) = 0. \quad (\text{A.2})$$

Combining the conservation of mass with Equation (A.1) to form a surface integral gives

$$\iiint \nabla \cdot (\rho \vec{V}) dV = \iint (\rho \vec{V}) \cdot \hat{n} dS_{body} + \iint (\rho \vec{V}) \cdot \hat{n} dS_o = 0 \quad (\text{A.3})$$

The net mass flux across any given surface is given as

$$\iint (\rho \vec{V}) \cdot \hat{n} dS = \dot{m}. \quad (\text{A.4})$$

Combining Equations (A.3) and (A.4) gives

$$\dot{m}_{body} + \dot{m}_o = 0, \quad (\text{A.5})$$

which holds as long as the addition of any mass from fuel flow of the jet engine is neglected.

A.2 Conservation of Momentum

The conservation of momentum for steady flow, in divergence form is given as

$$\nabla \left(\rho \vec{V} \cdot \vec{V} \right) = -\nabla p + \nabla \cdot \bar{\tau}. \quad (\text{A.6})$$

Applying Equation (A.1) gives

$$\underbrace{\iint [(p\hat{n} - \bar{\tau} \cdot \hat{n}) + \vec{V} \cdot \rho \vec{V} \cdot \hat{n}] dS_{body}}_{F_{body}} + \underbrace{\iint [(p\hat{n} - \bar{\tau} \cdot \hat{n}) + \vec{V} \cdot \rho \vec{V} \cdot \hat{n}] dS_o}_{F_o} = 0, \quad (\text{A.7})$$

$$F_{body} + F_o = 0. \quad (\text{A.8})$$

Thus conservation of momentum simply says that the force on the body and the force on the outer boundary must perfectly cancel each other out. The force on the body surface (\vec{F}_{body}) can slightly simplified by substituting $\vec{\tau} = \bar{\tau} \cdot \hat{n}$:

$$\vec{F}_{body} = \iint [(p\hat{n} - \vec{\tau}) + \vec{V} \cdot \rho \vec{V} \cdot \hat{n}] dS_{body} \quad (\text{A.9})$$

On the outer surface of the control volume there is no wall to sustain any viscous forces, so

$$\iint \bar{\tau} \cdot \hat{n} dS_o = 0. \quad (\text{A.10})$$

This allows the equation for the force on the outer surface (\vec{F}_o) to be simplified to

$$\vec{F}_o = \iint [p\hat{n} + \vec{V}\rho\vec{V} \cdot \hat{n}] d\mathcal{S}_o \quad (\text{A.11})$$

A.2.1 Conversion to Reference Quantities

The force integrals can be further modified to use a reference pressure ($p - p_\infty$) by noting that the integral of a normal vector along any closed boundary is 0:

$$p_\infty \iint \hat{n} d\mathcal{S} = p_\infty \iint \hat{n} d\mathcal{S}_{body} + p_\infty \iint \hat{n} d\mathcal{S}_o = 0. \quad (\text{A.12})$$

Similarly a reference velocity ($\vec{V} - \vec{V}_\infty$) can be used by leveraging Equation (A.4) as follows:

$$\vec{V}_\infty \iint \rho\vec{V} \cdot \hat{n} d\mathcal{S} = \vec{V}_\infty \iint \rho\vec{V} \cdot \hat{n} d\mathcal{S}_{body} + \vec{V}_\infty \iint \rho\vec{V} \cdot \hat{n} d\mathcal{S}_o = 0. \quad (\text{A.13})$$

Subtracting Equations (A.12) and (A.13) from Equation (A.7) gives:

$$\vec{F}_{body} = \iint [(p - p_\infty)\hat{n} - \vec{\tau} + (\vec{V} - \vec{V}_\infty)\rho\vec{V} \cdot \hat{n}] d\mathcal{S}_{body} \quad (\text{A.14})$$

$$\vec{F}_o = \iint [(p - p_\infty)\hat{n} + (\vec{V} - \vec{V}_\infty)\rho\vec{V} \cdot \hat{n}] d\mathcal{S}_o \quad (\text{A.15})$$

Note that the subtraction of the zero terms can only be done, if the new terms include integrals over both \mathcal{S}_{body} and \mathcal{S}_o , because Equation (A.12) and (A.4) require integrals over a closed surface, which is only true if both the body and outer surfaces are included. In other words, if you want to use reference values you must use them for both F_{body} and F_o .

A.3 Mechanical Power Analysis

The mechanical energy flux across the control volume can be computed as the dot product of Equation (A.6) with \vec{V} as follows:

$$\nabla \cdot (\rho\vec{V}\vec{V}) \cdot \vec{V} = -\nabla p \cdot \vec{V} + (\nabla \cdot \bar{\tau}) \cdot \vec{V} \quad (\text{A.16})$$

$$\left(\vec{V} \underbrace{(\nabla \cdot \rho\vec{V})}_{\text{Eq. (A.2)} \equiv 0} + \rho\vec{V} \cdot \nabla \vec{V} \right) \cdot \vec{V} = -\nabla p \cdot \vec{V} + (\nabla \cdot \bar{\tau}) \cdot \vec{V} \quad (\text{A.17})$$

$$(\rho\vec{V} \cdot \nabla \vec{V}) \cdot \vec{V} = -\nabla p \cdot \vec{V} + (\nabla \cdot \bar{\tau}) \cdot \vec{V} \quad (\text{A.18})$$

$$\rho\vec{V} \cdot \vec{V} \cdot \nabla \vec{V} = -\nabla p \cdot \vec{V} + (\nabla \cdot \bar{\tau}) \cdot \vec{V} \quad (\text{A.19})$$

We now use the following identity related to the ∇ operator:

$$\nabla(\vec{a} \cdot \vec{b}) = \vec{b} \cdot \nabla \vec{a} + \vec{a} \cdot \nabla \vec{b} \quad (\text{A.20})$$

If we take $\vec{a} = \vec{b}$ then the identity reduces to

$$\begin{aligned} \nabla(\vec{a} \cdot \vec{a}) &= 2\vec{a} \cdot \nabla \vec{a} \\ \frac{1}{2}\nabla(\vec{a} \cdot \vec{a}) &= \vec{a} \cdot \nabla \vec{a} \\ \frac{1}{2}\nabla(a^2) &= \vec{a} \cdot \nabla \vec{a} \end{aligned} \quad (\text{A.21})$$

Applying Equation (A.21) to Equation (A.19) gives

$$\rho \vec{V} \cdot \frac{1}{2} \nabla V^2 = -\nabla p \cdot \vec{V} + (\nabla \cdot \bar{\tau}) \cdot \vec{V} \quad (\text{A.22})$$

$$\nabla \cdot \left(\rho \vec{V} \frac{1}{2} V^2 \right) = -\nabla p \cdot \vec{V} + (\nabla \cdot \bar{\tau}) \cdot \vec{V} \quad (\text{A.23})$$

Noting that

$$\nabla \cdot (p \vec{V}) = \nabla p \cdot \vec{V} + p \nabla \cdot \vec{V} \quad (\text{A.24})$$

$$\nabla(\bar{\tau} \cdot \vec{V}) = (\nabla \cdot \bar{\tau}) \cdot \vec{V} + (\bar{\tau} \cdot \nabla) \cdot \vec{V}, \quad (\text{A.25})$$

We can further manipulate Equation (A.23) into the following form:

$$\nabla \cdot \left(\rho \vec{V} \frac{1}{2} V^2 \right) = -\nabla \cdot (p \vec{V}) + p \nabla \cdot \vec{V} + \nabla \cdot (\bar{\tau} \cdot \vec{V}) - (\bar{\tau} \cdot \nabla) \cdot \vec{V} \quad (\text{A.26})$$

Integrating over the control volume and applying Gauss's theorem to the terms where it is applicable gives

$$\begin{aligned} \iint \left(\rho \vec{V} \frac{1}{2} V^2 \right) \cdot \hat{n} d\mathcal{S} &= \iint -(p \vec{V}) \cdot \hat{n} d\mathcal{S} + \iiint p \nabla \cdot \vec{V} d\mathcal{V} + \\ &\quad \iint (\bar{\tau} \cdot \vec{V}) \cdot \hat{n} d\mathcal{S} + \iiint -(\bar{\tau} \cdot \nabla) \cdot \vec{V} d\mathcal{V}. \end{aligned} \quad (\text{A.27})$$

A.3.1 Can Not Convert to Reference Quantities

As an aside, note that you can not convert the mechanical shaft power equation to reference quantities ($p - p_\infty$ and $\vec{V} - \vec{V}_\infty$) in a similar fashion to what was done for the force equation. In the prior case, we subtracted two quantities which both equaled zero — Equations (A.12) and (A.13)— in order to convert over to reference quantities.

This same approach will not work here, because of the dot product with \vec{V} used to form

the power equation. Consider one of the volume integral terms from Equation A.27:

$$\iiint p \nabla \cdot \vec{V} dV. \quad (\text{A.28})$$

In order to convert this term to reference pressure we need to subtract a non-zero quantity:

$$\iiint p \nabla \cdot \vec{V} dV - \underbrace{\iiint p_\infty \nabla \cdot \vec{V} dV}_{!=0} = \iiint (p - p_\infty) \nabla \cdot \vec{V} dV. \quad (\text{A.29})$$

Of course, subtracting a non-zero quantity is not allowed, so this term can not be converted to reference pressure. Similarly consider another term:

$$\iint -(p \vec{V}) \cdot \hat{n} dS. \quad (\text{A.30})$$

Again, we need to subtract a non-zero term to convert to reference pressure:

$$\iint -(p \vec{V}) \cdot \hat{n} dS - \underbrace{\iint -(p_\infty \vec{V}) \cdot \hat{n} dS}_{!=0} = \iint -(p - p_\infty) \vec{V} \cdot \hat{n} dS. \quad (\text{A.31})$$

Here the added quantity is non-zero because, although the integral of a normal vector along a closed surface is 0, the integral of the dot product of the velocity and normal vectors over a closed surface is non-zero unless that velocity is constant.

The same logic holds true for the usage of the conservation of mass to add a zero quantity with V_∞ involved. The presence of the original dot product with \vec{V} changes the terms, so the ability to add zero quantities is removed.

A.3.2 The Power Balance Equation

Drela's power balance equation is given as

$$P_k + P_s + P_v = \dot{\mathcal{E}} + \Phi. \quad (\text{A.32})$$

In order to derive that equation, starting from Equation (A.27), we now apply Equation (A.1) to break the terms up into the portions related to S_{body} and S_o as follows:

$$\begin{aligned} & \iint \left(\rho \vec{V} \frac{1}{2} V^2 \right) \cdot \hat{n} dS_{\text{body}} + \iint \left(\rho \vec{V} \frac{1}{2} V^2 \right) \cdot \hat{n} dS_o = \\ & \iint -(\rho \vec{V}) \cdot \hat{n} dS_{\text{body}} + \iint -(\rho \vec{V}) \cdot \hat{n} dS_o + \\ & \iint \iint p \nabla \cdot \vec{V} dV + \\ & \iint (\bar{\tau} \cdot \vec{V}) \cdot \hat{n} dS_{\text{body}} + \iint (\bar{\tau} \cdot \vec{V}) \cdot \hat{n} dS_o + \\ & \iint \iint -(\bar{\tau} \cdot \nabla) \cdot \vec{V} dV. \end{aligned} \quad (\text{A.33})$$

Note that $\iint (\bar{\tau} \cdot \vec{V}) \cdot \hat{n} dS_o = 0$ because there are no solid walls on the outer boundary. Next we re-arrange terms to group the body surface and outer surface related terms, remove the viscous term that is zero on the outer boundary, and apply the substitution $\vec{\tau} = \bar{\tau} \cdot \hat{n}$:

$$\begin{aligned} & \iint -\left(\rho \vec{V} \frac{1}{2} V^2 \right) \cdot \hat{n} dS_{\text{body}} + \iint -(\rho \vec{V}) \cdot \hat{n} dS_{\text{body}} + \\ & \iint (\vec{\tau} \cdot \vec{V}) dS_{\text{body}} + \underbrace{\iint \iint p \nabla \cdot \vec{V} dV}_{P_v} = \\ & \underbrace{\iint \left(\rho \vec{V} \frac{1}{2} V^2 \right) \cdot \hat{n} dS_o}_{\dot{\mathcal{E}}} + \iint (p \vec{V}) \cdot \hat{n} dS_o + \underbrace{\iint \iint -(\bar{\tau} \cdot \nabla) \cdot \vec{V} dV}_{\Phi}. \end{aligned} \quad (\text{A.34})$$

A.3.2.1 Aerodynamic Losses

The two terms on the right side of the equals sign in Equation (A.32) are both aerodynamic losses, and hence the lower they can be made the better. Φ , defined as

$$\Phi = \iint \iint -(\bar{\tau} \cdot \nabla) \cdot \vec{V} dV, \quad (\text{A.35})$$

Is a term related to the dissipation of energy within the control volume through fluid shearing against itself, creating heat. It represents a source of power loss through viscous effects.

Drela refers to the $\dot{\mathcal{E}}$ term as the mechanical energy flow rate out of the control volume. This is essentially wasted power that was added to the flow, but which did not produce useful work before leaving the control volume. $\dot{\mathcal{E}}$ is defined as

$$\dot{\mathcal{E}} = \iint \left[p + \frac{1}{2} (\rho V^2) \right] \vec{V} \cdot \hat{n} dS_o. \quad (\text{A.36})$$

This equation can be further refined by splitting the surface integral over \mathcal{S}_o into two parts: the left/right and the top/bottom surfaces. Drela refers to the top/bottom as the “side-cylinder” surfaces, which implies the assumption of a cylindrical 3-D control volume. He refers to the right side of the control volume as the “Treffz plane”. If you assume that V is always perpendicular to the left and right sides of the control volume, and noting the the left side of the control volume has a uniform velocity and pressure of $V = V_\infty$ and $p = p_\infty$, then you can represent $\dot{\mathcal{E}}$ via the scalar equation:

$$\dot{\mathcal{E}} = \iint \left[(p - p_\infty) + \frac{1}{2} \rho (V^2 - V_\infty^2) \right] V d\mathcal{S}_o^{TP} + \iint \left[(p) + \frac{1}{2} \rho V^2 \right] \vec{V} \cdot \hat{n} d\mathcal{S}_o^{SC}. \quad (\text{A.37})$$

Lastly, if you assume that the velocity on \mathcal{S}_o^{SC} is always perfectly parallel to the control volume boundary (a reasonable assumption as long as no large oblique shock waves are present), then you get simplified version of $\dot{\mathcal{E}}$ which I used in Chapter 1.2.1:

$$\dot{\mathcal{E}} = \iint \left[(p - p_\infty) + \frac{1}{2} \rho (V^2 - V_\infty^2) \right] V d\mathcal{S}_o^{TP}. \quad (\text{A.38})$$

It is important to note that the apparent reference values in the above equation — $p - p_\infty$ and $V^2 - V_\infty^2$ — are not in fact reference values at all. These terms arise from the integral over the left and right sides of the control volume, and the fact that the velocity and pressure forces are parallel on the Treffz plane and anti-parallel on the left side inflow plane.

A.3.2.2 Power addition

The three terms on the left side of the equals sign in Equation (A.32) are all related to net power addition to the flow.

We further separate the body surface, S_{body} into two additional sub-surfaces: S_{body}^{wall} , S_{body}^{flow} . S_{body}^{wall} includes all portions of the control volume that are adjacent to solid walls, including any moving surfaces such as spinning propeller blades. S_{body}^{flow} includes all portions of the control volume near the body where flow is entering or exiting (i.e. inlet and nozzle planes from the jet engine). Starting with Equation (A.32), but substituting in for terms we

have already defined we have:

$$\begin{aligned}
& \iint - \left(\rho \vec{V} \frac{1}{2} V^2 \right) \cdot \hat{n} d\mathcal{S}_{body} + \iint -(p \vec{V}) \cdot \hat{n} d\mathcal{S}_{body} + \iint (\vec{\tau} \cdot \vec{V}) d\mathcal{S}_{body} + P_s = \dot{\mathcal{E}} + \Phi \\
& \cancel{\iint - \left(\rho \vec{V} \frac{1}{2} V^2 \right) \cdot \hat{n} d\mathcal{S}_{body}^{\text{wall}}}^0 + \iint - \left(\rho \vec{V} \frac{1}{2} V^2 \right) \cdot \hat{n} d\mathcal{S}_{body}^{\text{flow}} + \\
& \iint -(p \vec{V}) \cdot \hat{n} d\mathcal{S}_{body}^{\text{wall}} + \iint -(p \vec{V}) \cdot \hat{n} d\mathcal{S}_{body}^{\text{flow}} + \\
& \iint (\vec{\tau} \cdot \vec{V}) d\mathcal{S}_{body}^{\text{wall}} + \cancel{\iint (\vec{\tau} \cdot \vec{V}) d\mathcal{S}_{body}^{\text{flow}}}^0 + \\
P_v &= \dot{\mathcal{E}} + \Phi
\end{aligned} \tag{A.39}$$

Now, grouping terms by $\mathcal{S}_{body}^{\text{flow}}$ and $\mathcal{S}_{body}^{\text{wall}}$ gives

$$\underbrace{\iint - \left[p + \rho \frac{1}{2} V^2 \right] \vec{V} \cdot \hat{n} d\mathcal{S}_{body}^{\text{flow}}}_{P_k} + \underbrace{\iint - [p \hat{n} + \vec{\tau}] \vec{V} d\mathcal{S}_{body}^{\text{wall}}}_{P_s} + P_v = \dot{\mathcal{E}} + \Phi \tag{A.40}$$

So P_k is defined as

$$P_k = \iint - \left[p + \rho \frac{1}{2} V^2 \right] \vec{V} \cdot \hat{n} d\mathcal{S}_{body}^{\text{flow}}, \tag{A.41}$$

and P_s is defined as

$$P_s = \iint - [p \hat{n} + \vec{\tau}] \vec{V} d\mathcal{S}_{body}^{\text{wall}} \tag{A.42}$$

Finally we arrive at Drela's power balance equation

$$P_k + P_s + P_v = \dot{\mathcal{E}} + \Phi. \tag{A.43}$$

Drela asserts that the P_v term is negligible except in certain corner cases and the power balance equation reduces to just

$$P_k + P_s = \dot{\mathcal{E}} + \Phi. \tag{A.44}$$

This is the form of the equation shown at the opening of Chapter 1.2.1